



Max-Planck-Institut für Metallforschung
Stuttgart

Stress and Microstructure of Sputter Deposited Thin Copper and Niobium Films

Brando Chidi Okolo

Dissertation
an der
Universität Stuttgart

Bericht Nr. 132
April 2003

Stress and Microstructure of Sputter Deposited Thin Copper and Niobium Films

Von der Fakultät für Chemie der Universität Stuttgart
zur Erlangung der Würde eines Doktors der Naturwissenschaften (Dr. rer. nat.)
genehmigte Abhandlung

Vorgelegt von

Brando Chidi Okolo

aus Enugu in Nigeria

Hauptberichter: Prof. Dr. Ir. E. J. Mittemeijer

Mitberichter: Prof. Dr. F. Aldinger

Tag der mündlichen Prüfung: 04 – 04 – 2003

MAX-PLANCK-INSTITUT FÜR METALLFORSCHUNG STUTTGART
INSTITUT FÜR METALLKUNDE DER UNIVERSITÄT STUTTGART
2003

Table of Contents

Summary	VII
1 The Effect of Deposition Parameters and Substrate Surface Condition on Texture, Morphology and Stress in Magnetron Sputter Deposited Cu Thin Films	1
Abstract	1
1. Introduction	1
2. Experimental	2
2.1 Film production	2
2.2 X-ray diffraction	4
<i>$\theta/2\theta$ scans</i>	4
<i>Pole figures and stress measurements</i>	4
2.3 Morphology	5
<i>Transmission Electron Microscopy (TEM)</i>	5
<i>Focussed Ion Beam (FIB) imaging</i>	5
<i>Atomic Force Microscopy (AFM)</i>	5
3. Results and Discussion	5
3.1 Substrate cleaning	5
3.1.1 Substrate roughness	5
3.1.2 Substrate surface composition	6
3.2 Texture	7
3.2.1 $\theta/2\theta$ scans	7
3.2.2 Pole-figure scans	12
<i>Random fraction</i>	14
<i>Texture strength and sharpness from fit</i>	15
3.2.2.1 Annealing effect	16

3.2.2.2 Thickness effect	17
3.2.2.3 Substrate cleaning effect	18
<i>500 nm films</i>	18
<i>Ultrathin films</i>	19
<i>Texture of film versus substrate surface roughness and impurities</i>	20
3.3 Morphology	21
3.3.1 Deposition gas pressure effect, 500 nm films	21
3.3.2 Annealing effect	23
3.3.3 Substrate cleaning effect, 500 nm films	24
3.3.4 Substrate cleaning effect, ultra thin films	26
3.4 Residual stress	27
3.4.1 Deposition gas pressure effect, 500 nm films	29
3.4.2 Substrate cleaning effect, ultra thin films	31
3.4.3 Substrate cleaning effect, 500 nm films	32
3.5 Microstrain	34
4. Conclusions	36
4.1 Texture	36
4.2 Morphology	37
4.3 Growth stress and microstrain	37
2 Stress, Texture and Microstructure in Nb Thin Films Sputter Deposited on Amorphous Substrates	39
Abstract	39
1. Introduction	39
2. Experimental	41
2.1 Substrate preparation and film deposition	41
2.2 X-ray Photoelectron Spectroscopy (XPS)	41
2.3 Atomic force microscopy (AFM)	42
2.4 Focussed ion beam (FIB) imaging	42
2.5 X-ray diffraction (XRD)	42

2.6 X-ray reflectometry	44
3. Results and Discussion	44
3.1 Chemical composition as a function of depth.....	44
3.2 Morphology	50
3.2.1 Surface topography	50
3.2.2 Grain size	53
3.3 Texture	57
3.3.1 $\theta/2\theta$ scans	57
3.3.2 Pole-figure scans	58
3.4 Residual stress	62
3.4.1 Conventional $\sin^2\psi$ method	62
3.4.2 Grazing incidence X-ray diffraction (GIXRD)	68
3.4.3 Aging effect	71
3.5 Microstrain	73
3.6 X-ray reflectometry	75
4. Conclusions	77
4.1 Chemical composition	77
4.2 Morphology	77
4.3 Texture	77
4.4 Stress and microstrain	78
3 Kurzfassung der Dissertation in deutscher Sprache	79
References	89
Curriculum Vitae	93

Summary

Thin film technology has wide applications in science and engineering industry. Cu and Nb have active relevance in micro-electromechanical systems (MEMS). For Cu thin films, as a possible replacement of Al in the metallisation of substrates while in the case of Nb thin films, its relevance comes to bear in corrosion resistance engineering needs and its superconductivity. The optimal use of these thin film materials lies in tailoring their properties to meet demands for their usage. Grain morphology, texture and stress constitute significant aspects of thin film properties. In the present work priority is to investigate the impact of thin film sputter deposition conditions, the nature of substrate and aging on these properties.

Cu and Nb films of various thickness ranges (5 – 1000 nm) were produced by magnetron sputter deposition on two commercially available Si based amorphous substrates, SiO₂ and Si₃N₄, under ultra high vacuum conditions. The as-deposited thin films were investigated by X-ray diffraction (XRD), X-ray reflectometry, auger electron spectroscopy (AES), X-ray photoelectron spectroscopy (XPS), transmission electron microscopy (TEM), atomic force microscopy (AFM) and focussed ion beam (FIB) imaging.

Sputter cleaning of the substrates at various ion acceleration voltages prior to film deposition was observed to markedly impact on microstructure, texture and stress states owing to the physical (surface roughness) and chemical changes (reduction in contaminant content) on the cleaned substrates.

With increase of the ion acceleration voltage the morphology of the ultrathin (5 nm thick) Cu films, which at this thickness were still at the coalescence stage of film growth, changed from larger sized islands to smaller sized islands. For the thicker films a grain morphology change from irregular geometries to columnar structures occurred with the application of substrate sputter cleaning prior to film deposition. This change was accompanied by a reduction in the average grain size from about 1000 nm (for the films deposited on uncleaned substrates) to 300 nm (for the films deposited on sputter cleaned substrates). No significant influence was observed based on the type of substrate i.e. SiO₂ or Si₃N₄. Of novel significance though is that microstructural changes in thin films are achievable at a constant deposition temperature and pressure. A structure zone model developed by J. A. Thornton in 1975 (see Chapter 1, section 3.3.3) which describes the physical manifestations of thin film microstructure during sputter deposition ascribes morphology changes to temperature and pressure factors. Clearly this is not the case for the present Cu films where the substrate has also been found to significantly influence the film morphology, though it is noted that

the model was developed using film thicknesses that ranged between 20 to 250 μm . Furthermore, in both Cu films and Nb films, a thickness dependency exists whereby the lateral dimensions of grains increases with the thickening of thin films during the growth process. However substrate sputter cleaning prior to film deposition was not found to alter the morphology of Nb films.

Texture characterisation involved the combinational use of $\theta/2\theta$ scans and pole figure measurements with the powder diffraction ($\theta/2\theta$) scans more accurately accounting for the presence of a random component while the pole figure measurements fully account for the sharpness of a particular texture component. For the Cu films the $\{111\}$ fibre texture was the primary component while for the Nb films the $\{110\}$ fibre was dominant. The films deposited on Si_3N_4 substrates showed sharper (i.e. a decrease in the value of the HWHM) textures than those deposited on SiO_2 substrates. Sputter cleaning of the substrates prior to film deposition markedly sharpened the texture of the films except for the Cu films deposited on SiO_2 substrates where no effect of significance was observed.

The effect of deposition pressure on the texture of the Cu films was not obvious within the pressure range (5×10^{-2} Pa to 69×10^{-2} Pa) covered whereas annealing of the films after deposition increased the texture strength. Texture develops with an increase in sharpness for the Cu and Nb films deposited on both SiO_2 and Si_3N_4 substrates as a function of increasing film thickness. This effect is more pronounced for the films on the Si_3N_4 substrate.

A mechanism is proposed that accounts for the glaring difference in the texture of films deposited on amorphous SiO_2 and amorphous Si_3N_4 substrates. This hypothesis is based on the premise that the atomic interaction between Cu or Nb and O (of the SiO_2 substrate) is stronger than that between Cu or Nb and N (of the Si_3N_4 substrate). Therefore in the case of the metallic films deposited on SiO_2 substrates or uncleaned Si_3N_4 substrates (containing O contaminants at the surface, this interaction locally obstructs the formation of perfect crystalline order, i.e. fluctuations of the orientation of the nucleating crystals occur. The hindering effect against a perfect texture formation is suppressed by the removal of adsorbed impurities on the substrate surface during sputter cleaning. With increase in film thickness the texture in both film systems (metal - SiO_2 and metal - Si_3N_4) sharpens. This is attributed to the notion that continual material deposition during film growth occurs now on a highly ordered crystalline (i.e. no longer amorphous) material and/or the preferred growth of more ideally oriented crystals.

From the residual stress values $\sigma_{//,r}$ determined by the XRD $\sin^2\psi$ method, the intrinsic stresses $\sigma_{//,i}$ in Cu and Nb films were calculated by subtracting the thermal stress and found to be of compressive nature, though for the ultrathin Cu films a tensile stress regime originating from the

coalescence processes during film growth prevailed. A key-driving factor in the development of stress in the Cu films deposited is the evolution of film morphology. Cu films deposited on uncleaned substrates had irregular morphologies. However with substrates sputter cleaned at various ion acceleration voltages prior to the layer deposition a microstructure transition from irregular morphologies to columnar structures is accompanied by the emergence of tensile stress components due to intracolumnar voids in the films.

In the Nb films, oxide formation at the grain boundaries close to the surface causes a high compressive stress parallel to the film. Adopting a strain model originally meant for the explanation of stress generation in non-metallic films, it was possible to empirically account for stress generation in highly oxidation prone Nb films. Through the combined agencies of XPS and X-ray reflectometry it was observed that a 2 - 3 nm thick stable oxide layer of Nb₂O₅ forms on Nb film surfaces after deposition and from the oxide enriched top layer, oxygen is admitted into the metal matrix through grain boundary pathways. Oxides formed at the grain boundaries exert lateral forces on the neighboring grains as the grain boundaries expand to accommodate the additional matter. By this, for ultrathin Nb films a highly compressive stress is generated (in the order of a few GPa). As the film thickness is increased, at a constant penetration depth of oxygen to form oxides at the film grain boundaries, the measured stress, representing an average over the volume, is less in magnitude. The intrinsic stress - film thickness relationship was of the form: thickness change from 5 to 20 nm is accompanied by a drastic decrease in $\sigma_{//,i}$, further increase in film thickness from 20 to 100 nm led to a marked decrease in $\sigma_{//,i}$ and at film thickness of 100 and 500 nm $\sigma_{//,i}$ seems to saturate. The proof for the presence of a stress gradient in the thicker films was done by applying a grazing incidence diffraction geometry and it was shown that for a given film thickness, oxide enriched and perturbed regions close to the film surface are at higher stress states than oxide free regions deeper in the film. Four months after the films had been analyzed for stress state, XRD $\sin^2\psi$ stress analysis was repeated on the films and it was found that the stress causing mechanism (i.e. progressive oxidation of the film grain boundaries) in the Nb films was still active after 4 months of production. Further stress measurements on the films after 6 months of film production revealed that the state of stress had not changed significantly hence hinting an end of the oxide forming process at the film grain boundaries.

By the aid of a line profile analysis of the first and second order of the 111 reflection for the Cu films and 110 reflection for the Nb films using the Williamson-Hall method, the microstrain in a convenient set of these films was determined. The results revealed that microstrain in thin films has an underlying association with texture formation and crystal structure. Where for Cu films a

striking trend is for microstrain to increase with increase in texture sharpness in Nb films the trend is for microstrain to decrease with increase in texture sharpness.

One of the prime novelties of this work is the provision of experimental data on microstructure, texture and stress in ultrathin and thin films grown by magnetron sputter deposition. The data offers an opportunity for further success in the predictive aspect of materials sciences. Of equal significance is the quantitative description of differences between ultrathin films and thin films with respect to microstructure, texture and stress states.

Chapter 1. The Effect of Deposition Parameters and Substrate Surface Condition on Texture, Morphology and Stress in Magnetron Sputter Deposited Cu Thin Films

Abstract. Thin (500 nm and 1000 nm thick) and ultrathin (5 nm thick) Cu films were sputter deposited on as-received and sputter cleaned amorphous SiO₂ and Si₃N₄ wafer substrates. Two methods for the characterisation of the crystallographic texture by X-ray diffraction techniques ($\theta/2\theta$ scan and pole figure measurements) and their merits and limitations were illustrated. The microstructure of the films was investigated by Transmission Electron Microscopy, Focussed Ion Beam imaging and Atomic Force Microscopy. The X-ray diffraction $\sin^2\psi$ method was used for the determination of the residual stresses in the films. Due to the strong {111} texture, stress measurements were possible also for the ultrathin films. The dependence of the properties of the thin Cu films on the deposition gas pressure, film thickness, substrate type and cleaning conditions, and on annealing after deposition was investigated. The type and condition of the substrate was found to have a great impact on the microstructure of the Cu films. Sputter cleaning of the substrate prior to film deposition leads to a sharpening of the {111} fibre texture in films on Si₃N₄ substrate, whereas for films on SiO₂ substrate no influence was observed. The influence of cleaning the substrate on the morphology of the films is revealed in the smaller island size in the ultrathin films and for the 500 nm thick films, in the development of columnar microstructure. The growth stress of the ultrathin films at the coalescence stage of film growth was tensile. During film thickening the growth stress reversed to compressive owing to the relief of the coalescence stress and atomic peening. Microstrain in the films was found to correlate with the strength of the {111} texture. Annealing resulted in the sharpening of the {111} texture, grain growth and the relaxation of the compressive growth stress.

1. Introduction

A substantial number of investigations has been focussed in recent times on Cu films due to their potential as a viable replacement of Al in the metallisation of substrates [1-5]. Film production methods and procedures significantly affect the character of the end product. In sputter deposition, the nature of the substrate, deposition temperature, deposition pressure and the vacuum quality are some of the parameters that influence the film properties. Thin film properties such as stress, texture and morphology are of key importance for predicting the reliability of thin film systems. Stresses in

thin films are production process sensitive. These stresses can originate from thermal mismatch, working gas entrapment, atomic peening effect and interatomic attractive forces acting across island boundaries [6-9]. Texture occurs very frequently in thin films. The driving forces for texture formation are surface energy minimization and strain energy minimization [10]. In case of Cu films the former favours the formation of a {111} texture while the latter favours a {100} texture [2, 10-12]. A detailed investigation of the microstructures possible in sputter deposited films (20 to 250 μm thick) had been conducted by Thornton [13] in 1975. In a structure zone model (SZM) the evolution of the microstructure with sputtering pressure and homologous temperature, T/T_m , is characterised by four structure zones (1, T, 2, 3). At low temperatures the structures that develop are characterised by the kinetics of the adatoms on the substrate surface whereas at high temperatures large equiaxed-like structures determined by bulk diffusion develop. A revised SZM was subsequently offered by Messier *et al* [14] in which the sputtering pressure axis was replaced by a parameter proportional to the kinetic energy of the arrival particles, so as to highlight the combined impact of thermal and kinetic energy-induced mobility of the particles on the evolved microstructure.

Bai *et al* [15] noted that the effect of substrate roughness was ignored in the SZM. They reported corresponding observations for Cu films deposited by partially ionised beam (PIB) technique on smooth SiO_2 substrates and on rough Al_2O_3 substrates. It was found that substrate surface roughness promotes the development of columnar structures. Columnar structures can develop when the surface mobility of deposited atoms is limited.

In this study, properties as discussed above of thin (500 nm and 1000 nm) and ultrathin (5 nm) Cu films on two different types of amorphous substrates (SiO_2 and Si_3N_4) have been investigated as functions of production variables.

2. Experimental

2.1 Film Production

Copper films with thicknesses of 5 nm, 500 nm and 1000 nm were produced by magnetron sputter deposition on two commercially available Si type amorphous substrates. The substrates are: 500 μm Si (510)/50 nm SiO_2 and 500 μm Si (100)/50 nm SiO_2 /50 nm Si_3N_4 with the SiO_2 and Si_3N_4 layers being amorphous. Both substrate types were used in the as-received state and sputter cleaned conditions. Substrate sputter cleaning was performed for 3 min at 0.2 mA with Ar ions accelerated at three different voltages (200 V, 500 V and 1000 V). All the batches of films were produced under

Ultra High Vacuum conditions ($\sim 4 \times 10^{-8}$ Pa base pressure) in a load-lock system at a deposition temperature of 100 °C, 200 W working power, a deposition rate of approximately 1.2 nm/sec with the specimen holder rotating at 100 rpm. The film deposition variables were: the argon ion acceleration voltage during substrate sputter cleaning and the working gas (Argon) pressure. Details of the batch-wise production Cu films have been listed in Table 1.1.

The concentrations of species at the substrate surface were determined by an Auger Electron Spectroscopy (AES) system using a double-pass cylindrical mirror analyzer (Perkins-Elmer, 15-255G) at an electron acceleration voltage of 3 keV, coupled to the film deposition chamber without breaking the vacuum between film deposition and AES analysis.

Table 1.1. List of production conditions for Cu films showing; batch No (B#), substrate type (O and N for SiO₂ and Si₃N₄ respectively) and sample No. ST: substrate type, CV: substrate cleaning voltage, WP: working gas (Ar) pressure.

Sample code (thickness)	ST	CV (V)	WP (10^{-2} Pa)
B1O1 (0.50 μ m)	SiO ₂	200	5
B1O2 (0.50 μ m)	SiO ₂	200	22
B1O3 (0.50 μ m)	SiO ₂	200	69
B1O2b-annealed 350 °C	SiO ₂	200	22
B1O2c-annealed 400 °C	SiO ₂	200	22
B1O2d-annealed 450 °C	SiO ₂	200	22
B2N1 (0.50 μ m)	Si ₃ N ₄	200	5
B2N2 (0.50 μ m)	Si ₃ N ₄	200	10
B2N3 (0.50 μ m)	Si ₃ N ₄	200	22
B2N4 (0.50 μ m)	Si ₃ N ₄	200	46
B2N5 (0.50 μ m)	Si ₃ N ₄	200	69
B3O1 (1 μ m)	SiO ₂	200	5
B3O2 (1 μ m)	SiO ₂	200	69
B3O3 (0.5 μ m)	SiO ₂	200	69
B3N1 (1 μ m)	Si ₃ N ₄	200	5
B3N2 (1 μ m)	Si ₃ N ₄	200	69
B3N3 (0.5 μ m)	Si ₃ N ₄	200	69

B4O1 (0.5 μ m)	SiO ₂	No cleaning	46
B4O2 (0.5 μ m)	SiO ₂	200	46
B4O3 (0.5 μ m)	SiO ₂	500	46
B4O4 (0.5 μ m)	SiO ₂	1000	46
B4O5 (0.5 μ m)	SiO ₂	200	9.7
B4N1 (0.5 μ m)	Si ₃ N ₄	No cleaning	46
B4N2 (0.5 μ m)	Si ₃ N ₄	200	46
B4N3 (0.5 μ m)	Si ₃ N ₄	500	46
B4N4 (0.5 μ m)	Si ₃ N ₄	1000	46
B4N5 (0.5 μ m)	Si ₃ N ₄	200	9.7
B5O1 (5 nm)	SiO ₂	No cleaning	46
B5O2 (5 nm)	SiO ₂	200	46
B5O3 (5 nm)	SiO ₂	500	46
B5N1 (5 nm)	Si ₃ N ₄	No cleaning	46
B5N2 (5 nm)	Si ₃ N ₄	200	46
B5N3 (5 nm)	Si ₃ N ₄	500	46

2.2 X-ray diffraction

$\theta/2\theta$ scans: The films in Tab.1.1 were analyzed for texture using a PHILIPS MPD diffractometer (in the Bragg-Brentano diffraction geometry) with the X-ray tube operating at 45 kV and 40 mA. X-rays were generated from a Cu tube. The diffraction optics comprises a monochromator in the incident beam path to select Cu $K\alpha_1$ radiation, an incident beam mask of 10 mm and a divergence slit of 0.25°. In the diffracted beam path an anti-scatter slit of 0.25°, a receiving slit of height 0.3 mm and a proportional detector were used.

Pole figures and stress measurements: Pole figure measurements of the Cu 111 reflection were performed on a PHILIPS X'Pert MRD diffractometer equipped with a Eulerian cradle (four-circle goniometer). Cu $K\alpha$ radiation emerging from the point focus of a sealed X-ray tube operated at 45 kV and 40 mA was converted into a quasi-parallel beam by commercially available X-ray lens. The measurement directions are defined by a rotation angle ϕ around the sample normal and a tilt angle ψ with respect to the sample normal. Stress determinations were based on 2θ scans of the Cu 111

reflection for the 5 nm thick films and of the Cu 311 reflection for the 500 nm and 1000 nm thick films at various specimen tilt angles ψ .

2.3 Morphology

The microstructure of the films was investigated by Transmission Electron Microscopy (TEM), Focussed Ion Beam (FIB) and Atomic Force Microscopy (AFM) techniques.

TEM: A JEM JEOL 2000FX TEM device operating at an electron beam acceleration voltage of 200 kV was used. The investigated TEM foils were prepared by mechanical thinning and ion milling.

FIB imaging: A FEI FIB 200 microscope operating at 12 pA and 30 keV with a Ga^+ beam was used. Here imaging was realized by the detection of secondary electrons. Image appreciation stems from orientation of individual crystallites relative to the incident beam direction, causing large variations (due to ion-channelling contrast) in the ion-induced secondary electrons emission and hence enabling pronounced crystallographic contrast to be observed. Grains with their low index crystallographic planes parallel to the ion beam appear dark while higher index crystallographic planes appear lighter under special orientations.

AFM: A Digital Instruments Atomic Force Microscopy (AFM) device operating in the tapping mode, with Si tip cantilevers of 5-10 nm nominal curvature and a resonance frequency of 296-358 KHz was used to determine the roughness of the substrates and the surface morphology of the ultrathin Cu films. The roughness was represented as root mean square (rms) values (defined by the standard deviation of the height distribution) determined over an area of $10\ \mu\text{m} \times 10\ \mu\text{m}$.

The sizes of grains were determined from the TEM and FIB images by the linear intercept method calculating the mean linear intercept [16].

3 Results and Discussion

3.1. Substrate cleaning

3.1.1 Substrate roughness.

Figure 1.1 shows the rms roughness for the film-free substrates as determined from the AFM investigations. In the as-received condition the SiO_2 substrate is rougher than the Si_3N_4 substrate. Upon sputter cleaning the roughness was found to follow the same trend for both substrates: cleaning at 200 V gave rise to a smoothing of the substrate surfaces, suggesting that part of the roughness of the uncleaned substrates is due to surface contaminants (see below). At 500 V the roughness increases, most likely resulting from the development of defects at the surface due to bombardment by the sputtering ions. The roughness of the substrates after cleaning at 1000 V is lower than after cleaning at 500 V.

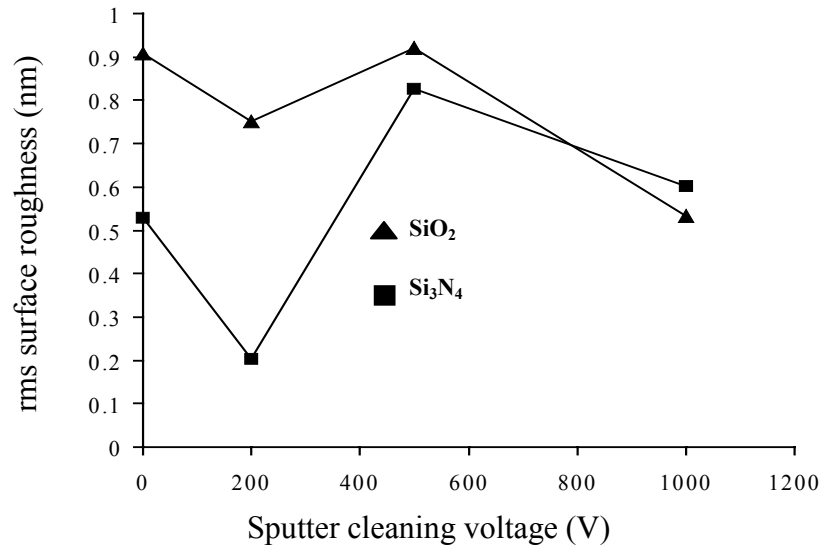


Figure 1.1. Graph of rms surface roughness of SiO₂ and Si₃N₄ substrates sputter cleaned at various ion acceleration voltages. The lines are drawn as guide to the eye.

3.1.2 Substrate surface composition

Results of the AES investigation are depicted in Fig. 1.2. By assuming a homogenous layer, the atomic concentrations were determined through a normalization procedure using a PHI MultiPak software for data treatment [17]. Contaminants, mainly oxygen (on the Si₃N₄ substrate) and carbon, were observed to be present on both substrate surfaces prior to sputter cleaning.

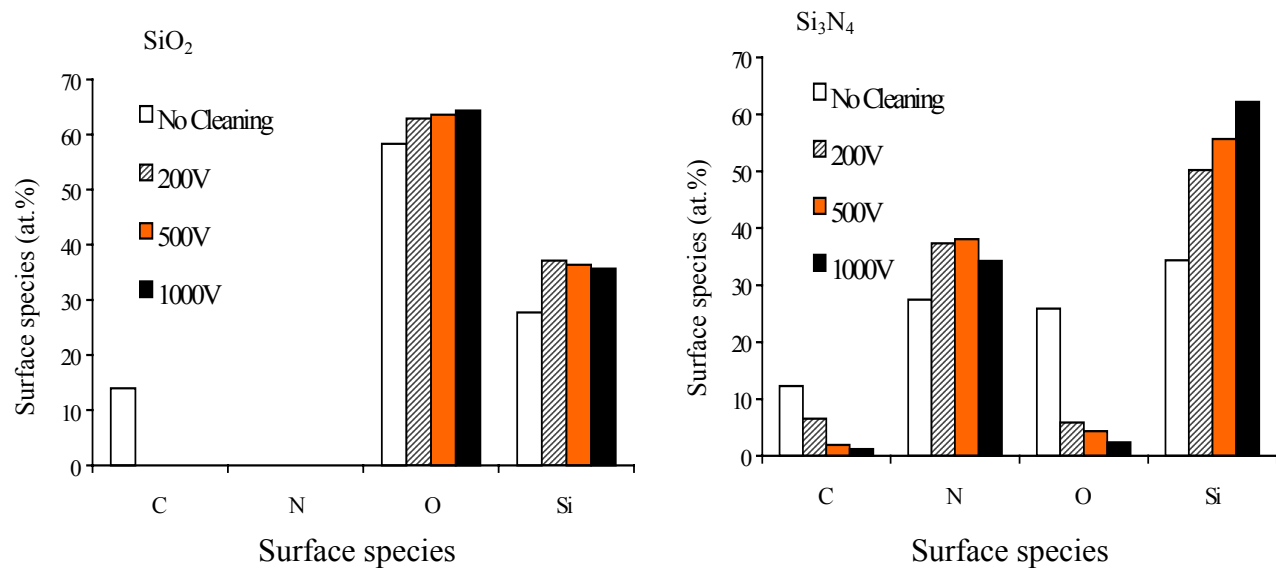


Figure 1.2. Concentration of surface atomic species on the SiO₂ and Si₃N₄ substrates for different sputter cleaning conditions.

Upon sputter cleaning of the Si_3N_4 surface the concentration of these contaminants decreased gradually with increase in sputtering ion voltage, whereas for the SiO_2 substrates carbon (the only observed contaminant) was completely eliminated from the surface already after sputter cleaning at 200 V.

3.2 Texture

The texture of the Cu films has been investigated using X-ray diffraction methods because this in contrast to TEM, offers a faster information gathering procedure, is non-destructive and specimen preparation is not elaborate.

3.2.1 $\theta/2\theta$ scans:

Intensity data treatment was carried-out using the PHILIPS ProFit peak fitting procedure with the Pseudo-Voigt function [18]. By this the characteristic parameters of the individual peaks were evaluated: position, integrated intensity, integral breadth, peak shape (Lorentzian-Gaussian) and asymmetry.

Examples of $\theta/2\theta$ scans for the Cu films deposited on SiO_2 and Si_3N_4 substrates are shown in Fig. 1.3 and Fig. 1.4 for variations in working gas (Ar) pressure and substrate cleaning conditions respectively. The measurements were abridged due to the strong 400 reflection from the single crystal Si 100 wafer occurring at $2\theta = 69^\circ$ so as to protect the detector from damage.

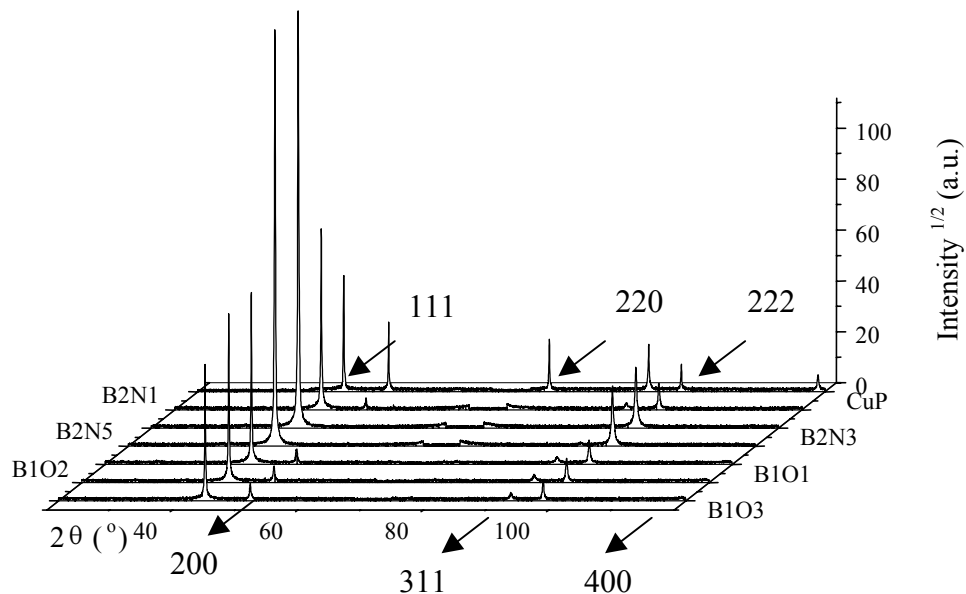


Figure 1.3. $\theta/2\theta$ scans for copper films deposited on SiO_2 (series B1) and Si_3N_4 (series B2) substrates at different deposition gas (Ar) pressures (Table 1.1). Included for comparison is a scan for a Cu-powder sample (CuP).

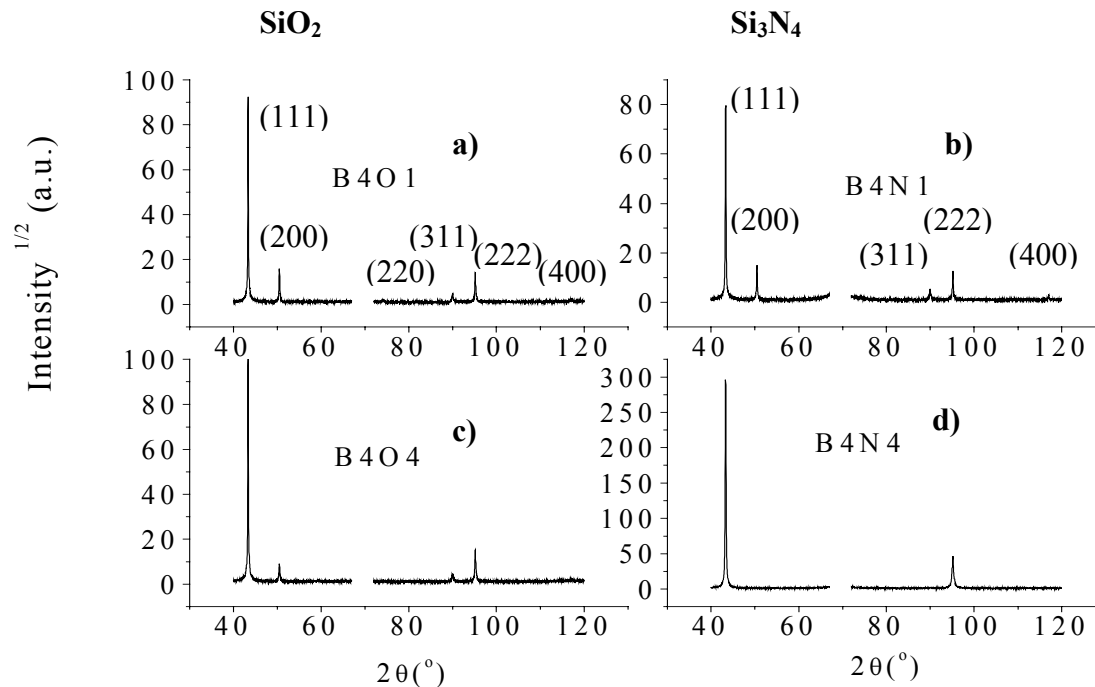


Figure 1.4. $\theta/2\theta$ scans for Cu films (from series B4) deposited on SiO_2 and Si_3N_4 substrates at a), b): no substrate cleaning, c), d): substrate cleaning at 1000 V.

All the films were found to exhibit a pronounced $\{111\}$ texture as can be seen by comparison with the XRD pattern for the Cu-powder sample (Fig. 1.3). The intensities of the reflections 200, 220 and 311 depend on the type of substrate (SiO_2 or Si_3N_4) on which the Cu films are deposited and the sputtering conditions at which deposition was performed. A complete quantitative description of the texture on the basis of $\theta/2\theta$ scans is not possible, this requires pole figure scans and the evaluation of the orientation distribution function [19-21]. However it is possible to perform a useful characterisation of texture using the integrated intensities of the Bragg peaks from a $\theta/2\theta$ scan where the diffracting planes are parallel to the sample surface. Frequently, such characterisations are done (for fcc metals with a $\{111\}$ texture) by regarding the intensity ratio $I_{111} : I_{200}$ of the 111 and 200 peaks [5, 22-25]. This already provides a quick method, however it does not take into account the reflections 220 and 311 and does not indicate if an increase of the ratio is due to an increase of the 111 peak or a decrease of the 200 peak, or both.

In the following, the Harris method is adopted [26]. Numbers for the strength of the texture are determined from the direct comparison of the integrated peak intensities of a textured Cu film with those of an untextured Cu-powder sample.

The technique requires performing a $\theta/2\theta$ scan of the specimen within a user defined scan range. The integrated intensities obtained by the fitting of Pseudo Voigt functions to the measured diffraction lines were corrected for absorption [27]. The corrected intensities of the individual peaks (I_i^s) are then normalised with those from a powdered specimen of the same material using corresponding peaks (I_i^p):

$$F_i = I_i^s / I_i^p \quad (1.1)$$

This normalisation takes into account those influences on the measured peak intensities, which do not depend on the volume fractions of the different textured components, i.e. the multiplicity, the atomic form factor, the Lorentz-polarisation factor and possible instrumental effects. F_i is then normalised to eliminate the effects of the power of the instrument and the irradiated sample volume, according to:

$$T_i = \left(F_i / \sum_{i=4} F_i \right) 100\% \quad (1.2)$$

T_i is a relative measure for the volume fractions of the crystallites oriented with specific hkl planes parallel to the film surface (for an untextured Cu film T_i for the 111, 200, 220 and 311 are each 25%).

Results for the fractions T_i as obtained with this procedure for the different Cu films are presented in Figs. 1.5 – 1.8.

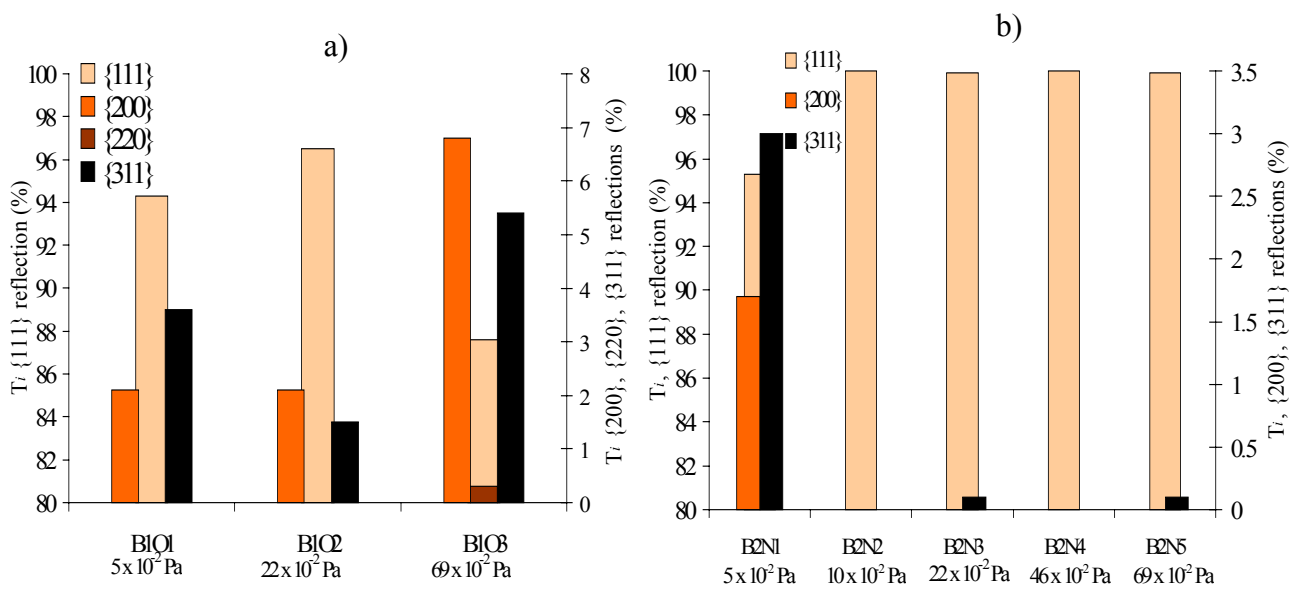


Figure 1.5. Fractions T_i of the texture components in 500 nm thick Cu films deposited at different Ar flows on (a) SiO₂ (series B1) and (b) Si₃N₄ (series B2) substrates. The left-hand scale is for the 111 reflection and the right-hand scale for the 200 and 220 and 311 reflections.

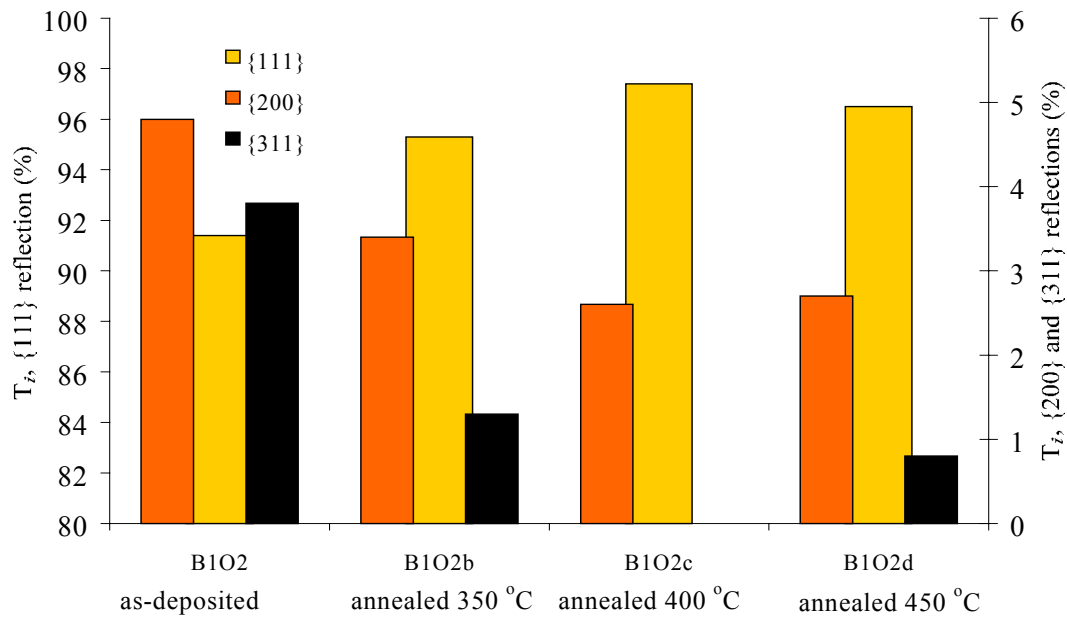


Figure 1.6. Fractions T_i for Cu films in as-deposited and annealed conditions on SiO_2 substrates (series B1).

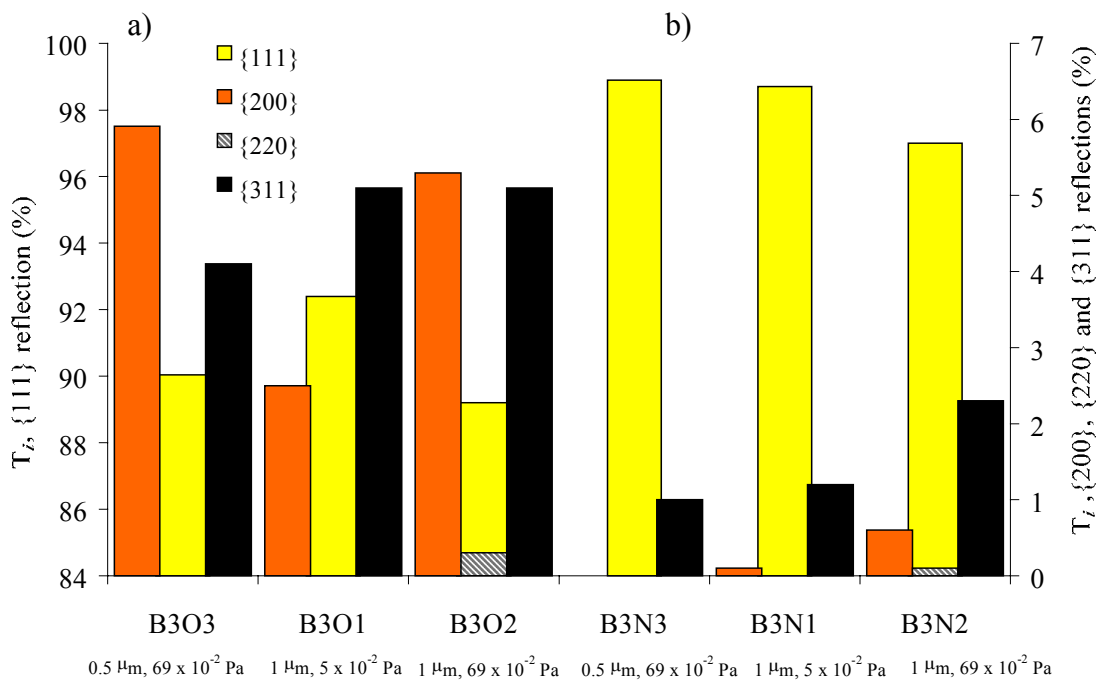


Figure 1.7. Fractions T_i for Cu films of 0.5 μm and 1 μm thickness and two different deposition pressures on (a) SiO_2 (series B3O) and (b) Si_3N_4 (series B3N) substrates.

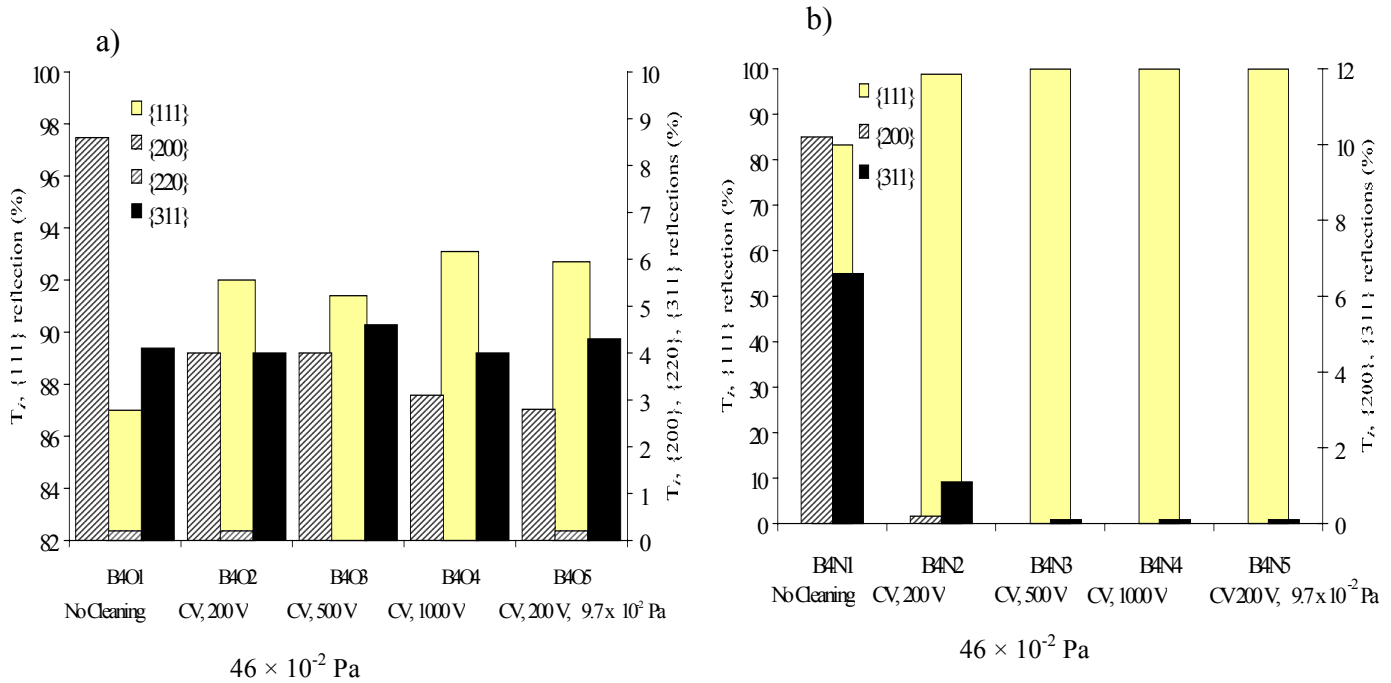


Figure 1.8. Fractions T_i for 500 nm thick Cu films deposited on (a) SiO₂ (series B4O) and (b) Si₃N₄ (series B4N) substrates in the as-received and sputter cleaned conditions.

From Figs. 1.5 – 1.8, it follows that the fraction T_{111} is greater than 90% for all the Cu films, indicating a strong {111} texture. The fractions T_{200} and T_{311} are in the range of a few percent and found to depend on the details of the production of the films. It is noteworthy that the fraction T_{220} is either far below 1% or below the detection limit in all of the B#N series and in the B#O series of specimens, except the series B1O. To satisfy the random case, the intensity ratio $I_{220} : I_{311}$ should equal the value given by the Cu powder measurements, i.e. $I_{220}^r : I_{311}^r = 0.94$ (c.f. Fig. 1.3). As this is not observed, it can be concluded that no random texture component exists in the sputtered Cu films, i.e., the minor components, 200 and 311, do not belong to a random component.

The following observations can be made in Figs. 1.5 – 1.8:

(i) Films sputter deposited on Si₃N₄ substrates show a somewhat stronger {111} texture than films sputter deposited on SiO₂ substrates (Fig. 1.3).

(ii) For films deposited on SiO₂ substrates, an increase of the Ar pressure leads to a decrease of the texture strength (Fig. 1.5a), whereas for films deposited on Si₃N₄ substrates, an increase is indicated (T_{111} attains 100% and accordingly the {200} and {311} components disappear, Fig. 1.5b).

(iii) Post-deposition annealing of a Cu film deposited on SiO₂ substrate leads to an increase of the {111} texture, however without T₁₁₁ attaining 100% (Fig. 1.6).

(iv) Increasing the film thickness leads to a slight decrease of the {111} texture in the films deposited on both SiO₂ and Si₃N₄ substrates. Together with the {200} and {311} components, there was also the presence of the {220} component in the thicker films (Figs. 1.7a and b). Decreasing the deposition gas flow for the growth of the thicker films (1 μm), the {111} texture becomes stronger (T₁₁₁ increases) for films on both substrates. This compares well with the results for the 500 nm films on SiO₂ (Fig. 1.5a, 69×10⁻² Pa and 5×10⁻² Pa) however not for the 500 nm films on Si₃N₄ (Fig. 1.5b).

(v) Sputter cleaning of the SiO₂ substrates prior to film deposition has marginal effects on the {111} texture; a slight increase is observed for Cu 111 upon substrate cleaning at 200 V and this does not change when cleaning is performed at higher voltages (Fig. 1.8a). Sputter cleaning of the Si₃N₄ substrate leads to an increase of the {111} texture up to practically 100% (Fig. 1.8b).

Despite the valuable texture information that can be extracted from the $\theta/2\theta$ scans, the method outlined above has its inherent limitations. Symmetric $\theta/2\theta$ scans record intensity at zero tilt angle, $\psi = 0^\circ$, i.e. only from hkl planes parallel to the sample surface (in reality a finite range about $\psi = 0^\circ$ is covered, due to the resolution of the instrument). Hence for the case of a broad distribution in texture, i.e. with some hkl planes, belonging to the considered hkl texture component, tilted away from the fibre axis at $\psi = 0^\circ$, the sharpening of this distribution (e.g. during annealing of the film) would be attributed, by a $\theta/2\theta$ scan, to an increase of the volume fraction of the texture component. Therefore the fraction T_i introduced above presents a measure of the degree of texture, but not necessarily the volume fraction of the texture component. Hence pole figure scans are required.

3.2.2 Pole - figure scans

Pole figures, $I(\varphi, \psi)$, showed that all Cu films had a fibre texture (no dependence on the rotation angle φ occurred).

Figure 1.9 shows ψ scans (111 reflection) for 500 nm thick Cu films deposited on SiO₂ and Si₃N₄ substrates at various deposition gas pressures (series B1O and B2N). These $I(\psi)$ functions have been corrected for background, absorption, thickness and intensity loss due to geometric effects [28]. Hence they allow a direct comparison of films with different thickness or different illuminated area.

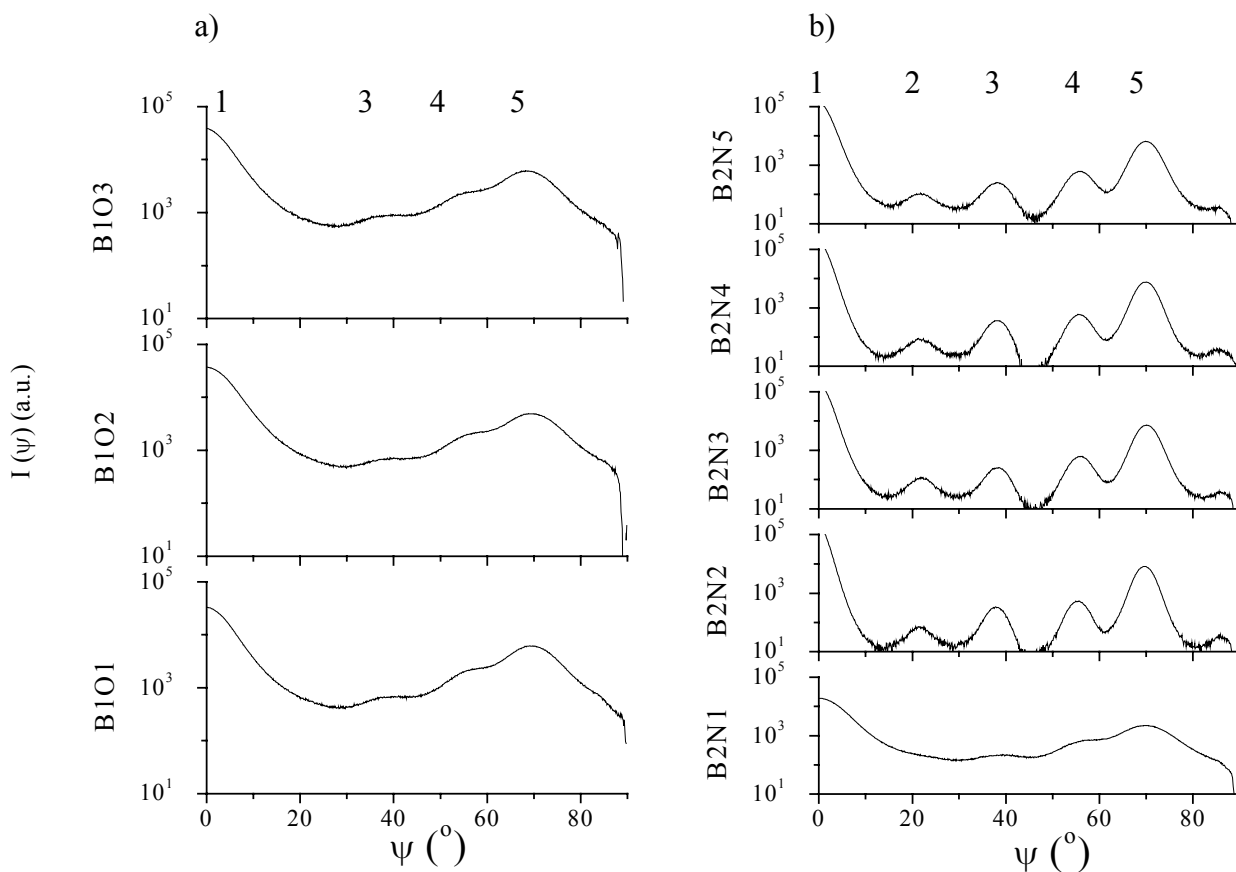


Figure 1.9. Cu films (series B1 and B2) sputter deposited at different Ar pressures (Table 1.1); pole figure sections for the Cu 111 reflection. (a) sputtered on SiO_2 substrates, (b) sputtered on Si_3N_4 substrates. Note the logarithmic scale of $I(\psi)$. (The break in the curve for specimen B2N4 is due to negative intensities resulting from the correction for background)

The scans exhibit 5 peaks, which appear much more pronounced for the films on Si_3N_4 substrates than for the films SiO_2 substrates. The peaks #1, at $\psi=0^\circ$, and #5, at $\psi=70.5^\circ$, belong to the $\{111\}$ texture component. Peaks #3 and #4 result from twinning on the 111 planes (theoretical $\psi = 38.94^\circ$ and 56.25°) leading to a texture component with 511 planes parallel to the film surface. This texture component also contributes to the peak #5 at $\psi=70.5^\circ$ [1]. Multiple twinning generates peak #2 at $\psi=22^\circ$ [1]. This peak is visible for the Si_3N_4 based films only; however its absence in the SiO_2 based films may be due to its non-existence or due to the smearing out of the profile. (The same notation, #, has been used to describe the peaks in all the ψ plots presented in this report)

For a quantitative evaluation of the ψ scans a peak fitting algorithm was developed adopting Pearson VII functions for the individual peaks, $I_i(\psi)$, composing the function $I(\psi)$ in the pole figure

scan and a constant plateau level to account for a possible random fraction. In order to allow for the fitting of peak #1, the experimental $I(\psi)$ was supplemented by a range of negative ψ values by mirroring with respect to the ordinate. A relative measure of the fractions of the texture components was obtained by calculating the peak areas using [29]

$$A_i = \int_{0^\circ}^{90^\circ} I_i(\psi) \sin \psi d\psi \quad (1.3)$$

and normalizing by

$$A_i^n = A_i / \sum_{i=1}^N A_i \quad (N=5) \quad (1.4)$$

This quantitative evaluation by fitting allows for addressing two important points, (i) the existence of a random fraction and (ii) the texture strength and sharpness.

Random fraction. Frequently in literature the minimum intensity in the $I(\psi)$ plot has been taken as the level of the contribution from a random fraction of crystallites, $I_r = \text{constant}$ [30-32]. However, in case of broad overlapping peaks (Fig. 1.9a) this procedure may not be suitable because $I(\psi)$ then may never attain the level I_r . Adopting this procedure may result in an incorrect texture characterisation since exaggerated I_r values are obtained. Taking the minimum of the $I(\psi)$ functions in Fig. 1.9 as level of I_r yields a random fraction, which is higher for the films on SiO_2 substrates than for those on Si_3N_4 substrates by a factor in the order of about 20. This setback has been addressed by the fitting procedure adopted in this study.

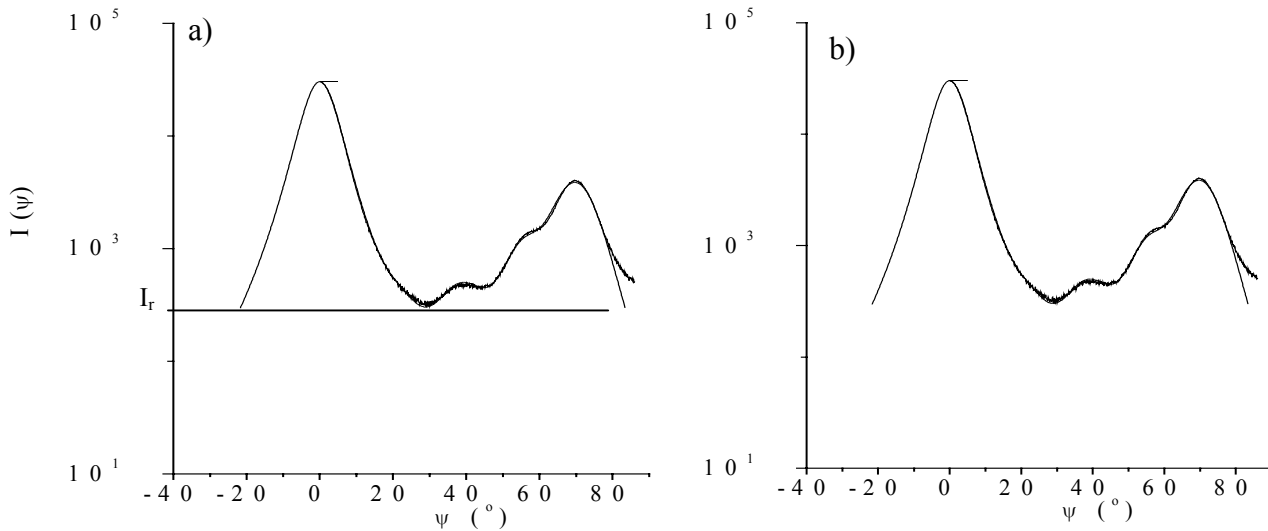


Figure 1.10. $I(\psi)$ for a Cu film on SiO_2 substrate, (.....) experimental, a) (—) fit with random fraction, I_r , b) (—) fit with $I_r = 0$.

Figure 1.10 shows fits to an experimental $I(\psi)$, where in one case the background fit parameter had been enabled free (a) and the other with the parameter set fixed at $I_r = 0$ (b). Apparently fits of the same quality were possible, irrespective of fit mode of I_r , and it has to be concluded that the pole figure scans do not reveal either the presence or absence of a random fraction of crystallites in the Cu films on the SiO_2 and Si_3N_4 substrates. Comparing this to the $\theta/2\theta$ procedure adopted above, where a random fraction was excluded based on the absence of the 220 reflection, it can be stated that it may be rather a $\theta/2\theta$ scan than a pole figure scan which permits the detection of a random component. Therefore the fit in Fig. 1.10b correctly accounts for the texture state of the film.

Texture strength and sharpness from fit. The fitting was performed with the background fit parameter set fixed, at $I_r = 0$, i.e. excluding a random fraction. The results from the fitting of the measured $I(\psi)$ in Fig. 1.9 are listed in Table 1.2.

Table 1.2. Fractions A_i^n and HWHM (in square brackets) for texture components from Cu 111 pole figure plots (Fig. 1.9). m = multiplicities of the peak.

Specimen Peak No	#1 {111} $m=1, [^\circ]$	#2 {5 7 13} $m=1, [^\circ]$	#3 {511} $m=1, [^\circ]$	#4 {511} $m=2, [^\circ]$	#5 {511} + {111} $m=1, [^\circ], m=3$
B1O1, 5×10^{-2} Pa	17.0 [4.6]	1.00 [6.0]	5.54 [7.3]	14.8 [6.2]	61.7 [6.2]
B1O2, 22×10^{-2} Pa	17.0 [4.8]	0.53 [4.3]	6.50 [9.0]	14.8 [5.5]	61.2 [5.9]
B1O3, 69×10^{-2} Pa	20.3 [5.0]	1.73 [8.5]	5.50 [8.0]	10.2 [5.0]	62.3 [6.5]
B2N1, 5×10^{-2} Pa	19.4 [4.3]	1.34 [6.0]	5.15 [7.0]	11.6 [5.0]	62.5 [5.6]
B2N2, 10×10^{-2} Pa	17.3 [1.3]	0.53 [3.5]	2.50 [2.1]	4.90 [2.1]	74.8 [1.9]
B2N3, 22×10^{-2} Pa	19.7 [1.6]	0.90 [3.6]	2.10 [2.4]	6.00 [2.5]	71.5 [2.1]
B2N4, 46×10^{-2} Pa	17.8 [1.5]	0.71 [4.6]	2.73 [2.2]	5.30 [2.4]	73.5 [2.1]
B2N5, 69×10^{-2} Pa	19.7 [1.8]	0.95 [3.9]	2.44 [2.9]	6.01 [2.7]	71.0 [2.2]

Volume fractions of oriented crystallites are given by the A_i^n in Table 1.2 and the sharpness of the distribution by the HWHM of the peaks in the pole figure scans. The strength of the {111} texture, S_{111} , is defined as the volume fraction of (111) oriented crystallites. A measure for this is given by the peaks #1 and the {111} contribution to peak #5 in Fig. 1.9:

$$S_{111} = A_1^n + A_{5,111}^n \quad (1.5)$$

However, because of the overlap of the {111} contribution and the {511} contribution to peak #5, Eq. (1.5) cannot be used and hence only the peak #1 is taken as a *relative* measure, $S_{111}^r = A_1^n$, for the strength of the {111} texture. The values of A_{111}^n in Table 1.2 show a non-systematic nature of the spread. Within this spread the values of A_{111}^n are the same for all films in Table 1.2. Hence the strength of the {111} texture is about the same for Cu films on both SiO_2 and Si_3N_4 and does not

depend systematically on the Ar pressure during deposition. However the texture is sharper for the Si_3N_4 based films. In this context it is recalled that the variation of the T_{111} fraction (c.f. section 3.2.1), as derived from the $\theta/2\theta$ scans (i.e. at $\psi=0$), could be due to a variation of either the strength or the sharpness of the $\{111\}$ texture. The fractions of the $\{511\}$ texture twins (responsible for both peaks #3 and #4) are higher for the SiO_2 based films, where the ratio $A_4^n : A_3^n$ around 2 accords to the value as expected from the multiplicities of these reflections. Noting that the contribution $A_{5,111}^n$ ($m=3$) to the peak #5 should be 3 times the peak $A_{1,111}^n$ ($m=1$), the contribution $A_{5,511}^n$ from the $\{511\}$ twins to this peak can be estimated by $A_{5,511}^n = A_5^n - 3A_1^n$ to be around 7 for the films on SiO_2 substrates (and B2N1 on Si_3N_4) while for the films on Si_3N_4 substrates the estimated fractional volume contribution $A_{5,511}^n$ was 14. For the films on SiO_2 substrates, this value is in fair accordance with peaks #3 ($m=1$) and #4 ($m=2$) whereas for the films on Si_3N_4 substrates, the value of $A_{5,511}^n$ around 14 is much higher than the value between 2 and 3 as expected from peaks #3 and #4. The reason for this observed higher intensity of peak #5 is not clear.

3.2.2.1 Annealing effect

Figure 1.11 shows the $I(\psi)$ plots for the 111 reflection of a 500nm thick Cu film on SiO_2 substrate in the as-deposited state and after annealing at 450 °C for 30 min.

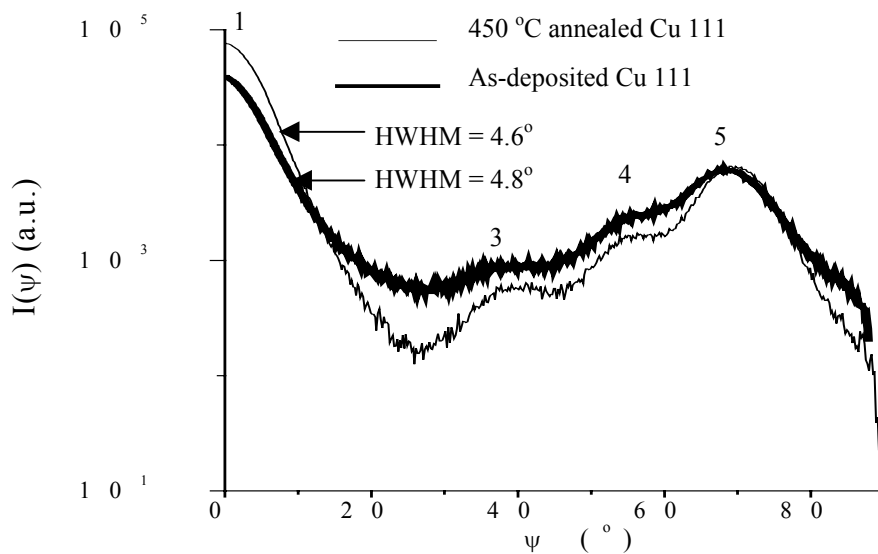


Figure 1.11. Cu-film on SiO_2 substrate (samples B1O2 and B1O2d in Table 1.1): pole figure sections $I(\psi)$ before and after annealing at 450 °C.

Annealing leads to an increase of the $\{111\}$ texture strength (increase of A_i^n by a factor of 2) but did not appreciably affect the sharpness (compare HWHM for both specimens) of this texture. However, the texture of the twin components shown at peaks #3 and #4 seems to become sharper.

3.2.2.2 Thickness effect

The Cu (111) pole figure scans for the films from the B3 series of specimens are plotted in Fig.1.12. A comparison of the 0.5 μm thick films B3O3 and B3N3 with the corresponding 1 μm thick films B3O2 and B3N2 shows that the occurrence of a sharper texture of the films on Si_3N_4 than of the films on SiO_2 does not depend on the film thickness. This indicates that the quality of the $\{111\}$ texture of the Cu films as associated with the type of substrate prevails throughout the film during its growth. The observation that the texture of the 0.5 μm thick films does not depend on the pressure during deposition (section 3.2.2.1, Fig. 1.9) can be made also for the 1 μm thick films in Fig. 1.12, where films deposited at 5×10^{-2} Pa and 69×10^{-2} Pa are compared.

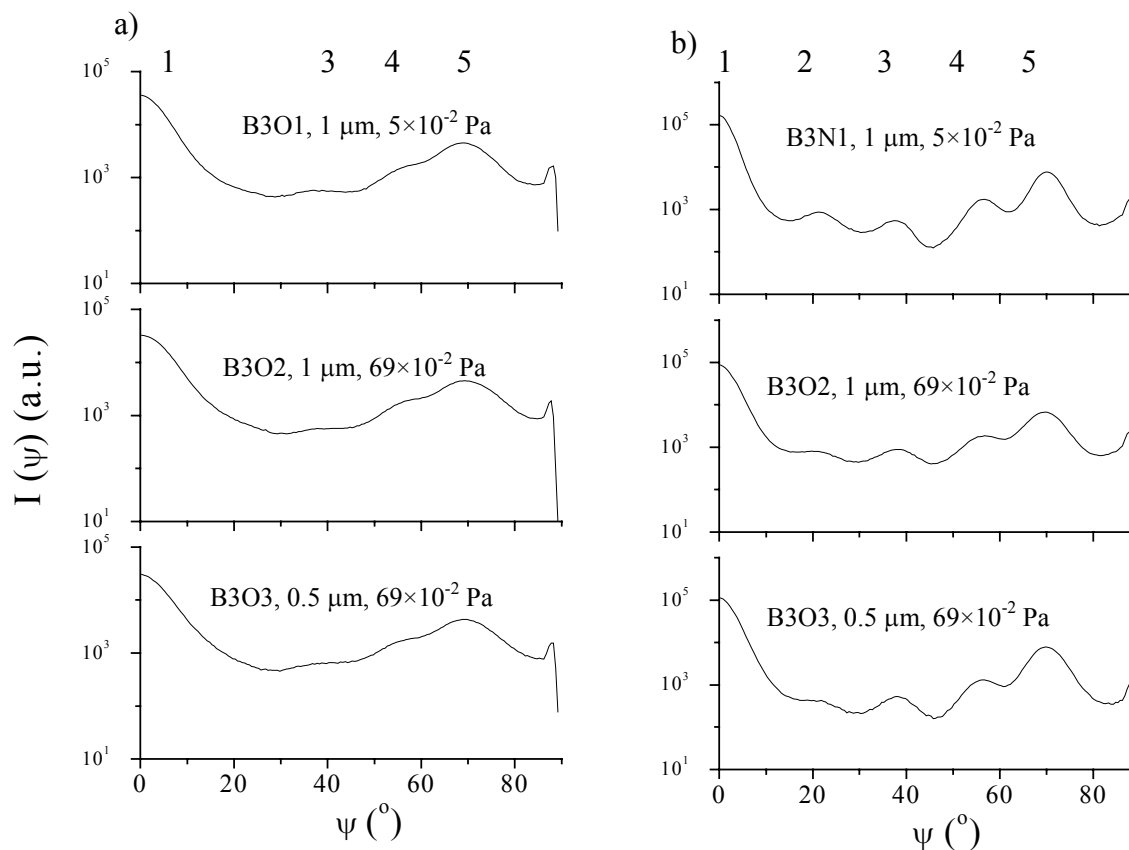


Figure 1.12. Cu films of different thickness sputter deposited on (a) SiO_2 and (b) Si_3N_4 at different Ar pressures.

3.2.2.3 Substrate cleaning effect

500 nm films: Pole figure sections, $I(\psi)$, for Cu films grown on SiO_2 and Si_3N_4 substrates (series B4) after different sputter cleaning conditions are presented in Fig. 1.13.

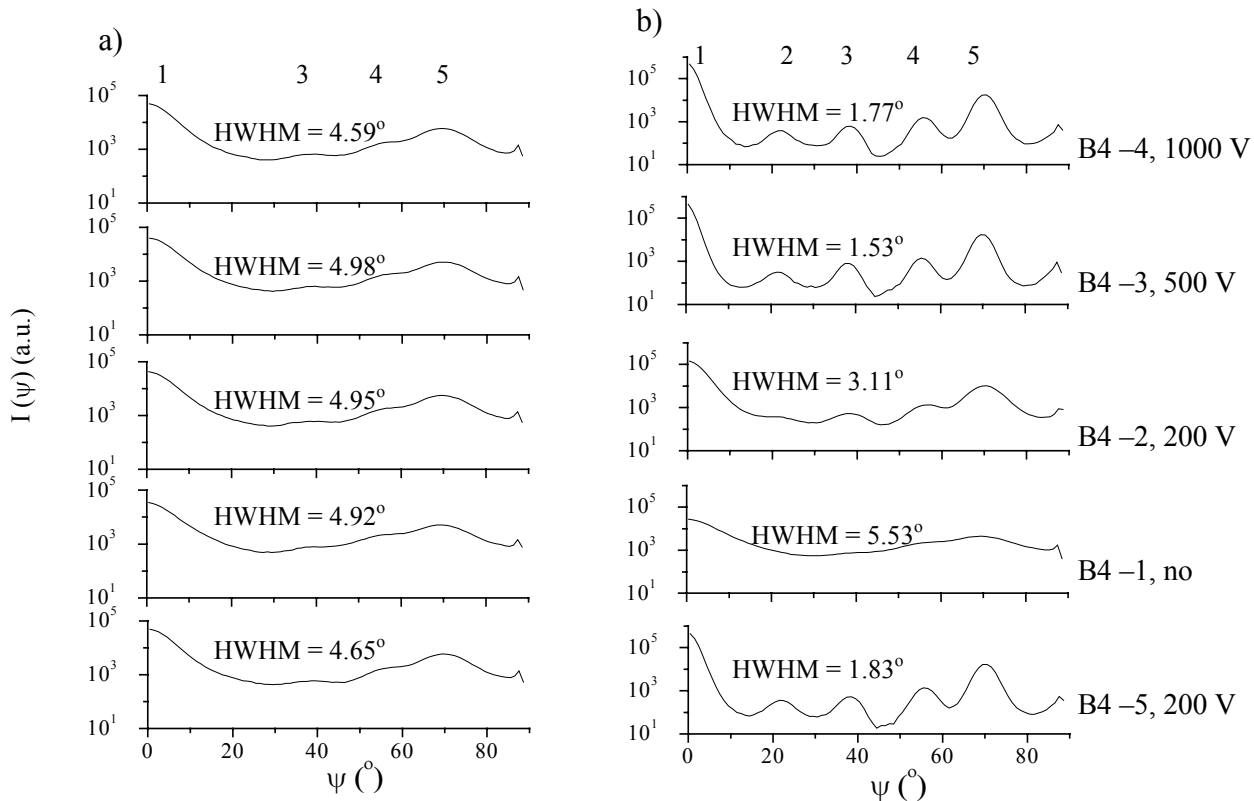


Figure 1.13. Pole figure plots $I(\psi)$, of Cu films sputter deposited at 46×10^{-2} Pa without substrate cleaning (no) and after cleaning at different voltages (see Table 1.1 for details of B4 series specimens). (a) sputtered on SiO_2 , (b) sputtered on Si_3N_4 . Samples B4-5 were deposited at lower Ar pressure, 9.7×10^{-2} Pa. The half width at half maximum is indicated for the peak #1.

The observed features of the film texture in the plots are the same for uncleaned SiO_2 and Si_3N_4 substrates. Cleaning of the SiO_2 substrates prior to film deposition practically does not affect the texture of the films (although a very slight sharpening of the peaks may be observed). In contrast, cleaning of the Si_3N_4 substrates has a strong effect on the texture. The peaks sharpen with increasing voltage up to 500 V and remain unchanged with further increase from 500 V to 1000 V. It is interesting to note that at 200 V pre-cleaning and at a lower deposition gas (Ar) pressure (9.7×10^{-2} Pa, B4N5), the texture becomes sharper than at a higher Ar pressure (46×10^{-2} Pa, B4N2). This

can be explained by the higher energy of the particles (Ar reflected from the cathode and/or Cu) at lower Ar pressure bombarding the substrate which (in addition to the pre-cleaning by Ar ions) causes a cleaning effect on the surface during the first stages of the film deposition.

Ultrathin films: The texture analysis for the ultrathin Cu films grown on as-received and sputter cleaned SiO_2 and Si_3N_4 substrates was only possible using the pole figure method. This is due to the absence of sufficient reflections required for the application of the $\theta/2\theta$ method (as described in section 3.2.1 above); only the 111 reflection was detectable in the $\theta/2\theta$ scan. Fig. 1.14 shows the pole figure scans. For films deposited on cleaned Si_3N_4 substrates the sharpness of the {111} texture increased with increasing cleaning voltage, whereas for the uncleaned Si_3N_4 substrates and the for all films on SiO_2 substrates, no discernible texture component was observed. Obviously substrate type and cleaning condition both have significant influences on the texture state of the films.

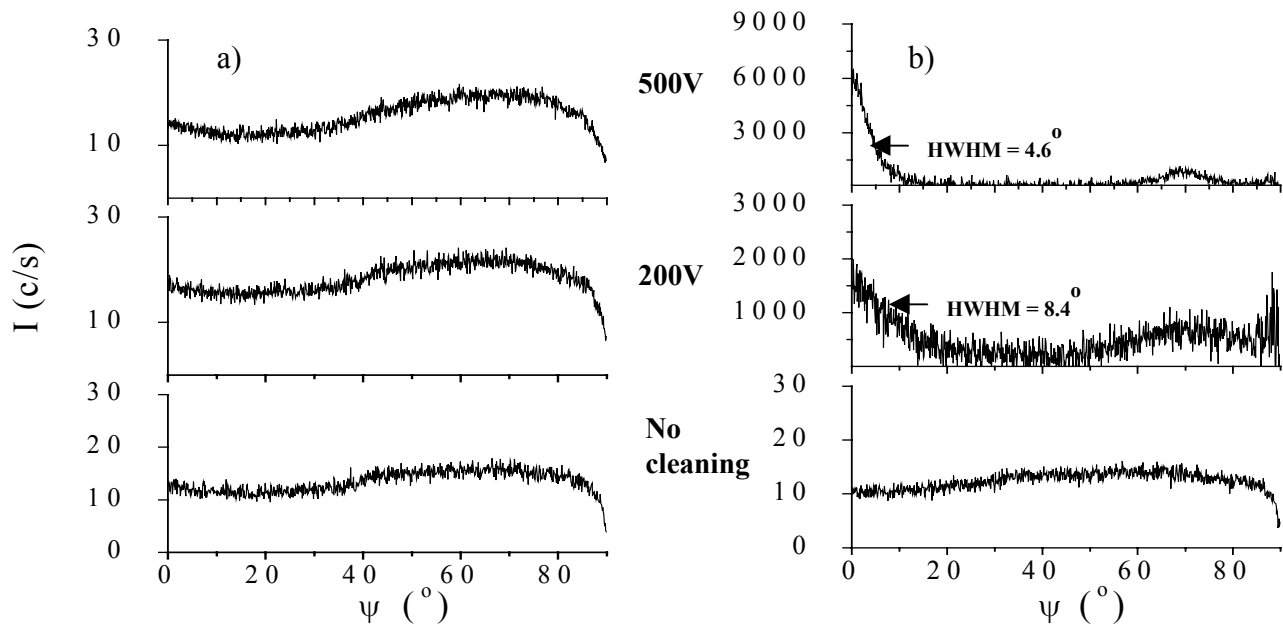


Figure 1.14. 111 pole figure sections for 5 nm thick Cu films on SiO_2 (a) and Si_3N_4 (b) substrates. Note that the curves for the films on SiO_2 and that on uncleaned Si_3N_4 substrates were not corrected for background and absorption.

A comparison of Figs. 1.13 and 1.14 shows a similarity in the texture character of the films, i.e. stronger texture on the Si_3N_4 substrate that increases upon sputter cleaning. Hence, the texture character of the films is determined by the substrate type at the very on-set of the film development.

Yet, there are also differences between the ultrathin films and the thick films. For the thick films grown on Si_3N_4 substrates the half widths at half maximum (HWHM) of the 111 pole at $\psi = 0^\circ$ are 5.3° , 3.1° and 1.5° at no substrate cleaning and substrate cleaning at 200 V and 500 V, respectively (Fig. 1.13). For the ultrathin films (Fig. 1.14) distinctly larger values occur for the HWHM: 8.4° (at 200 V) and 4.6° (at 500 V). This indicates that the texture sharpness of the films increases with thickening of the very thin films (later on there no further substantial change, see section 3.2.2.2). The intensity ratio $I_{\text{Si}_3\text{N}_4}(\psi = 0^\circ) : I_{\text{SiO}_2}(\psi = 0^\circ)$ for the thick films deposited on the two substrates cleaned at 500 V is approximately 10 (see Fig. 1.15). If this were to hold for the ultra thin film, then an intensity $I_{\text{SiO}_2}(\psi = 0^\circ)$ of about 600 c/s would be expected. However, only the background level of about 15 c/s (see Fig. 1.14) was measured in this case. These observations show that the difference in the texture strength of the films deposited on the two substrates is more pronounced for the 5 nm thick films than for the 500 nm thick films. Thus the influence of the substrate on the film texture decreases during growth of the Cu films.

Texture of films versus substrate surface roughness and impurities

Surface roughness has been reported to decrease the texture strength of thin films [11]. However, the present study does not reveal an obvious correlation between the texture of Cu films and the roughness (Fig. 1.1) of the substrate surface.

The decrease of oxygen contaminant on the Si_3N_4 surface (Fig. 1.2) correlates with an increase of the {111} texture of the Cu films (see Figs. 1.15 and 1.16). Thus oxygen on the substrate seems to hinder the development of a sharp {111} texture in the film. This may be understood as follows. The atomic densities of amorphous SiO_2 and Si_3N_4 are 0.066 \AA^{-3} and 0.104 \AA^{-3} respectively. It has been suggested for Cu films on different amorphous substrates having different densities that a higher atomic density of the substrate is a possible factor for a stronger texture [5]. Thus the relatively strong texture in the films deposited on Si_3N_4 substrates is attributed to the higher atomic density of the Si_3N_4 surfaces (the oxygen contaminant on the *uncleaned* Si_3N_4 substrates then is assumed to form a thin SiO_2 layer on top of the substrate).

An alternative explanation for the role of the oxygen contaminant departs from the assumption that the interaction between Cu and O (of the SiO_2 substrate) is stronger than that between Cu and N (of the Si_3N_4 substrate), this being true for gaseous O_2 and N_2 . The Cu atoms tend to build a highly ordered structure with a {111} texture on top of a disordered substrate structure. In case of epitaxial growth, the substrate would dictate the structure of the growing film, i.e. would impose a disordered structure on the Cu film. This effect is to be expected stronger as the

chemical interaction between Cu and the substrate atoms becomes stronger. The compromise between a perfect $\{111\}$ texture (for surface energy reasons) and the influence of the amorphous substrate then are local deviations from a perfect alignment of the $\langle 111 \rangle$ direction of the Cu crystallites perpendicular to the substrate surface. Further layers of Cu after the early stage of film growth can form on more perfectly oriented crystallites because they grow not on a disordered underlayer but on an already ordered Cu underlayer. This would explain the sharper texture in the thicker films.

3.3 Morphology

3.3.1 Deposition gas pressure effect, 500 nm films

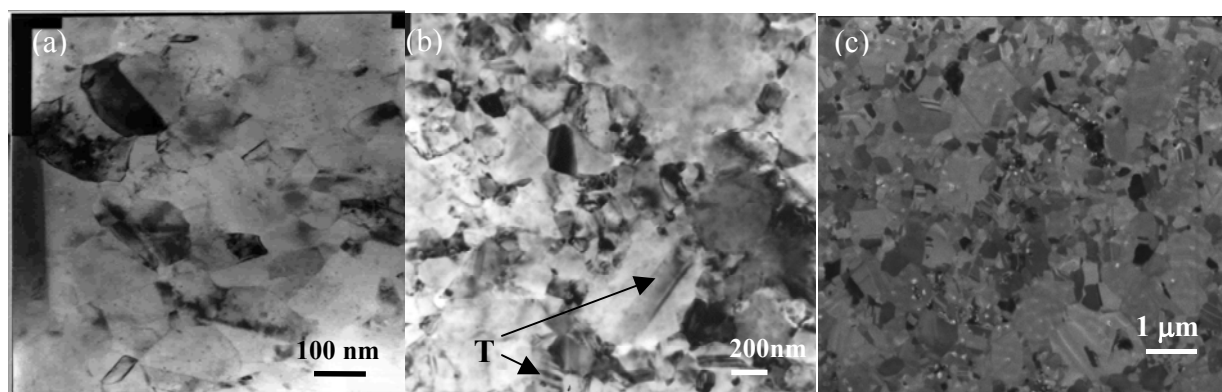


Figure 1.15. Bright-field image TEM plane views of as-deposited Cu films (series B1) on SiO_2 substrates at (a) 5×10^{-2} Pa, (b) 22×10^{-2} Pa and (c) 69×10^{-2} Pa. Note the different scales. Twins (T) are indicated in Fig. 1.15b.

The in-plane microstructure observed by TEM of the 500 nm thick Cu films deposited at various gas pressures on SiO_2 and Si_3N_4 substrates is shown in Figs. 1.15 and 1.16. The morphology of the grains for the films deposited on SiO_2 substrates was found to be equiaxed structured. Twins were observed in some of the grains (see e.g. T in Fig. 1.15b). The grain morphology of the films deposited on Si_3N_4 substrates was likewise equiaxed. The presence of twins also was observed in the micrographs (see T in Fig. 1.16a,c). The images show that more twins are present in the Cu films on Si_3N_4 substrates than in the films on SiO_2 (compare e.g. Fig. 1.15a with Fig. 1.16a). The in-plane grain sizes were determined by the linear intersection method calculating the mean linear intercept. The thus determined in-plane grain size of around 150 nm is of the order of one-third of the film thickness.

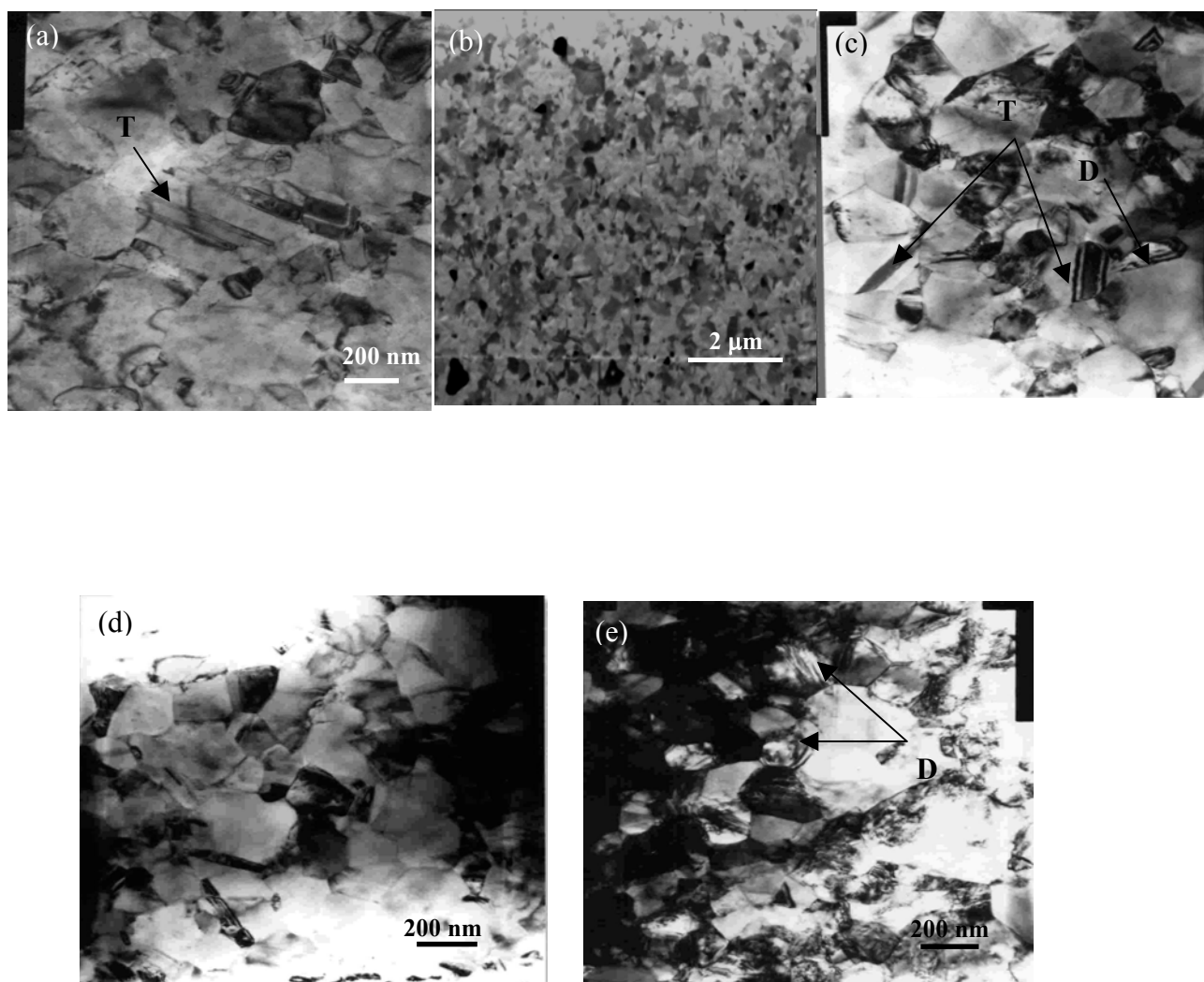


Figure 1.16. Bright-field image TEM plane views of Cu films (series B2) deposited on Si_3N_4 substrates at (a) 5×10^{-2} Pa, (b) 10×10^{-2} Pa, (c) 22×10^{-2} Pa, (d) 46×10^{-2} Pa and (e) 69×10^{-2} Pa. Note the different scales. Twins (T) and dislocation lines (D) are indicated in Fig. 1.16 a,c.

The in-plane grain size as a function of deposition gas pressure for the Cu films grown on SiO_2 and Si_3N_4 substrates is shown in Fig. 1.17. An increase in the average grain size of the Cu films deposited on SiO_2 was observed with increase in the deposition gas pressure, whereas in the case of the Cu films on Si_3N_4 substrates, a slight decrease in size was observed with increase in deposition gas pressure.

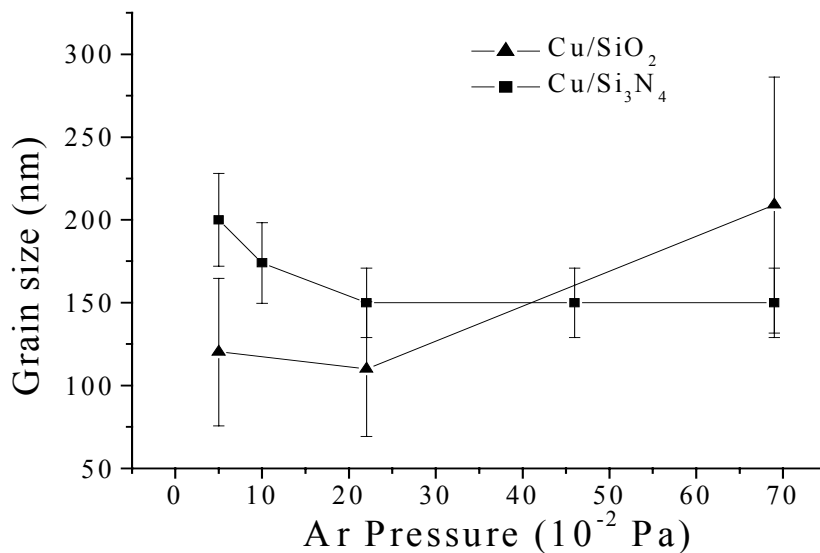


Figure 1.17. In-plane grain size versus film deposition gas pressure for Cu films deposited on SiO₂ (series B1) and Si₃N₄ (series B2) substrates.

3.3.2 Annealing effect

The microstructural image of sample B1O2d (film annealed at 450 °C) is shown in Fig. 1.18. Dislocation lines (D in Fig. 1.18) and twins (T in Fig. 1.18) were observed on the grains. A comparison with the microstructure of the unannealed sample B1O2 shows that grain growth occurred during the annealing of the film. The average in-plane grain size for the unannealed film was about 110 nm whereas that in the annealed film was about 700 nm. Annealing was also observed to broaden the twin bands (T in Fig. 1.18).

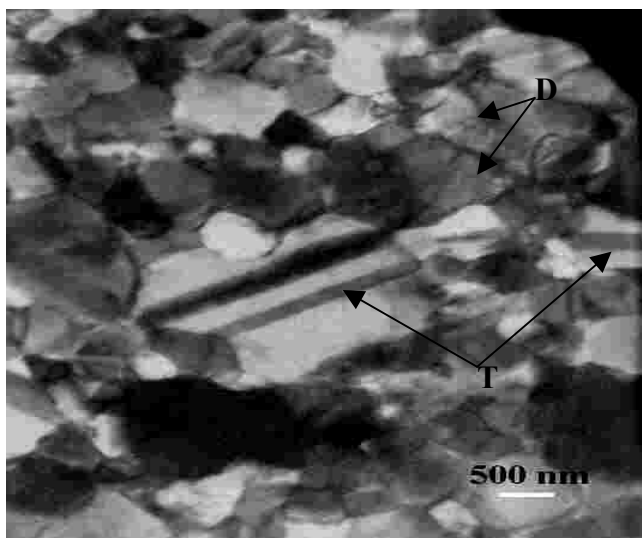


Figure 1.18. Microstructure of a post-deposition annealed (450 °C) 500 nm thick Cu film on SiO₂ substrate. A large grain with twin bands can be seen in the center of the bright-field TEM image. Twins (T) and dislocation lines (D) are indicated.

3.3.3 Substrate cleaning effect, 500 nm films

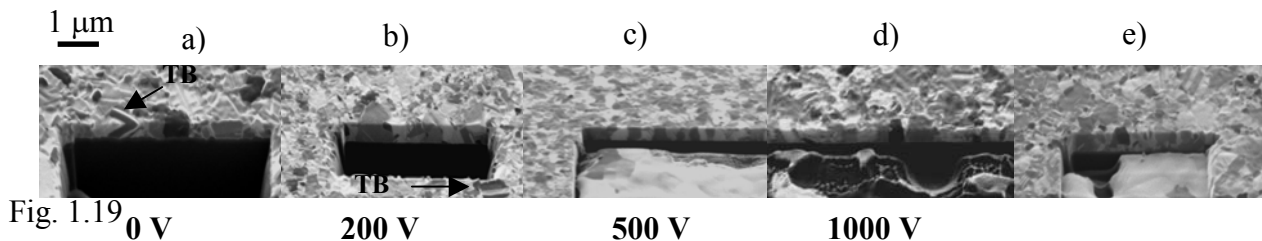


Fig. 1.19

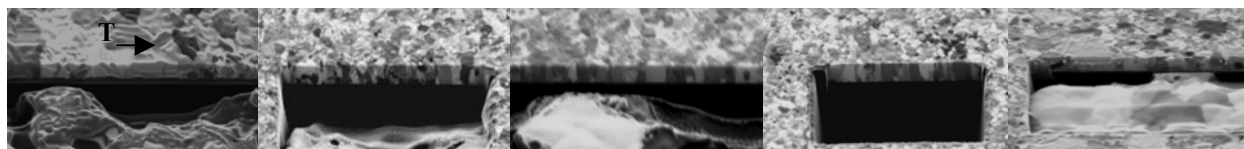


Fig. 1.20

Figures 1.19 & 1.20. FIB images of Cu films (series B4) deposited on SiO_2 and Si_3N_4 substrates at (a) no substrate cleaning, (b-d) substrate cleaning at 200, 500 and 1000 V respectively, and (e) substrate cleaning at 200 V for a low deposition gas pressure. T and TB indicate twins and twin-bands respectively.

The microstructures, as observed by FIB imaging, of the Cu films deposited on as-received and sputter cleaned substrates (series B4 in Table 1.1) are shown in Figs. 1.19 and 1.20. Evidence of twinning was present in the images (Figs. 1.19a and 1.20a). These twins are more likely to be growth twins since no annealing was performed on this series of specimens. Twin bands, measuring about 100 nm in width, which extended through the film thickness, were found in the images. The films deposited on substrates that were cleaned at 200 V had morphologies that were generally the same (irregular or equiaxed) as those on uncleaned substrates but with a grain size reduced to one-third. In the films deposited on Si_3N_4 substrates columnar grains were also observed, making up about 30 % of the observed grains. The grains of the films on substrates sputter cleaned at 500 and 1000 V were found in both film systems to be clearly columnar with sizes comparable with those on substrates cleaned at 200 V. Although no twins were detected in the present microstructural images of the films shown in Fig. 1.19c,d and Fig. 1.20c,d, pole figure analysis of these films indicate their existence (Fig. 1.13).

The average in-plane grain sizes for the films, as function of substrate cleaning condition, is shown in Fig. 1.21. From the plot it is obvious that the sizes of the grains in the two film systems are equal for the various substrate and deposition conditions.

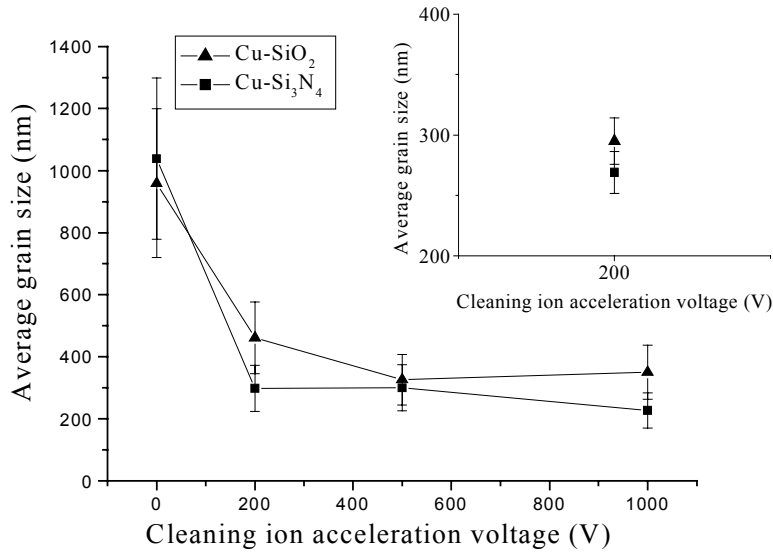


Figure 1.21. Grain size versus substrate cleaning voltage for Cu films (series B4) deposited on SiO₂ and Si₃N₄ substrates. Insert shows grain sizes for films deposited on substrates cleaned at 200 V and low-pressure conditions.

It is noted that the more perfect columnar structure of the Cu films on the substrates cleaned at 500 V and 1000 V, compared to that for cleaning at 200 V, is associated with a higher roughness of the substrate surface (Fig. 1.1) and with less contaminants at the surface (Fig. 1.2). The mechanism responsible for microstructure development in the films on uncleaned substrates may depend on the presence of O and C impurities on the substrate surface, which may hinder the development of a columnar structure of the Cu films.

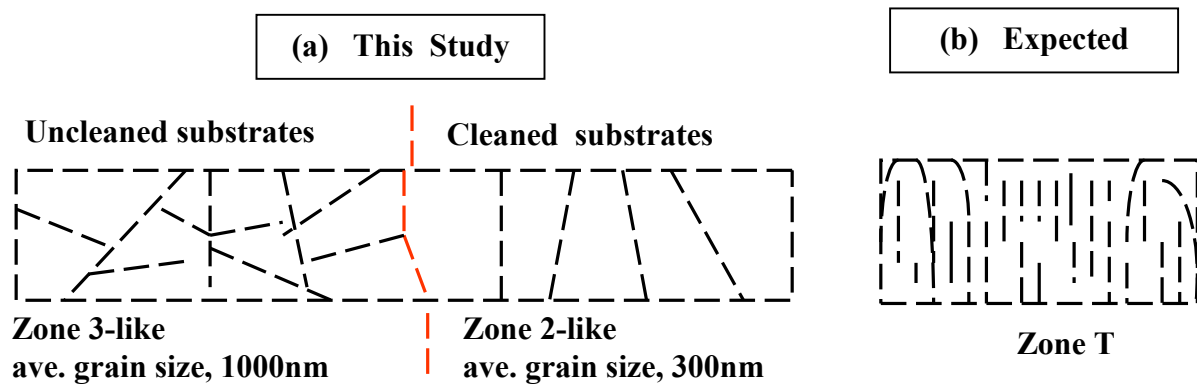


Figure 1.22. Schematic diagram showing (a) the microstructure of 500 nm thick Cu films produced at constant deposition conditions but modified substrate surface and (b) the expected fibrous structure based on SZM developed from much thicker films.

According to the structure zone model as presented in [13], the Cu films produced under the conditions used in this study are expected to exhibit a zone T-like structure characterised by a dense array of fibrous grains and conventional grain boundaries (Fig. 1.22b). Clearly this is not the case. The microstructure of the films deposited on uncleaned substrates was found to consist of a mixture of irregular and equiaxed shapes with grain sizes ranging from 700 – 1400 nm (Fig. 1.22a), i.e. a zone 3-like morphology was observed, which is characterised by recrystallisation and bulk diffusion [33]. The transition to a columnar microstructure upon sputter cleaning of the substrates (Fig. 1.22a) seems as though there was a shift on the axis of the homologous temperature T/T_m towards lower values, where the zone 3 structures evolves to the zone 2 type.

The present study reveals that it is possible to obtain at constant temperature, pressure and deposition rate microstructures of varying morphology for thin films deposited on substrates of variable surface conditions (roughness and impurities). The existing structure zone model clearly does not account for the influence of substrate surface conditions.

3.3.4 Substrate cleaning effect, ultrathin films

AFM topography images for the 5 nm thick films on uncleaned and sputter cleaned Si_3N_4 substrates are shown in Fig. 1.23.

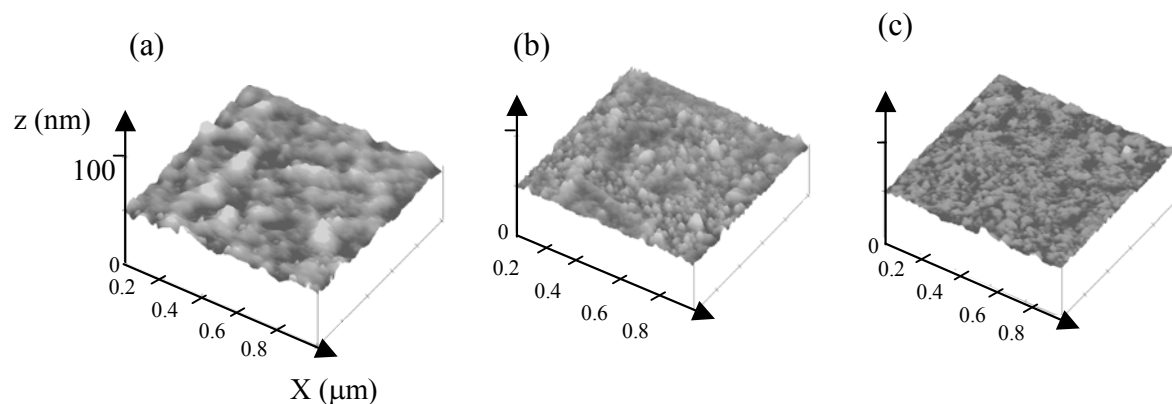


Figure 1.23. Three dimensional AFM topography images of 5 nm thick Cu layers deposited on Si_3N_4 substrates in the case of (a) no substrate cleaning, and in the case of substrate cleaning at (b) 200 V and (c) 500 V. The same z-scale applies to all the images.

The structures observed in the AFM images are islands, (black portions in the image represent uncovered substrate areas while the grey areas are the Cu deposits). Hence for these ultrathin films coalescence stage of film growth is in progress. The island size as determined from the lateral extensions of the height fluctuations in the images is shown in Fig. 1.24 versus substrate sputter cleaning voltage. Island size was observed to decrease upon sputter cleaning. This implies a higher nuclei/island density in the ultrathin films if substrate cleaning prior to film deposition is applied.

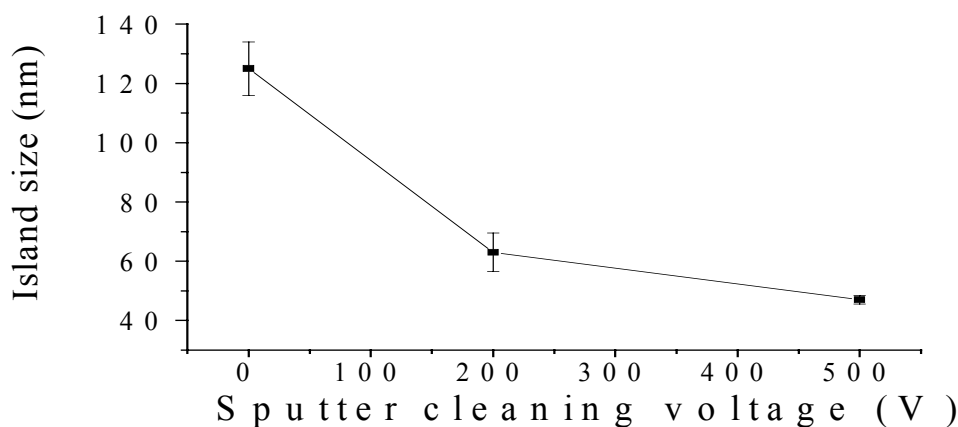


Figure 1.24. Graph of island size in 5 nm thick Cu films on Si_3N_4 substrates as a function of substrate cleaning voltage.

3.4 Residual stress

The X-ray diffraction stress measurements were conducted using the 111 reflection for the ultrathin (5 nm) films and the 311 reflection for the thicker films. Due to the strong {111} texture of the thicker films, the pole figure $I(\psi)$ for the 311 reflection exhibits maxima at three tilt angles ψ , as shown in Fig. 1.25, which have been used for the stress measurements.

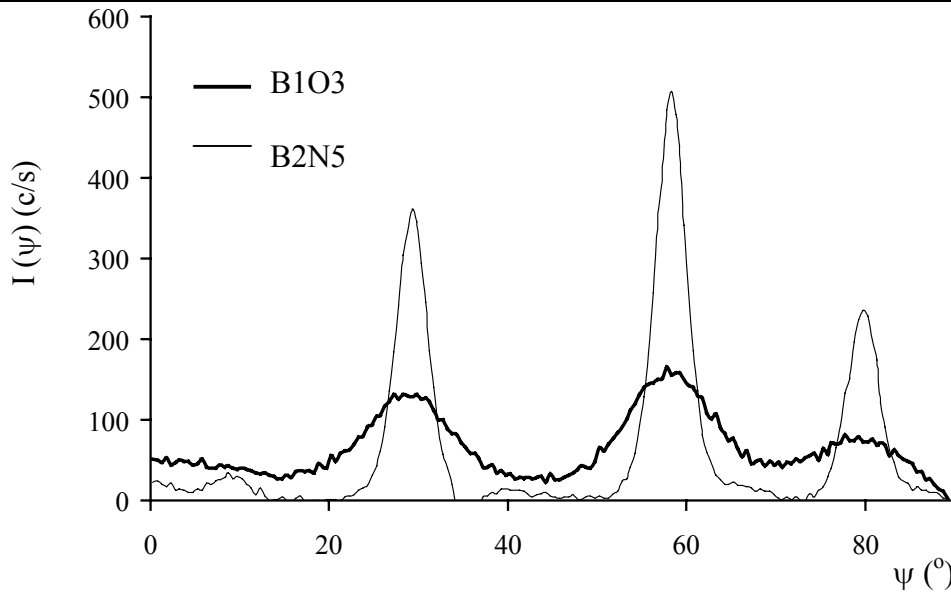


Figure 1.25. Pole figure scans for 500 nm thick Cu films (series B1 and B2) on SiO_2 and Si_3N_4 substrates for the 311 reflection.

From the 2θ scans, recorded at various tilt angles ψ , the lattice plane spacing, d_ψ , is determined from the peak position using Bragg's law. If a plane rotationally symmetric stress state exists (i.e. no ϕ dependency in stress), the in-plane residual stress, $\sigma_{//,r}$, can be determined from [34]

$$\varepsilon_\psi^{hkl} = \frac{d_\psi^{hkl} - d_0^{hkl}}{d_0^{hkl}} = \left[2S_1^{hkl} + 1/2 S_2^{hkl} \sin^2 \psi \right] \sigma_{//,r} \quad (1.6)$$

where d_0 , is the stress free lattice constant and S_1^{hkl} and $1/2 S_2^{hkl}$ are the X-ray elastic constants for the film. In the present study the Neerfeld-Hill values for $1/2 S_2^{hkl}$ were taken, 11.74 TPa^{-1} for 311 Cu and 7.87 TPa^{-1} for 111 Cu, calculated from the single crystal elastic constants from [35].

The stress parallel to the surface, $\sigma_{//,r}$, was calculated from the slope of the d_ψ^{hkl} versus $\sin^2 \psi$ plot.

The residual stress represents the sum of the intrinsic (growth induced stress $\sigma_{//,g}$) and extrinsic (thermal stress, $\sigma_{//,th}$ generated by differences in the film and substrate thermal expansion coefficients) stress, and is given by:

$$\sigma_{//,r} = \sigma_{//,g} + \sigma_{//,th} \quad (1.7)$$

Provided that no stress relaxation by plastic deformation takes place, the thermally induced stress can be determined from:

$$\sigma_{//,th} = \frac{E}{1-\nu} (\alpha_f - \alpha_s) (T_d - T_a) \quad (1.8)$$

$E/(1-\nu)$, is the biaxial modulus that depends on the texture state. The Neerfeld-Hill average for the biaxial modulus has been adopted for this study and has been calculated as 263 GPa in the case of a

(perfect) Cu {111} fibre texture and as 192 GPa for the random case. α_f and α_s are the coefficients of thermal linear expansion for the film ($16.5 \times 10^{-6}/\text{K}$ for Cu [36]) and substrate ($1.72 \times 10^{-6}/\text{K}$ for Si, extrapolated for $T = 373 \text{ K}$ [37]) respectively. T_d (100 °C) and T_a (25 °C) denote the substrate temperature during deposition and the ambient temperature during the stress measurement, respectively. The tensile thermal stress was calculated to be 290 MPa for the textured case and 213 MPa for the random case.

3.4.1 Deposition gas pressure effect, 500 nm films

$\sin^2\psi$ plots for the 500 nm thick Cu films on SiO_2 substrates are shown in Fig. 1.26a for different deposition gas pressures (series B1O) and for an annealed sample. Clearly, the residual stresses are tensile. Table 1.3 lists the calculated stress values. The measured stresses are distinctly larger than the yield stress of bulk Cu ($\sigma_{\text{yield}} = 33.3 \text{ MPa}$ [38]), signifying that thin Cu films are mechanically more stable than bulk Cu [39].

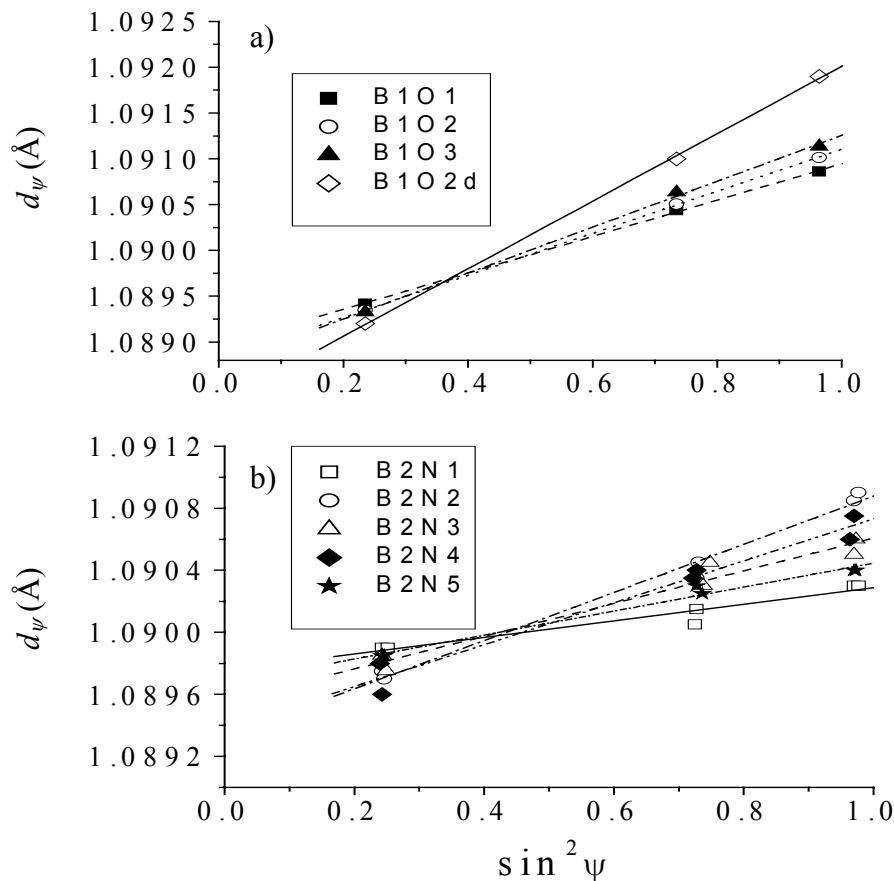


Figure 1.26. Plot of d_ψ (311) versus $\sin^2\psi$ for 500 nm thick Cu films deposited at various deposition argon pressures on (a) SiO_2 substrates ($P_{\text{B1O1}} < P_{\text{B1O2}} < P_{\text{B1O3}}$) and for B1O2 annealed at 450 °C (B1O2d) and on (b) Si_3N_4 substrates ($P_{\text{B2N1}} < P_{\text{B2N2}} < P_{\text{B2N3}} < P_{\text{B2N4}} < P_{\text{B2N5}}$). Straight lines are fitted to the measured data.

Subtracting the thermal stress, $\sigma_{//,th}$, from the measured residual stress, $\sigma_{//,r}$, reveals that the growth stress, $\sigma_{//,g}$, for the layers is compressive (Table 1.3). The compressive nature of the growth stress can be ascribed to the atomic peening effect during sputter deposition. The decrease of the compressive growth stress with increasing Ar pressure is due to the correspondingly lower kinetic energy of the Cu ions: a less pronounced peening effect occurs at higher Ar pressure. However, regarding the results for other series of Cu films (see below) the trend observed here might be accidental.

Annealing at 450 °C appreciably increases the tensile stress in the Cu film. This indicates that the compressive growth stress is healed out during annealing and the residual stress, $\sigma_{//,r} = 288$ MPa, is equal to the thermal stress corresponding to some temperature between 25 °C and 450 °C below which during the cooling process $\sigma_{//,th}$ cannot relax further.

Table 1.3. Residual stress $\sigma_{//,r}$ and growth stress $\sigma_{//,g}$ for Cu films deposited on SiO₂ at various gas (Ar) pressures (series B1O) and for an annealed specimen (B1O2d).

Specimen	B1O1	B1O2	B1O3	B1O2d
$\sigma_{//,r}$ (MPa)	156 ± 4	180 ± 2	196 ± 8	288 ± 6
$\sigma_{//,g}$ (MPa)	-134	-110	-94	-

$\sin^2\psi$ plots for 500 nm thick Cu films on Si₃N₄ substrates are shown Fig. 1.26b for different deposition (Ar) gas pressures (series B2N). The observed tensile residual and compressive growth (after correction for the thermal stress) stresses are listed in Table 1.4.

With this series no systematic relationship was observed between the stress and the variation in deposition gas pressure. The values of the compressive growth stress, $\sigma_{//,g}$, in the films on Si₃N₄ are larger by about 100 MPa than in the films on SiO₂ (Table 1.3).

Table 1.4. Residual stress $\sigma_{//,r}$ and growth stress $\sigma_{//,g}$ Cu films deposited on Si₃N₄ substrates at various gas (Ar) pressures (series B2N).

Specimen	B2N1	B2N2	B2N3	B2N4	B2N5
$\sigma_{//,r}$ (MPa)	41 ± 6	121 ± 7	82 ± 8	106 ± 10	61 ± 5
$\sigma_{//,g}$ (MPa)	-249	-169	-208	-184	-229

The stress results for Cu films of two different thicknesses, 500 nm and 1 μm , deposited on SiO_2 and Si_3N_4 substrates are listed in Table 1.5. The observed tensile residual stresses in the films and the compressive growth stresses are independent of the thickness or substrate type (the differences with variation of the varied parameters are not systematic).

Table 1.5. Residual stress $\sigma_{//,r}$ and growth stress $\sigma_{//,th}$ for 500 nm and 1 μm thick Cu films deposited on SiO_2 and Si_3N_4 substrates at various gas (Ar) pressures (series B3).

Specimen	B3O1	B3N1	B3O2	B3N2	B3O3	B3N3
$\sigma_{//,r}$ (MPa)	53 ± 8	85 ± 4	95 ± 2	98 ± 3	72 ± 2	75 ± 3
$\sigma_{//,g}$ (MPa)	-237	-205	-195	-192	-218	-215

3.4.2 Substrate cleaning effect, ultrathin films

Normally, ultrathin films yield too little diffracted intensity to make diffraction stress analysis feasible. However, due to the strong $\{111\}$ texture of the ultrathin Cu films on Si_3N_4 substrates (if the substrates had been cleaned) it became possible to perform a stress measurement, yet, over ψ ranges of $0^\circ - 18^\circ$ and $58^\circ - 76^\circ$ (see Fig. 1.14b).

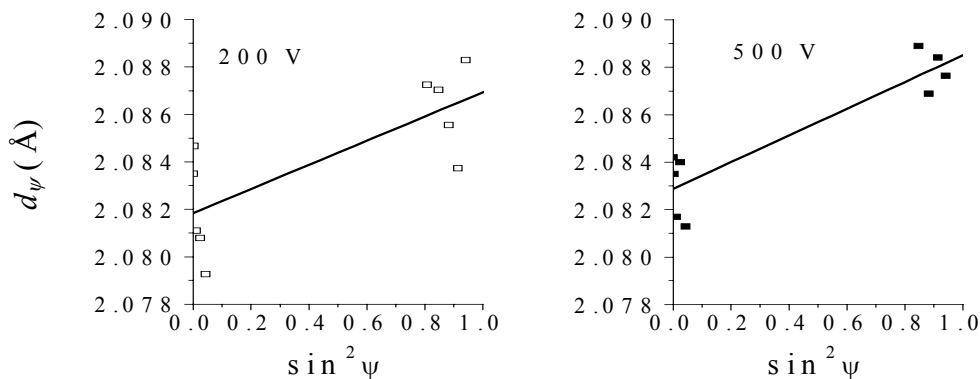


Figure 1.27. $\sin^2 \psi$ plots, from 111 peaks, for ultra thin (5 nm) Cu films deposited on Si_3N_4 substrates sputter cleaned at : (a) 200 V and (b) 500 V.

The $\sin^2 \psi$ plots generated from the 111 peaks of the ultrathin Cu films revealed the presence of residual stresses of tensile nature in these films (Fig. 1.27). Due to the (still) low count rate from the 5 nm thick films, a large scatter of the lattice strain data points resulted and this leads to the large error range indicated for the $\sigma_{//,r}$ values. The calculated values for the residual stress in the

ultrathin films were 310 ± 90 at 200 V and 342 ± 58 at 500 V. These values evidently are larger than the thermal stress (290 MPa) for the a perfect $\{111\}$ fibre texture and 213 MPa for the random case. This indicates that the growth stress ($\sigma_{//,g} = \sigma_{//,r} - \sigma_{//,t}$) in the ultrathin films is of tensile nature. Such tensile stresses would develop upon island coalescence, as a result of the interatomic attractive forces that act across the island boundaries [6]. Although the error for the stress values in the ultrathin films is rather large, it appears that the stress is higher for the case of sputter cleaning at 500 V than at 200 V. This trend can be explained by the smaller island sizes for the film deposited on substrates cleaned at 500 V and hence the higher grain boundary density, as compared to the case of substrate cleaning at 200 V.

3.4.3 Substrate cleaning effect, 500 nm films

Diffraction stress analysis was carried-out for the 500 nm thick Cu films (series B4O and B4N), following different substrate sputter cleaning conditions. Examples for the $\sin^2\psi$ plots are shown in Fig. 1.28.

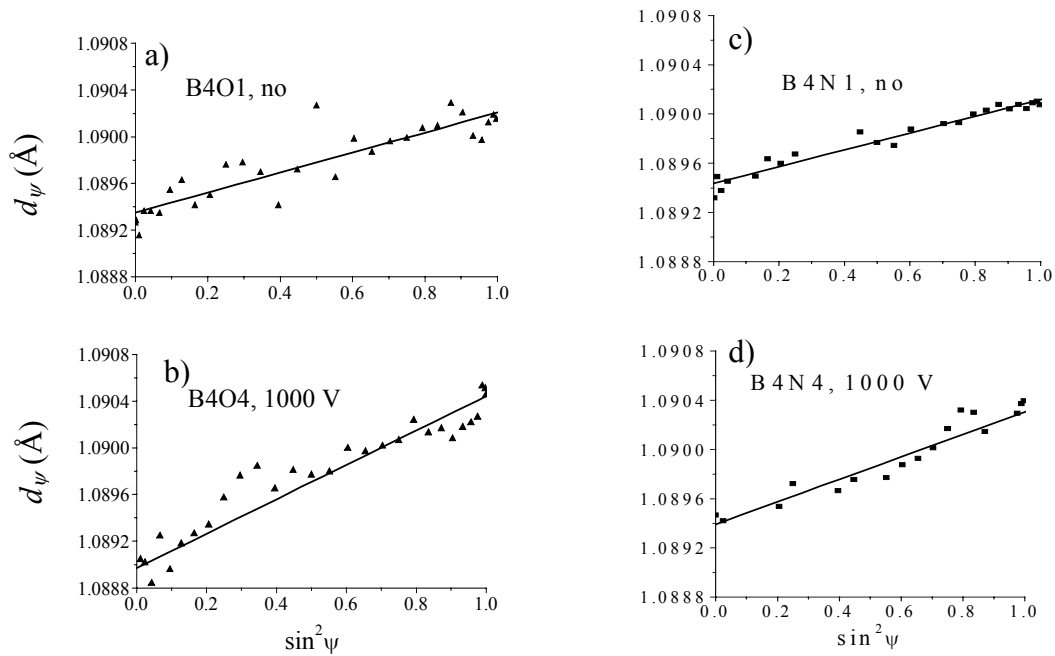


Figure 1.28. Plot of d_{ψ} 311 versus $\sin^2\psi$ for 500 nm thick Cu films deposited on uncleaned substrates and substrates sputter cleaned at 1000 V for (a, b) SiO_2 substrates and (c, d) Si_3N_4 substrates.

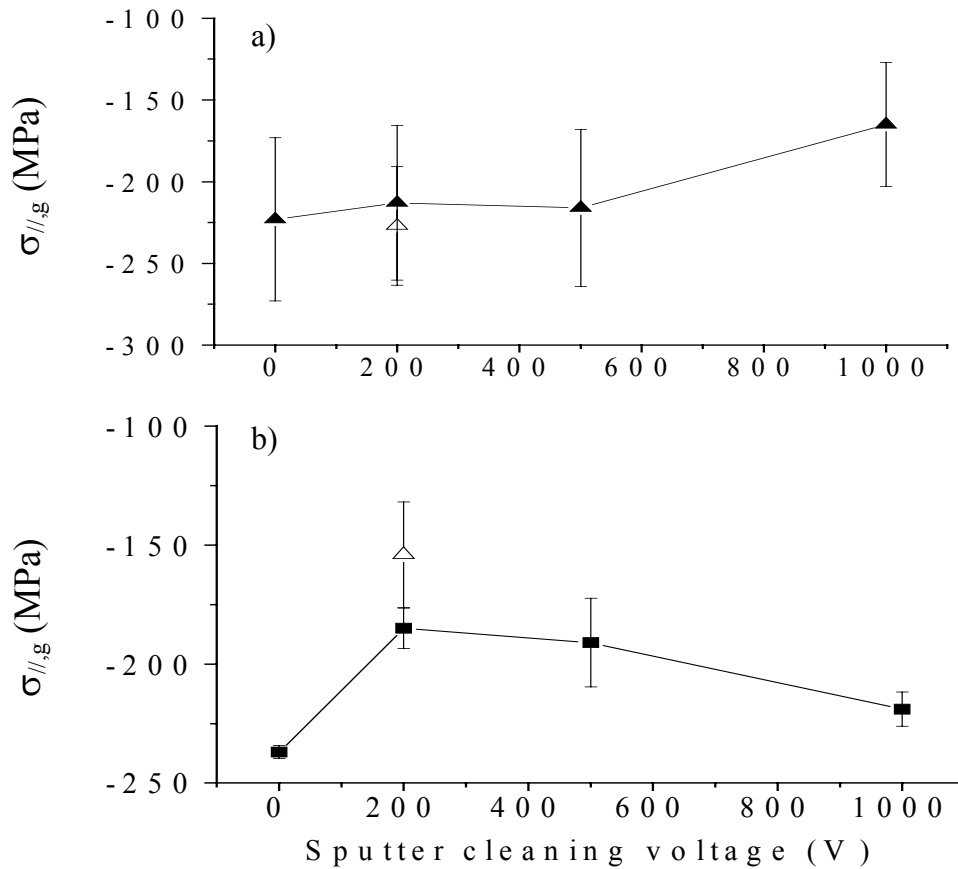


Figure 1.29. Graph of $\sigma_{//,g}$ against substrate sputter cleaning acceleration voltage for 500 nm thick Cu films deposited on (a) SiO₂ substrates (series B4O) and (b) Si₃N₄ substrates (series B4N). Δ : B4O5 and B4N5 at low deposition gas pressure. (The lines are drawn as guide for the eye)

The residual stress, $\sigma_{//,r}$ as deduced from the slope of the $\sin^2\psi$ plots was found to be tensile in all the Cu films. The compressive growth stress $\sigma_{//,g}$ (calculated from $\sigma_{//,r}$ by subtraction of $\sigma_{//,th}$) is shown in Fig. 1.29 versus the substrate sputter cleaning voltage. For films on SiO₂ substrates $\sigma_{//,g}$ decreases upon sputter cleaning, in particular for 1000 V. The difference of $\sigma_{//,g}$ for the films deposited after substrate cleaning at 200 V at higher (B4O2) and lower (B4O5) gas pressures is not significant (see for error bars in Fig. 1.29a).

Also for the films on Si₃N₄ substrates, the compressive growth stress $\sigma_{//,g}$, is smaller for the films deposited on cleaned substrates than on the uncleaned substrate. In contrast to the films grown on cleaned SiO₂ substrates, the growth stress increases with increasing cleaning voltage and it is smaller at a lower Ar gas pressure (see 200 V in Fig. 1.29b).

A comparison of the growth stress in the 500 nm and 5 nm thick Cu films deposited on Si₃N₄ substrates indicates contrasting stress states, where for the thicker films $\sigma_{//,g}$ is compressive

and for the ultrathin films $\sigma_{//,g}$ is tensile. Two jointly operating mechanisms can be responsible for this reversal of the stress during the growth of the (eventually 500 nm thick) films: (i) relief of the tensile coalescence stress upon continued film growth, for materials of high atomic mobility such as Cu [40, 41], (ii) generation of compressive stress, where different mechanisms are reported to account for this:

Incorporation of excess atoms into grain boundaries by atomic peening [9, 42] or driven by the excess (with respect to the grain boundaries) chemical potential of the film surface during growth [43], incorporation of excess atoms at adjacent compressive ledges at the surface of the growing film [44].

The compressive stress $\sigma_{//,g}$ decreases from 237 MPa to 185 MPa for 500 nm thick Cu films on Si_3N_4 substrates with the introduction of substrate sputter cleaning at 200 V (Fig. 1.29). The emergence of a columnar microstructure upon sputter cleaning may be responsible for this stress decrease, recognizing that intracolumnar voids are thought to generate tensile stress by the action of the interatomic forces acting across the voids [9]. Further increase of the sputter cleaning voltage leads to an increase of the compressive stress. This may be associated with the higher roughness of the substrates cleaned at 500 V and 1000 V than that at 200 V (see Fig. 1.1). The higher substrate roughness may cause higher roughness of the Cu films and thus more ledges at the film surface and consequently (according to [44]) higher compressive stress.

3.5 Microstrain

Microstrain in the 500 nm thick Cu films perpendicular to the film surface was determined from the integral widths of the diffraction peaks measured by $\theta/2\theta$ scans in Bragg-Brentano geometry (section 2.2). The Williamson - Hall (integral breadth) method [45] was applied to the 111 and 222 reflections after a Pseudo-Voigt function was fitted to the measured peaks.

The peak width due to physical broadening, β_f , was obtained by correcting the measured peak width, β_h , for the instrumental broadening, β_g , determined from an annealed Cu powder according to [46]:

$$\beta_f = \sqrt{\beta_h^2 - \beta_g^2} \quad (1.9)$$

The Williamson - Hall plot revealed that no peak broadening due to the crystallite size effect occurred for the Cu films. This implies that the grain size in the films is larger than the upper detection limit (of the order of 100 nm) accessible by X-ray diffraction line-profile analysis. This

finding is in accordance with the microscopic results obtained for the thin Cu films (section 3.3). Microstrain in the Cu films is, therefore, solely responsible for line broadening.

The values for the microstrain ϵ are shown in Fig. 1.30 versus the Ar pressure and in Fig. 1.31 versus the sputter cleaning voltage for Cu films deposited on amorphous SiO_2 and Si_3N_4 substrates.

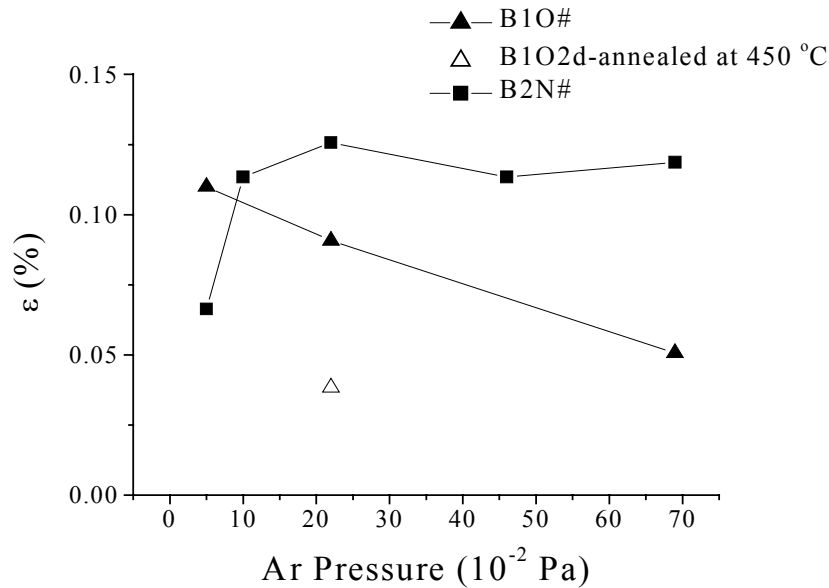


Figure 1.30. Microstrain, ϵ , as a function of deposition gas pressure for Cu films (B1O and B2N) deposited on SiO_2 and Si_3N_4 substrates.

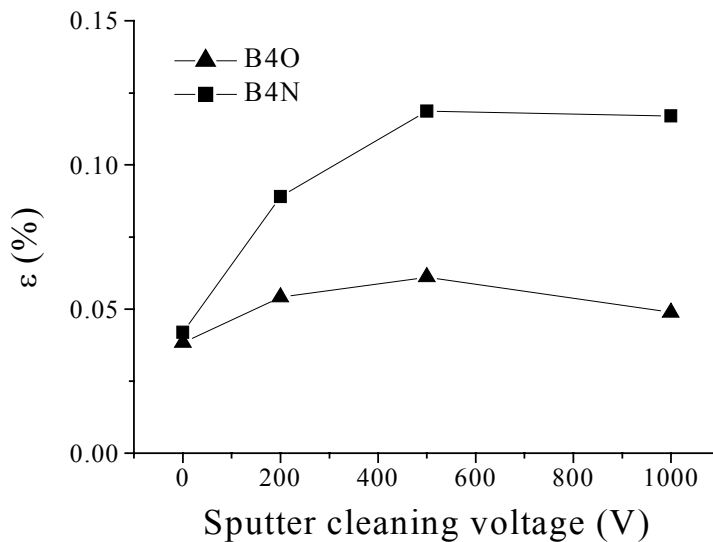


Figure 1.31. Microstrain, ϵ , as a function of sputter cleaning voltage for Cu films (series B4O and B4N) deposited on SiO_2 and Si_3N_4 substrates.

The microstrain in the films is generally larger for the films deposited on Si_3N_4 substrates than for those on SiO_2 substrates. For some series of Cu films a correlation between the microstrain and the growth stress was found. Comparing the ε values in Fig. 1.30 and the $\sigma_{//g}$ values in Tables 1.3 and 1.4 it can be stated that both ε and $\sigma_{//g}$ is larger for films on Si_3N_4 . With increase in deposition Ar gas pressure, ε decreased for the films deposited on SiO_2 substrates. This is in agreement with the values calculated for $\sigma_{//g}$ where a decrease was also observed. The Cu film deposited on Si_3N_4 substrates likewise showed an agreement where in both cases (ε and $\sigma_{//g}$), no systematic dependence is observed. Annealing resulted in an appreciable decrease in ε (see the included data point in Fig. 1.30), indicative of the healing out of microstress in the Cu films in which also the growth stress had relaxed. However, other film series did not exhibit such a clear correlation (see e.g. Figs. 1.29 and 1.31).

It is noteworthy to mention that the microstrain results also correlate with the texture results obtained for the Cu films. Especially for the films deposited on Si_3N_4 , an increase in the microstrain along the 111 direction perpendicular to the film surface (Fig. 1.31) corresponds to an increase in the $\{111\}$ texture strength upon substrate sputter cleaning (Fig. 1.13). This effect is much less pronounced for the Cu films on SiO_2 substrates.

4. Conclusions

4.1 Texture

- For a deeper insight into the texture of thin films $\theta/2\theta$ scans as well as pole figure scans are important, both having specific advantages and limitations.
- The substrate type and substrate surface condition have marked influences on the texture of as-deposited Cu films.
- Cu films deposited on uncleaned substrates exhibit $\{111\}$ texture, having the same character irrespective of the substrate type.
- Sputter cleaning of substrates prior to film deposition, by which surface impurities are removed, has no influence on the $\{111\}$ texture Cu films deposited on SiO_2 substrates whereas for Cu films deposited on Si_3N_4 substrates a marked increase of the texture sharpness occurs with increasing substrate sputter cleaning voltage.
- The $\{111\}$ texture trend in ultrathin (5 nm) Cu films as a function of substrate type and cleaning conditions is the same as in thicker (500 nm) Cu films.

- Growth twins generate a $\{511\}$ texture component in Cu films that is sharper for films on Si_3N_4 substrates.
- The volume fraction of twins for films on SiO_2 substrates is higher than for films deposited on Si_3N_4 substrates.
- The sharper texture of films deposited on cleaned Si_3N_4 substrates probably is due to the absence of oxygen.

4.2 Morphology

- Sputter cleaning influences the Morphology of Cu thin films:
For the ultrathin films, undergoing coalescence, it leads to the decrease of island size by a factor of 2.
For 500 nm thick films, it leads to a morphology transition from a mixture of globular and equiaxial microstructure to columnar microstructures with smaller grain sizes.

4.3 Growth stress and microstrain

- The growth stress of ultrathin Cu films is tensile and originates from the attractive forces between islands at the coalescence stage of film growth. For films on cleaned substrates it is higher due to smaller island sizes.
- With thicker films (500 nm) the growth stress is compressive. This reversal from tensile to compressive growth stress during film thickening is due to relief of the coalescence stress and the atomic peening during sputter deposition.
- Cu films with sharper texture exhibit higher microstrain.
- Annealing leads to the sharpening of the $\{111\}$ fibre texture, an increase of the average grain size, a relaxation of the growth stress and a drop in the microstrain.

Chapter 2. Stress, Texture and Microstructure in Nb Thin Films Sputter Deposited on Amorphous Substrates

Abstract. Thin films of pure Nb with thicknesses 5 nm, 20 nm, 100 nm and 500 nm were deposited by magnetron sputtering onto Si wafers covered with amorphous layers of SiO₂ and Si₃N₄ under ultra high vacuum conditions. The substrates were used in the as-received and sputter cleaned conditions. The as deposited films were analyzed with respect to chemical composition (by X-ray Photoelectron Spectroscopy sputter depth profiling), morphology (by Focussed Ion Beam imaging), texture, (macro) stress and microstrain (by X-ray diffraction methods) and surface morphology (by Atomic Force Microscopy). Further, the film/substrate system was investigated by X-ray reflectometry. The columnar morphology of the Nb films is not influenced by the type and the surface condition of the substrate. The dominant texture component in the Nb films is a {110} fibre texture typical of bcc metals, with a minor texture component resulting from twinning. Texture development in the film is primarily dictated by the type of substrate and the cleaning conditions. Nb films deposited onto amorphous SiO₂ substrates exhibit less sharp textures than those deposited onto amorphous Si₃N₄ substrates. Sputter cleaning of the substrates prior to film deposition led to a sharper texture in the Nb films, with the largest effect on films deposited onto Si₃N₄ substrates. X-ray diffraction $\sin^2\psi$ stress analysis revealed that the Nb films are subjected to compressive stress parallel to the surface. The ultra thin films have higher overall stress values than thicker films, with values of the order of a few GPa. These stresses were ascribed to the formation of oxides at the films grain boundaries close to the film surface. This interpretation is supported by the measurement and simulation of X-ray reflectometry data. By grazing incidence X-ray diffraction the existence of a stress gradient in the Nb films was confirmed. Line profile analysis showed that the crystal microstructural imperfection is larger for the films with less pronounced texture.

1. Introduction

The performance of thin metallic films in technical applications is determined by a variety of properties, such as thickness, grain and surface morphology, crystallographic texture, structural imperfections, chemical composition and impurities and, in particular, by residual stresses. These properties depend on the specific methods of film production (vapour deposition, sputter deposition, electrodeposition, etc.) and on the conditions during their production, such as the

working-gas pressure, temperature and electrical power in case of sputter-deposited films. These dependencies offer the possibility to influence, or even tailor, the properties of a thin film and thus to achieve an end product capable of withstanding specific external influences while in service. Thus an increasing amount of research has been devoted to thin films.

The origin of morphologies, textures and stresses of thin metallic films has extensively been studied [6, 9, 43, 47-55]; in particular, in case of sputtered films, the influences of the working-gas pressure and the deposition temperature have been considered. On the other hand, the influences of the type of substrate and its treatment prior to film deposition, although recognized as important, have been much less explored.

Refractory-metal thin films have gained increasing interest for engineering applications. Niobium as a pure metal is very reactive and forms an extremely stable oxide layer when exposed to air, which enhances its corrosion resistance. Its high melting point and yield strength make it capable of enduring highly demanding thermally and mechanically imposed stresses. Thus Nb films can be used as a stable protective coating of materials [56]. As an alloying element Nb can improve the superconducting or semiconducting properties of alloys [57]. Replacement of Pb-alloy films by Nb as electrode material in superconductive computers has increased their stability during thermal cycling [58].

The development of stresses in pure Nb films has been reported in literature [48, 50, 59, 60] and found to depend on the deposition temperature, contamination of the film and/or recrystallization. The compressive stress in very thin vapour-deposited Nb films was considered to be due to diffusion of oxygen atoms into Nb grain boundaries [50], according to a model proposed in Ref. [61].

In the present study sputter-deposited Nb films were investigated. Using a variety of techniques for film characterisation, for the first time a comprehensive picture is presented of the composition (contamination), microstructure, including crystal imperfection, texture and residual stress of bcc Nb films. As in our previous work on (fcc) Cu films [62-64], emphasis has been on the influence of the type of substrate, amorphous SiO₂ and amorphous Si₃N₄, including its surface condition, and of the film thickness on the properties of the Nb films.

2. Experimental

2.1 Substrate preparation and film deposition

Niobium films of various thicknesses were grown using a magnetron sputter deposition device. The layers were deposited on two commercially available Si-wafer substrates: 500 μm Si (510)/50 nm amorphous-SiO₂ and 500 μm Si (100)/50 nm amorphous-SiO₂/50 nm amorphous-Si₃N₄, each with a diameter of 100 mm; these substrates are called SiO₂ and Si₃N₄ substrates in the following. The substrates with dimensions of 14 mm \times 14 mm were used in both the as-received and sputter cleaned conditions. Sputter cleaning was performed in-situ in the Nb layer deposition chamber for 1 min using Ar ions accelerated at 100 V and at a pressure of 1.0×10^{-1} Pa. The ion current was maintained at 0.215 A so as to ensure a constant ion dosage to the substrates during cleaning. Film deposition was carried out at a temperature of 100 °C under ultra high vacuum conditions, a base pressure of 5×10^{-7} Pa, working gas (Ar) pressure of 46×10^{-2} Pa and a sputtering power of 100 W, with the specimen holder rotating at 12 rpm. From the film thickness of one Nb sample, measured by profilometry, and the sputter time, a deposition rate of 0.15 nm/sec was determined. This has subsequently been used to determine the film thicknesses of all the Nb samples grown. Film thicknesses of 5, 20, 100 and 500 nm were sputter deposited on uncleaned (U) and sputter cleaned (C) SiO₂ and Si₃N₄ substrates.

2.2 X-ray photoelectron spectroscopy (XPS)

XPS was used for the determination of the composition depth profiles in the Nb films of thicknesses 5, 20 and 100 nm. The XPS spectra were recorded using a VG ThetaProbe instrument. Monochromatic Al K α ($h\nu = 1486.6$ eV) radiation was used to generate the photoelectrons. The X-ray beam was focussed to give a spot size of 400 μm on the sample. The energy scale of the analyzer was calibrated such that the maximum intensity of the Ag 3d_{5/2} peak of pure silver is at 368.20 eV. Survey spectra were obtained in the binding energy range of 0 to 1400 eV. Detailed spectra were subsequently recorded in the binding energy ranges of 90 –110 eV (Si 2p), 195 –335 eV (Nb 3d), 275 – 295 eV (C 1s), 390 – 410 eV (N 1s) and 520 – 540 eV (O 1s). All spectra were measured at constant pass energy and at two detection angle ranges (37° – 76° and 30° – 37°) with respect to the sample surface. No tilting of the sample was required during these measurements since the instrument allows parallel collection of electrons departing the sample at different detection angles. A time dependent sputtering was carried out with a 3 keV Ar⁺ ion beam rastering

over an area of about $1 \times 1 \text{ mm}^2$ for each of the specimen investigated. Snapshot spectra of the Si 2p, Nb 3d, C 1s, N 1s and O 1s binding energy ranges were measured after each sputter cycle. Sputter profiling was stopped as soon as Nb signals had disappeared in the spectra. An estimation of the sputter rate of 5.9 nm/min was obtained from depth profiling of a 30 nm Ta₂O₅ layer on Ta.

2.3 Atomic force microscopy (AFM)

A Digital Instrument AFM device operating in the tapping mode, with Si tip cantilevers of 5-10 nm nominal curvature and resonance frequency of 296-358 KHz was used to determine the surface morphology Nb films. The roughness was represented as the standard deviation of the height distribution obtained for an image size of $10 \mu\text{m} \times 10 \mu\text{m}$.

2.4 Focussed ion beam (FIB) imaging

The morphology of the thicker films (100 nm and 500 nm) was investigated using a FEI FIB 200 microscope operating at 12 and 66 pA with a Ga⁺ beam accelerated at 30 keV. Imaging of the Ga⁺ beams affords contrast between grains of different crystallographic orientation due to variations in the yield of secondary electrons from the channeling of the ion beam. For a given orientation of the sample, grains with their low index crystallographic planes parallel to the ion beam appear relatively dark while higher index crystallographic planes appear relatively light. Cross sections were prepared by milling a trench in the film, then tilting the sample by 45° and recording the FIB-induced secondary electron image from the sidewall of the trench. FIB investigation of thin film microstructure has proved to be fast due to the absence of an elaborate specimen preparation requirement. However since the imaging process involves the sputtering away of material from the specimen, layer thickness determination by this method leads to underestimates for the layer thickness.

2.5 X-ray diffraction (XRD)

$\theta/2\theta$ scans were performed on a PHILIPS MPD diffractometer applying Bragg-Brentano geometry. The X-rays were generated from a Cu tube with the generator operating at 45 kV and 40 mA. A primary monochromator was used to select Cu K α_1 radiation. An incident beam slit of 10 mm

(beam height) and a divergence slit of 0.25° were used. In the diffracted beam path an anti-scatter slit of 0.25° , a receiving slit of height 0.3 mm and a proportional detector were used.

The measured intensity data were fitted with a Pseudo-Voigt function using the PHILIPS ProFit software [18]. From the fit, the characteristic parameters of the individual peaks were evaluated: position, integrated intensity, integral breadth, full width at half maximum, peak shape (Lorentzian-Gaussian mixture and asymmetry). The 110 and 220 peaks of Nb as recorded in the $\theta/2\theta$ using Bragg – Brentano geometry are used for line-broadening analysis.

Pole figure scans and stress measurements were performed on a PHILIPS X'Pert MRD diffractometer equipped with an Eulerian cradle, using a Cu $K\alpha$ radiation with the X-ray generator operating at 45 kV and 40 mA. With the aid of a X-ray lens in the incident beam path, a foil collimator and a monochromator in the diffracted beam path parallel beam optics was achieved. When a combination of two tilt angles, i.e. rotation around two axes lying in the sample surface and perpendicular to each other, are used as variables in a stress measurement, it is necessary to distinguish (more carefully as usually done in literature) between the instrumental angles and the angles describing the measurement direction with respect to the sample. The following definitions will be used [65] (see Fig. 2.1):

$2\theta_{hkl}$: Diffraction angle of reflection hkl imposed by the lattice spacing d_{hkl} and set by the position of the detector.

ψ : tilt angle of diffracting lattice planes with respect to the sample surface, i.e. the angle between the plane normal (coinciding with the diffraction vector) and the sample surface normal.

χ : tilt angle (instrumental) of the sample around an axis perpendicular to plane defined by the incident and diffracted beam.

ϕ : rotation angle around the sample surface normal.

Ω : offset angle around an axis parallel to the θ -axis (for symmetrical Bragg-Brentano geometry: $\Omega=0^\circ$). χ -mode: $\psi = \chi$ ($\Omega=0^\circ$) and Ω -mode: $\psi = \Omega$ ($\chi = 0^\circ$)

Pole figure scans were made at fixed Bragg angle (corresponding to a specific reflection) by recording intensity data as the specimen is scanned through a 360° ϕ rotation at stepped tilt angles (usually ranging from $0^\circ \leq \psi \leq 88^\circ$). Stress measurements were performed by measuring $\theta/2\theta$ scans of hkl peaks at different ψ values ($0^\circ \leq \psi < 90^\circ$). Conventional measurements were performed by applying the χ -mode either using only the Nb 110 reflection or using multiple hkl. The so-called grazing incidence stress measurements were done using the combined χ - Ω -mode.

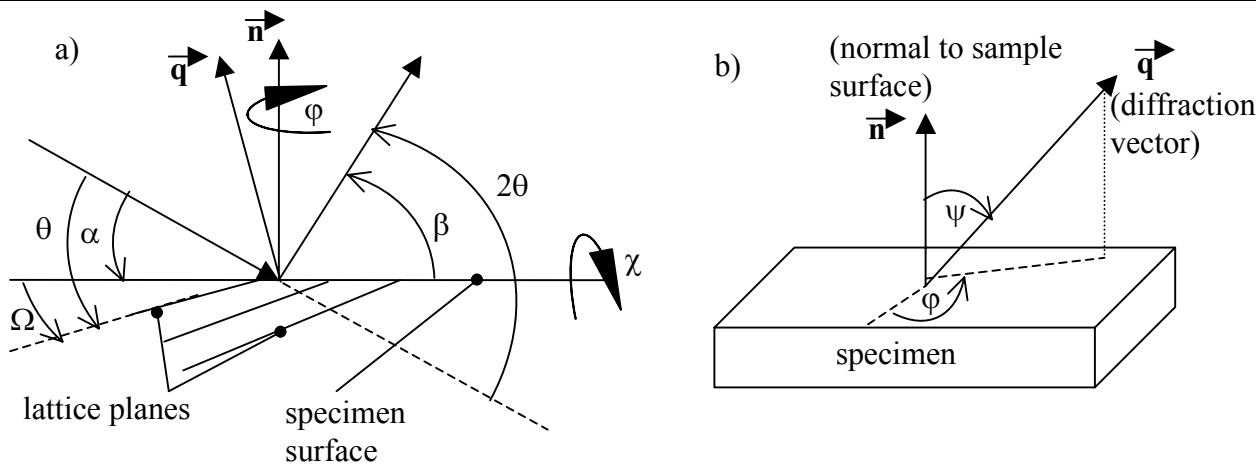


Figure 2.1. Schematic diagram showing the angles used in the present diffraction measurements (a) for the angles: the Bragg angle θ , the angle of incidence α and the diffracted angle with respect to the specimen surface β (shown for $\chi = 0$). (b) for the angles: the rotation angle ϕ and the tilt angle ψ between the diffraction vector and the normal to the sample surface (see text above for more details).

2.6 X-ray reflectometry

X-ray reflectometry was carried out using a Siemens D5005 θ - θ diffractometer equipped with an X-ray mirror for the selection of Cu $K\alpha$ radiation and a sample stage with a knife edge collimator above the sample in addition to the conventional slit system.

3. Results and Discussion

3.1 Chemical composition as a function of depth

For the determination of the atomic concentrations from the XPS spectra a linear background was subtracted from the individual photo-electron (composite) peaks and from the resulting peak areas the concentrations were calculated assuming that the samples are laterally homogenous and using the relative photoionisation cross-sections according to Refs. [66, 67]. XPS spectra for the Nb 3d peak and the O1s peak for a 5 nm thick Nb film and for a 20 nm thick Nb film, after different sputter times are shown in Fig. 2. In the spectra of the as-produced films taken with the larger take off angle of 52° (Fig. 2.2a, $t = 0$ s) four Nb peaks occur: two Nb peaks are characteristic for the oxide Nb_2O_5 and two Nb peaks are characteristic for the metallic Nb.

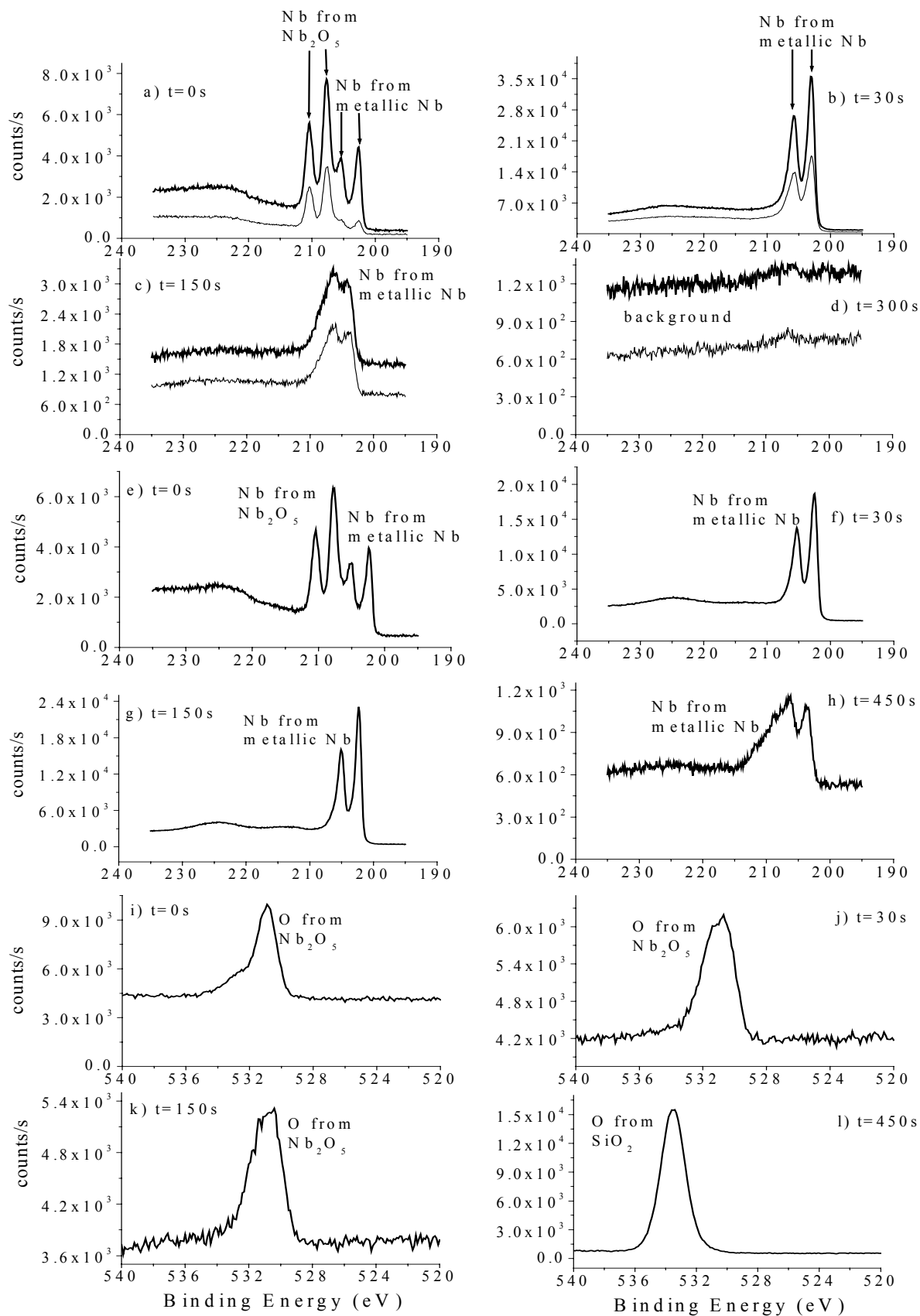


Figure 2.2. XPS spectra of Nb 3d and O 1s peaks. a)-d) 5 nm Nb film on uncleaned Si_3N_4 , at take off angles 52° (thick lines) and 22° (thin lines); e)-l) 20 nm Nb film on uncleaned SiO_2 , take off angle 52° . Note the different scales of the ordinates.

In the spectra data with the smaller take off angle of 22° the sampling volume is more restricted to the very surface. Apparently, the peaks for the metallic Nb then are absent indicating that the very surface of the film consists (at least mostly) of the Nb_2O_5 . Niobium is known to have a very high affinity for oxygen. When left in atmosphere a thin oxide layer easily forms [59, 68-72]. After sputtering 30 s (Fig. 2.2b), corresponding to a depth of about 3 nm, the peaks of the oxide disappeared whereas metallic Nb is still present. Evidently, the thickness of the surface oxide layer is smaller than 5 nm (the Nb film thickness). After sputtering for 150 s (Fig. 2.2c), corresponding to a sputter depth of about 12 nm, only traces of Nb are left. As the sputter depth is larger than the film thickness, these traces have to be ascribed to the intermixing effect caused by the sputter process during depth profiling. After 300 s (Fig. 2.2d) no Nb is observed anymore.

For the 20 nm thick Nb film the situation for 0 s (Fig. 2.2e) and 30 s sputtering (Fig. 2.2f) is the same as for the 5 nm thick film (Figs. 2.2a and b), indicating that the formation of the oxide layer on the surface does not depend on the film thickness.

The oxygen O 1s peak varies with depth: at the surface, it occurs at 531 eV (Fig. 2.2i) corresponding to Nb_2O_5 , and in the bulk after 450 s sputtering, it is found at 533.5 eV (Fig. 2.2l) corresponding to SiO_2 (i.e. due to the amorphous SiO_2 layer on the silicon wafer). It is important to note that for the 20 nm thick film after sputtering for 30 s, where the Nb peaks due to Nb_2O_5 have disappeared (Fig. 2.2f), still an O 1s peak occurring at 531 eV is visible (Fig. 2.2j), however with much lower intensity than as observed after 0 s. After 150 s (Fig. 2.2g) the peaks of metallic Nb have the same height as after 30 s (Fig. 2.2f), whereas the O 1s peak has become smaller (Fig. 2.2k). It is concluded that niobium-oxide formation extends into the film beyond the Nb_2O_5 layer at the top, albeit with an amount decreasing with depth. After 450 s sputtering the O signal observed (Fig. 2.2l) is representative of the SiO_2 layer on top of the Si wafer.

The atomic concentrations for all atomic species detected in Nb films deposited onto uncleaned and sputter cleaned SiO_2 substrates have been plotted in Fig. 2.3 versus the XPS sputter depth profiling time; similar results have been plotted in Fig. 2.4 for Nb films on Si_3N_4 substrates.

The carbon detected originates from either the vacuum pumps used in the XPS chamber giving rise to a uniform distribution of very low C content in the case of the sputter cleaned substrates (Figs. 2.3b and c) or is a contaminant on the uncleaned substrates detected as a peak at the layer-substrate interface (Fig. 2.3a).

The silicon derives from the substrate and thus occurs in the form of an oxide (as in SiO_2), a nitride (as in Si_3N_4) and of semiconductor Si (as in pure Si). The semiconductor form of Si detected in the specimens with cleaned Si_3N_4 substrates in the depth range where Si_3N_4 occurs (Figs. 2.4b and d) was found to be relatively high in intensity as compared to the other specimens. This observation

suggests that sputtering during the depth profiling more easily ruptures the Si-N bonds than the Si-O bonds.

Of particular significance, as seen in Figs. 2.2 and 2.3, is the low concentration of Nb at the film surface (at zero sputter time) and its sharp rise upon increasing sputter time. Over the same depth range, the oxygen concentration is observed to drop (see the above discussion on the presence of Nb at the very surface). The XPS results show that the depth z at which the layer oxidation had progressed is about the same in all the films irrespective of the layer thickness or substrate type.

The thickness of the stable Nb_2O_5 layer on top is estimated to be (smaller than) about 3 nm (see the above discussion with respect to Fig. 2.2). The results shown in Figs. 2.3 and 2.4 indicate the presence of some oxygen beyond the depth of 3 nm down to roughly 5 nm. This observation is ascribed to the presence of stable Nb_2O_5 and/or suboxides NbO_x [68] in the grain boundaries of the Nb film. However, it should be noted that the sputter process during depth profiling can be responsible for the formation of some NbO_x [73]. This observation has an important consequence for the interpretation of data reported and discussed in section 3.4.

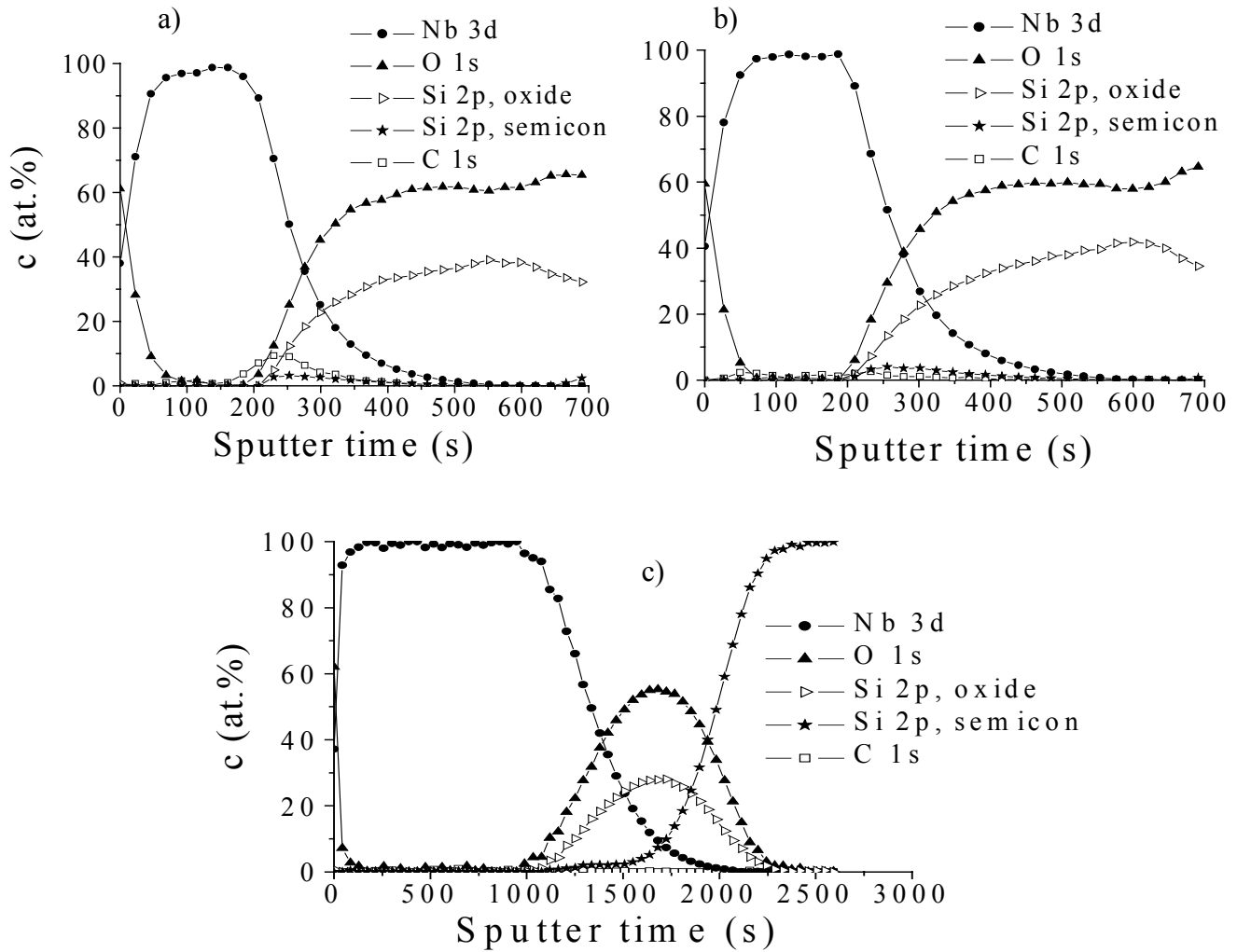


Figure 2.3. Atomic concentrations versus sputter time for 20 nm thick Nb film on (a) uncleaned SiO₂, (b) sputter cleaned SiO₂ substrate, and (c) 100 nm thick Nb film on sputter cleaned SiO₂ substrate.

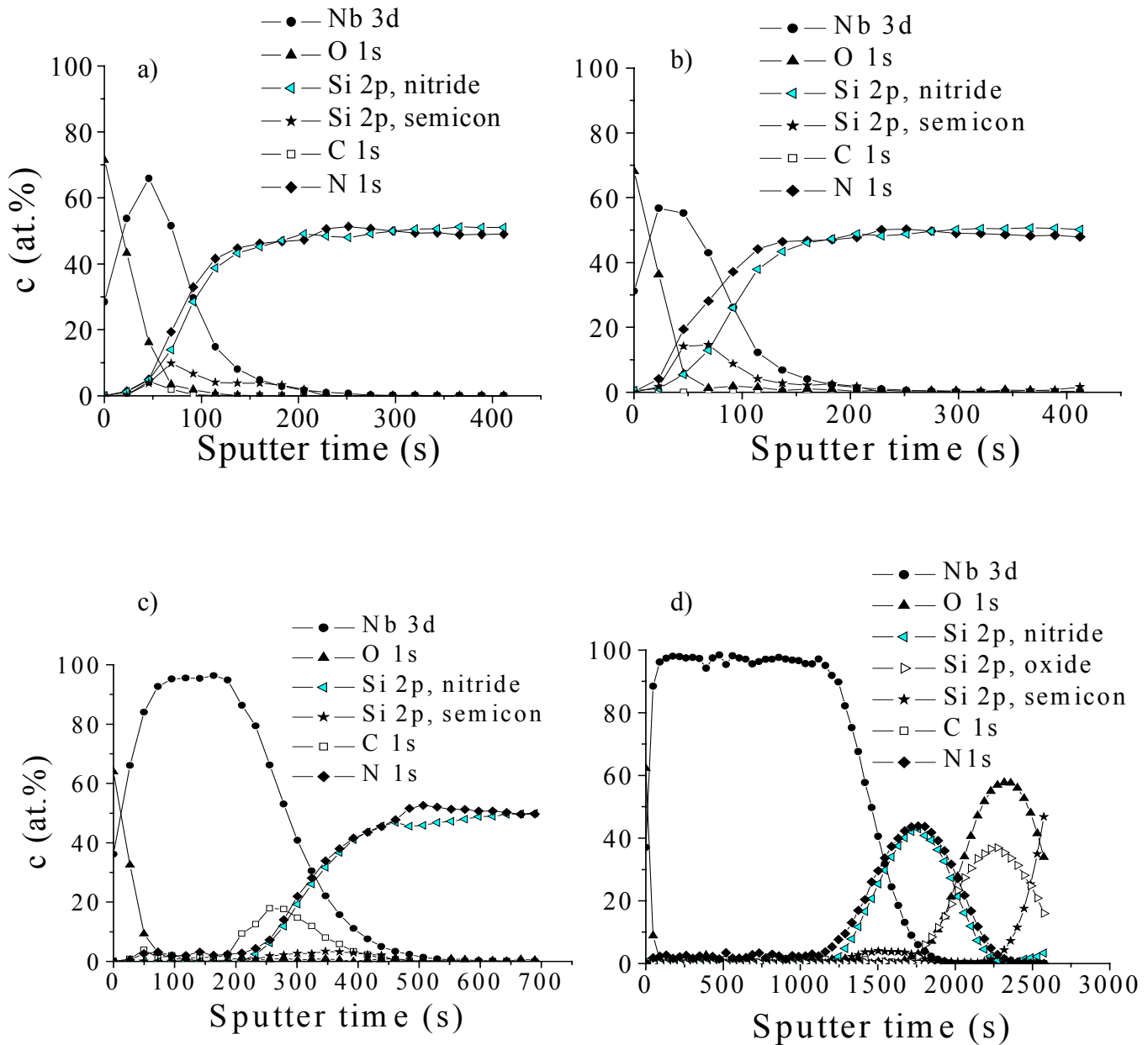


Figure 2.4. Atomic concentrations versus sputter time for 5 nm thick Nb film on (a) uncleaned Si_3N_4 , (b) sputter cleaned Si_3N_4 substrate, (c) 20 nm thick Nb film on uncleaned Si_3N_4 substrate, and (d) 100 nm thick Nb film on sputter cleaned Si_3N_4 substrate.

3.2 Morphology

3.2.1 Surface topography

The AFM topography images for Nb films of various thicknesses deposited on uncleaned and sputter cleaned SiO_2 and Si_3N_4 substrates are shown in Figs. 2.5 and 2.6.

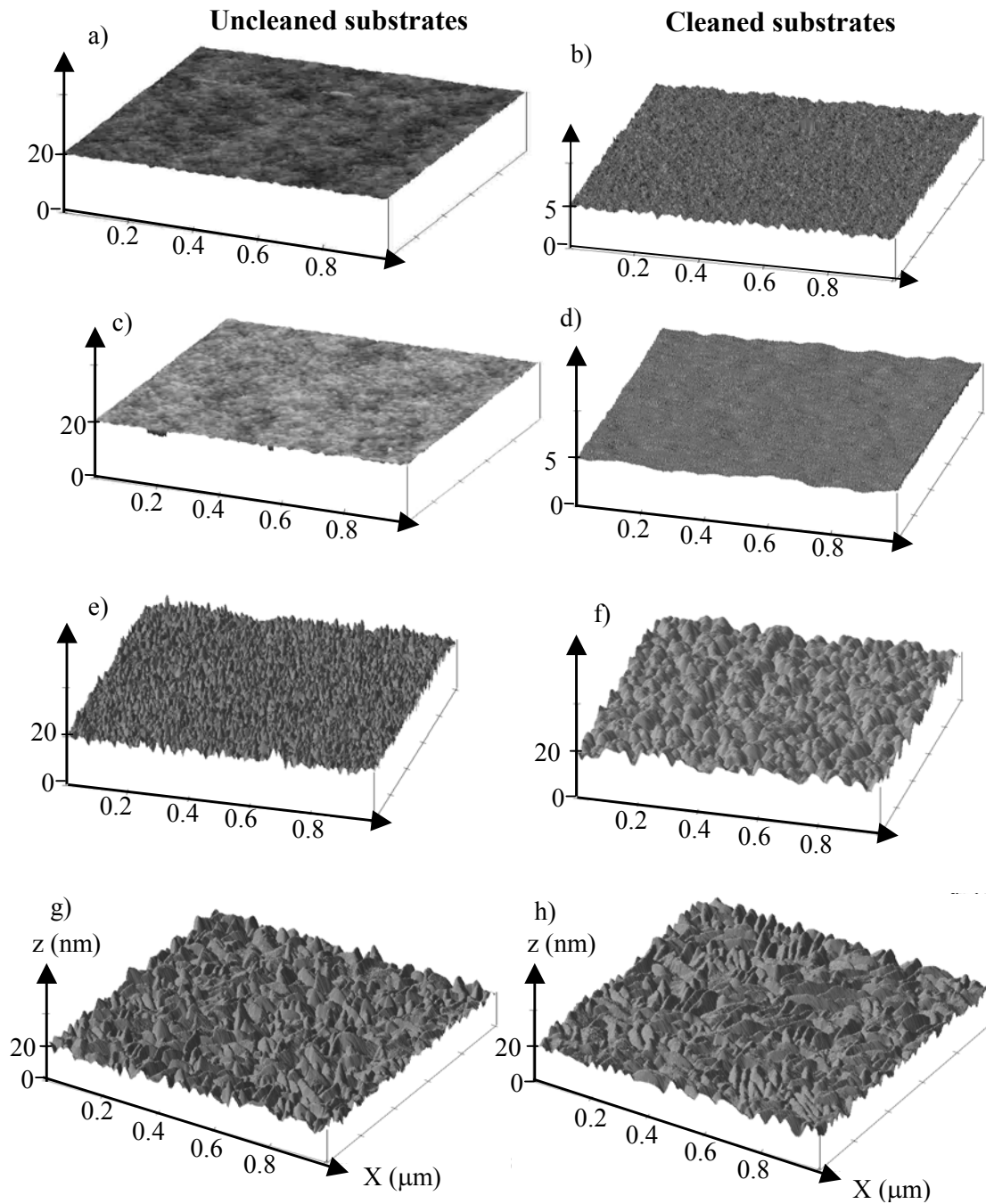


Figure 2.5. Three-dimensional AFM topography images of Nb films deposited on uncleaned and sputter cleaned SiO_2 substrates for (a, b) 5 nm, (c, d) 20 nm, (e, f) 100 nm, and (g, h) 500 nm thick Nb films.

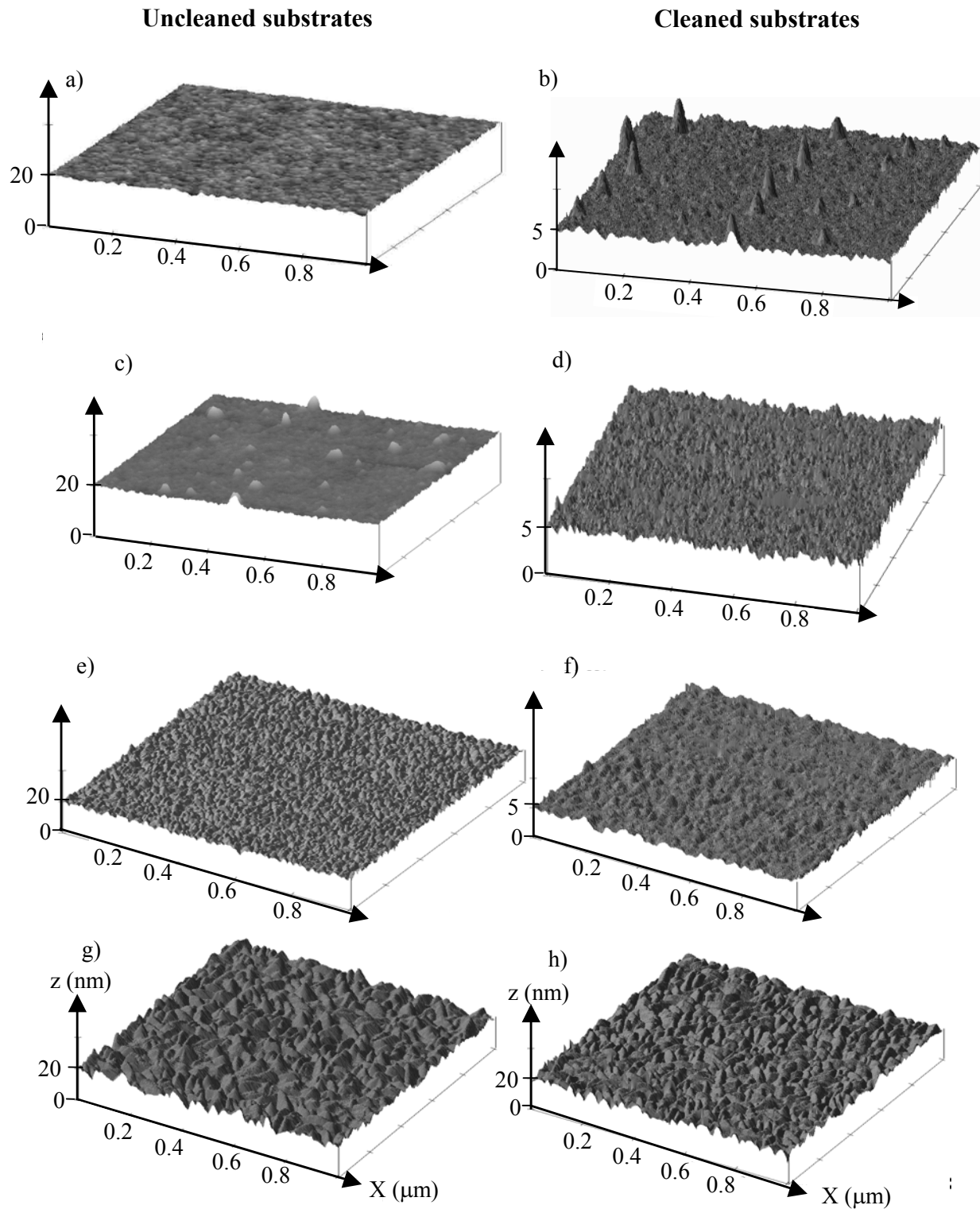


Figure 2.6. Three-dimensional AFM topography images of Nb films deposited on uncleaned and sputter cleaned Si_3N_4 substrates for (a, b) 5 nm, (c, d) 20 nm, (e, f) 100 nm, and (g, h) 500 nm thick Nb films.

The roughness values, R , (standard deviation of the height distribution) as obtained from the AFM data have been listed in Table 2.1. For the films on SiO_2 no systematic correlation between the roughness of the film surface and the substrate sputter cleaning condition is observed, whereas for the films on Si_3N_4 substrates a trend is observed that suggests that the films on cleaned substrates are smoother. For both substrates (SiO_2 and Si_3N_4) a systematic trend of an increasing roughness with increasing film thickness is observed.

Some of the films deposited on Si_3N_4 substrates show protrusions that were hillock-like. For the 5 nm thick film they occur on the cleaned substrate with a lateral extension of about 50 nm and a height of about 2 nm, whereas for the 20 nm film they occur on the uncleaned substrate with a lateral extension of 50 nm and a height of about 6 nm. This effect gives rise to relatively large roughness, R , values as compared to the films that do not exhibit such protrusions.

From the two-dimensional AFM data the height distributions $p(h)$ were calculated. Examples are shown in Fig. 2.7 for a 20 nm thick film on cleaned Si_3N_4 exhibiting so-called normal behaviour and for a 20 nm thick film on uncleaned Si_3N_4 exhibiting protrusions in the AFM picture (Fig. 2.6). The normal behaviour is defined as a mono-modal (more or less symmetrical) distribution around the average height (corresponding to $h = 0$ in Fig. 2.7) which can well be described by mainly a Gaussian function and a small Lorentzian contribution to account for the tails. For the film exhibiting protrusions a bimodal distribution is obtained (Fig. 2.7): an additional peak around $h = 3$ nm occurs. The amplitude of this contribution is quite small (smaller by two orders of magnitude than the contribution around $h = 0$) and thus is visible only in a logarithmic representation of $p(h)$.

Noting that the Nb films have a columnar microstructure (section 3.2.1) the pyramidal features observed in Figs. 2.5g,h and 2.6g,h are attributed here to the columnar grains. Thus it is deduced that the columnar structure development begins after the first few tens of nanometer (earlier for the films on Si_3N_4 substrate (Fig. 2.6d) than for the films on SiO_2 substrate (Fig. 2.5e)). At 100 °C deposition temperature the Nb atoms have rather low atomic mobility which results in a kinetic roughening of the substrate surface as observed here. A consequence of this is shadowing of lower regions on the substrate surface by higher regions that receive more material from the sputter source [55, 74, 75].

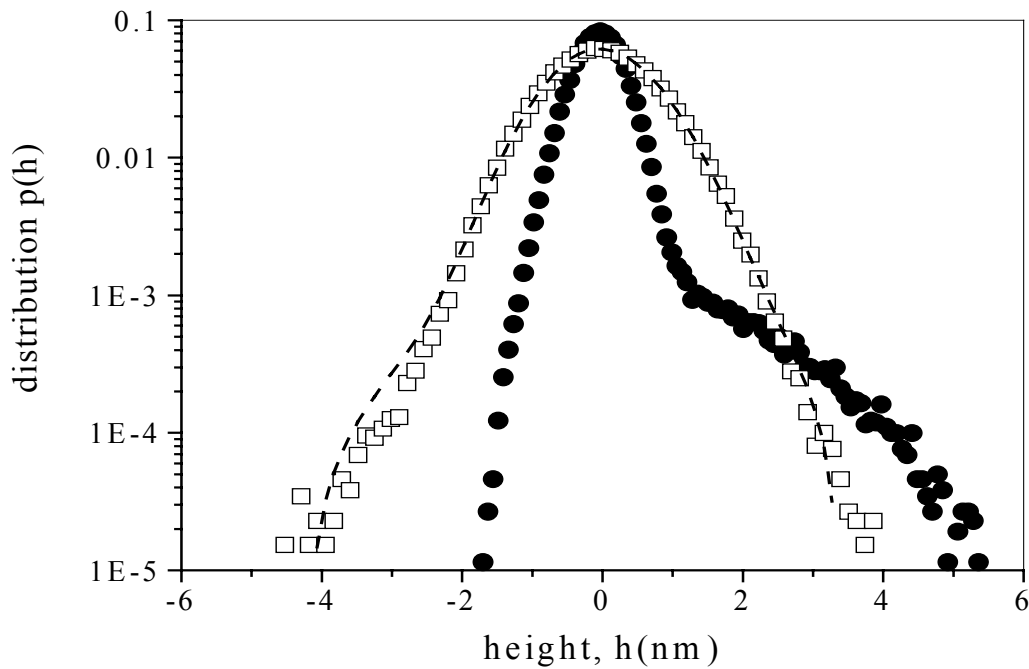


Figure 2.7. Height distribution $p(h)$ for 20 nm thick Nb films on Si_3N_4 substrate. \square cleaned substrates, fitted (---) using a slightly asymmetrical pseudo Voigt function (see text), \bullet uncleaned substrate, not fitted. Note the logarithmic $p(h)$ scale.

3.2.2 Grain size

The grain sizes of the Nb films were determined from the AFM data using two methods: the linear intercept method as described in [16] and an auto-correlation function method (described below). The results obtained using these methods have been listed in Table 2.1.

The morphology of the film surface in lateral directions can be characterised by a characteristic length for the lateral extension of the height fluctuations. This can be done in a quantitative way employing the concept of the height-height correlation function. The auto-correlation function of the height fluctuations around the average height $h(\mathbf{R})$ is defined as:

$$g(\mathbf{R}) = \frac{\langle h(\mathbf{R}_1) \cdot h(\mathbf{R}_2) \rangle}{\langle h(\mathbf{R}_1)^2 \rangle}, \quad (2.1)$$

where the vectors \mathbf{R}_1 and \mathbf{R}_2 denotes two points on the surface with distance $R = |\mathbf{R}_1 - \mathbf{R}_2|$. The average $\langle \dots \rangle$ is taken over all points of the film surface, and the normalisation is such that $g(R=0) = 1$.

From the two-dimensional AFM data the auto-correlation function for the height fluctuation was calculated. Representative examples for the 5 nm, 100 nm, 500 nm thick Nb films on uncleaned Si_3N_4 substrates are shown in Fig. 2.8. The oscillations of $g(R)$ following the drop of $g(R)$ from $g(R) = 1$ at $R = 0$ to its first minimum value reveal that the fluctuations of the height are not purely random, but correlated with distance. It is suggested that the wavelengths of these fluctuations can be attributed to the lateral grain size of the Nb films. As a quantitative measure the position D of the second maximum was taken, as indicated in Fig. 2.8 (the distance between a central grain at $R = 0$ and an adjacent grain at $R = D$ corresponds to the diameter of the grains).

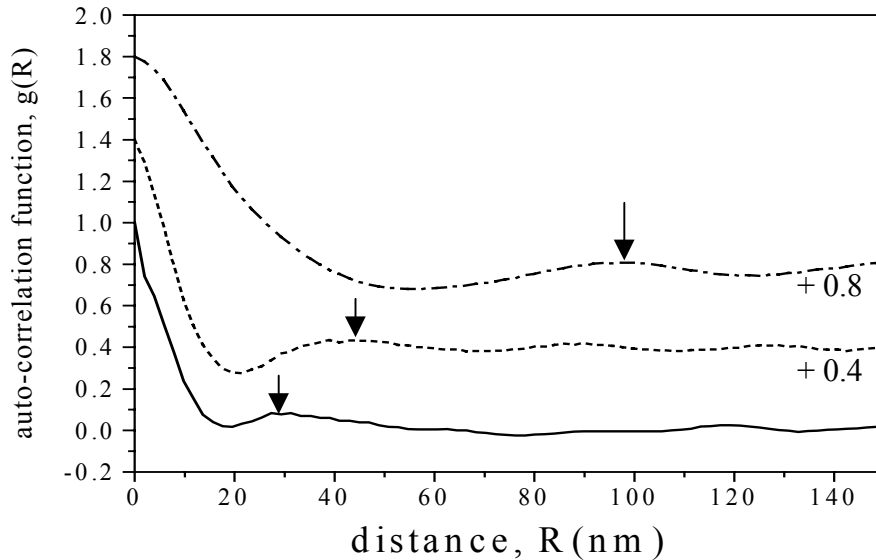


Figure 2.8. Height-height auto-correlation function $g(R)$ for Nb films on uncleaned Si_3N_4 substrates, with thickness of 5 nm (—), 100 nm (----) and 500 nm (- - -). The arrows indicate the positions of the second peak from where D values (Table 2.1) have been obtained (the curves for the 100 and 500 nm thick films are displaced upwards for clarity).

The values of D as obtained from the height-height auto-correlation function compare well with those obtained from the linear intercept method (A). The grain sizes, between 30 nm and 100 nm (see results given in Table 2.1), exhibit a trend for increase with increasing film thickness. The 5 nm thick films are at the coalescence stage of the film growth because portions of the substrate

are not covered yet by the Nb deposits (see e.g. black regions in Fig. 2.5a) thus the corresponding values of the lateral size in Table 2.1 represent island sizes.

For both film systems (SiO_2 and Si_3N_4 substrates) the average lateral grain sizes are comparable (Table 2.1). For the 5 and 20 nm thick films the size is about 30 nm. The increase of the grain size with film thickness becomes clear at a thickness of 100 nm, in particular for films deposited on cleaned substrates.

The grain size in the film are within the nano-scale (≤ 100 nm) and according to the deposition conditions, conform to the zone T microstructures indicated for sputter deposited films in the structure zone model [13]. The zone T structures are characterised by densely packed fibrous grains thought to represent a transition from the more porous zone 1 structures (consisting of tapered crystallites separated by voids) to zone 2 structures (typified by distinctly columnar grains).

Table 2.1. The average lateral grain size as obtained from the linear intercept method (A) and as obtained from the height-height auto-correlation function (D) and the roughness, R, for Nb films of various thicknesses deposited on uncleaned (U) and sputter cleaned (C) SiO_2 (upper) and Si_3N_4 (lower) substrates.

Film thickness (nm)	5 (U)	5 (C)	20 (U)	20 (C)	100 (U)	100 (C)	500 (U)	500 (C)
A (nm)	37	32	30	22	35	67	70	80
D (nm)	40	21	40	75	54	140	78	91
R (nm)	0.41	0.41	0.50	0.56	0.9	1.63	1.98	1.63

Film thickness (nm)	5 (U)	5 (C)	20 (U)	20 (C)	100 (U)	100 (C)	500 (U)	500 (C)
A (nm)	33	42	30	30	50	60	100	90
D (nm)	30	53	57	29	44	47	98	90
R (nm)	0.57	0.91	1.2	0.40	1.06	0.53	1.77	1.23

Cross sections of the thicker films (500 nm), as revealed by FIB imaging, are shown in Fig. 2.9. Clearly, the grains in the films on both substrate types are of columnar morphology. The column width/average grain size was determined by the linear intercept method and found to be about 130 nm in all the 500 nm thick films. This signifies that there is no marked influence of the substrate type and cleaning prior to layer deposition on the film morphology. Comparing the grain size obtained from the FIB imaging with A and D for the 500 nm thick Nb films in Table 2.1 suggests an overestimation of the grain size as obtained by the FIB imaging technique. This difference is attributed to the experimental inaccuracies of the techniques used: for the FIB method a point resolution of 20 nm is possible and small grains may be missed whereas for the AFM method a resolution range of 5 – 10 nm is achievable (depending on the cantilever tip size).

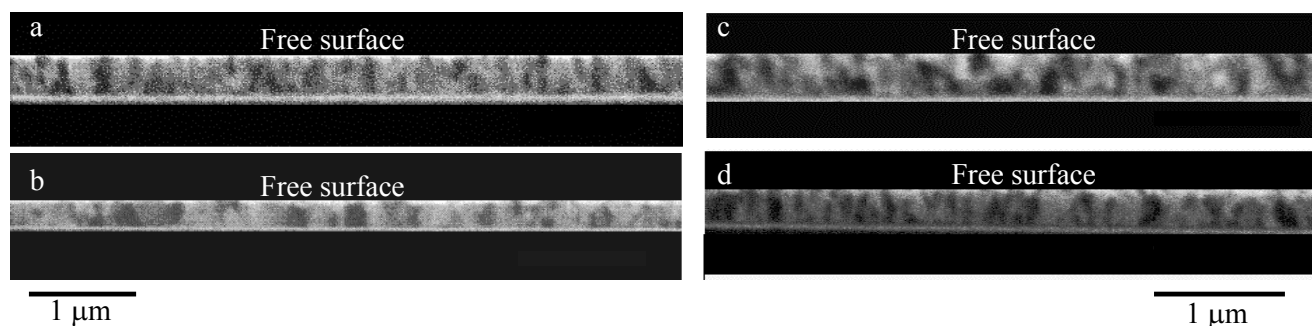


Figure 2.9. FIB images of sputter deposited 500 nm thick Nb films on (a) uncleaned (b) sputter cleaned SiO_2 substrates, and (c) uncleaned (d) sputter cleaned Si_3N_4 substrates.

3.3 Texture

3.3.1 $\theta/2\theta$ scans

The diffractometer scans depicted in Fig. 2.10, recorded from the Nb films, revealed the presence of only two reflections (110 and 220) over the scan range ($33^\circ \leq 2\theta \leq 140^\circ$).

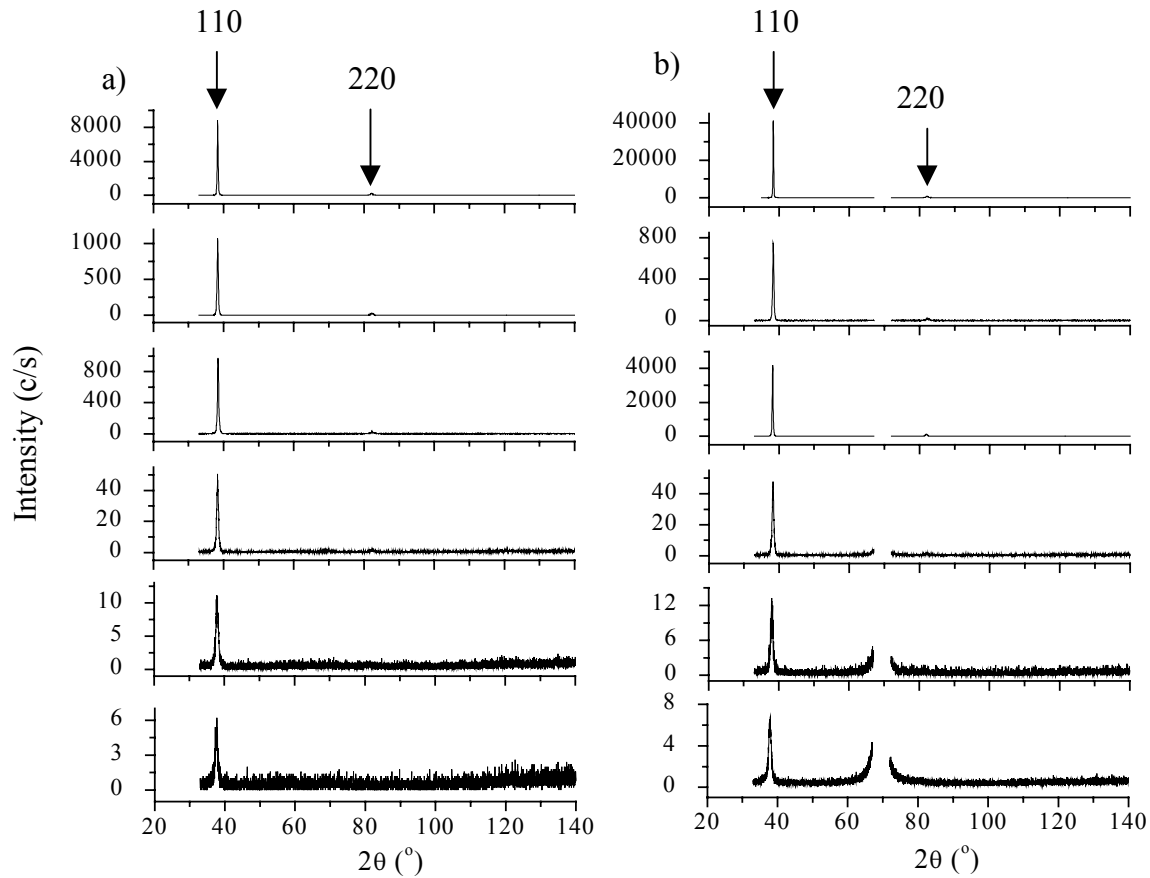


Figure 2.10. X-ray diffraction patterns ($\theta/2\theta$ scans) of Nb films of various thicknesses deposited on (a) SiO_2 substrates and (b) Si_3N_4 substrates, at uncleaned (U) and sputter cleaned (C) substrate conditions. The gap around $2\theta = 70^\circ$ in (b) is where the Si 400 reflection from the substrate occurs.

For the films deposited on Si_3N_4 substrates, the 400 reflection of the base single crystal Si 100 wafer substrate occurring at $2\theta = 69^\circ$ was found to be of very high intensity and hence was avoided during measurement in order to protect the detector from damage. The absence of this feature in Fig. 2.10a is because the single crystal Si wafer beneath the SiO_2 layer has a 510 orientation (see section 2.1); within the diffraction scan range of Fig. 2.10 Si 510 has no reflection. It was not possible to obtain enough diffraction intensity for the ultrathin (5 nm) films due to the limited diffracting volume of the specimens.

For a textureless Nb specimen eight reflections with specific relative intensities would be detected within the scan range. For the sputtered Nb film no traces of other reflections besides 110 and 220 were detected. Hence the Nb films are textured: the Nb crystals have predominantly 110 planes parallel to the surface.

It is observed that the intensity of the Nb 110 peak for the films deposited on cleaned substrates is much higher than for those on uncleaned substrates, revealing that substrate cleaning prior to the deposition of the film leads to a more perfect $\{110\}$ texture.

3.3.2 Pole-figure scans

In $\theta/2\theta$ scans only planes parallel to the sample surface can give rise to diffraction peaks in the Bragg-Brentano geometry. Hence the $\theta/2\theta$ scan defines only a limited number of points in orientation space. For determination of the (full) orientation distribution, so-called pole figure scans have to be made. Despite this advantage of pole figure scans over the $\theta/2\theta$ scan for characterisation of the texture, both characterisation methods complement each other as has been shown in [64] where a $\theta/2\theta$ scan rather than a pole-figure scan was found to more accurately account for the presence of the fraction of randomly oriented crystals in the film.

A complete pole-figure scan, recorded using the Nb 110 reflection, is shown in Fig. 2.11. Clearly a $\{110\}$ fibre texture occurs, with the fibre axis normal to the surface. The rotational symmetry about the fibre axis implies that all texture information is obtained by measuring the 110 peak intensity upon tilting the specimen at constant ϕ (ψ scans): these scans will be called here “fibre plots”. The half width at half maximum (HWHM), of the peak around $\psi = 0^\circ$ (the fibre axis) and the intensity at $\psi=0^\circ$ are used as the fibre texture quantifying parameters. If only the $\{110\}$ fibre texture occurs, as shown by the $\theta/2\theta$ scans, it is only the sharpness of the texture that can vary and thus the height $I_{\psi=0^\circ}$ and the HWHM contain the same information.

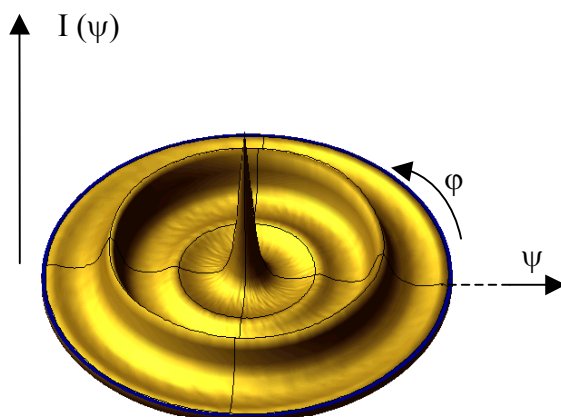


Figure 2.11. $\{110\}$ Pole figure for a 500 nm thick Nb film deposited on a-SiO₂ substrate.

The 110 fibre plots for the Nb films, as defined above, are shown in Fig. 2.12. The $I(\psi)$ functions have been corrected for background, absorption, thickness and intensity loss due to geometric effects [28], thereby permitting a direct comparison of films of different thickness.

For the ultrathin 5 nm films on uncleaned and cleaned SiO₂ substrates and on uncleaned Si₃N₄, the Nb 110 peak cannot be detected in the $\theta/2\theta$ scan (i.e. at $\psi = 0$). Thus the correction of the $I(\psi)$ scan for background, which is based on the subtraction of an average background, determined by a $I(\psi)$ scan recorded at 2θ values at either side of $2\theta_{110}$ [19], from $I_{2\theta,110}(\psi)$, was not possible. Apparently, for these films the $\{110\}$ texture is too broad or absent to generate a detectable peak in $I(\psi)$ at $\psi = 0$. For the 5 nm film on cleaned SiO₂ substrate only a weak indication for some structure in the $I(\psi)$ scan is seen, whereas for the 5 nm film on cleaned Si₃N₄ substrate a distinct peak at $\psi = 0$ occurs. The fibre texture developed earlier in the film deposited onto the Si₃N₄ substrate than in that deposited onto the SiO₂ substrate.

The texture of the films deposited onto Si₃N₄ substrates is generally sharper than that of the films deposited onto SiO₂ substrates (see the HWHM data given in Fig. 2.12). For both substrate types the effect of substrate cleaning prior to film deposition was found to yield a sharpening of the $\{110\}$ fibre texture component. For increasing film thickness the texture becomes sharper and this effect is more pronounced for the films on Si₃N₄.

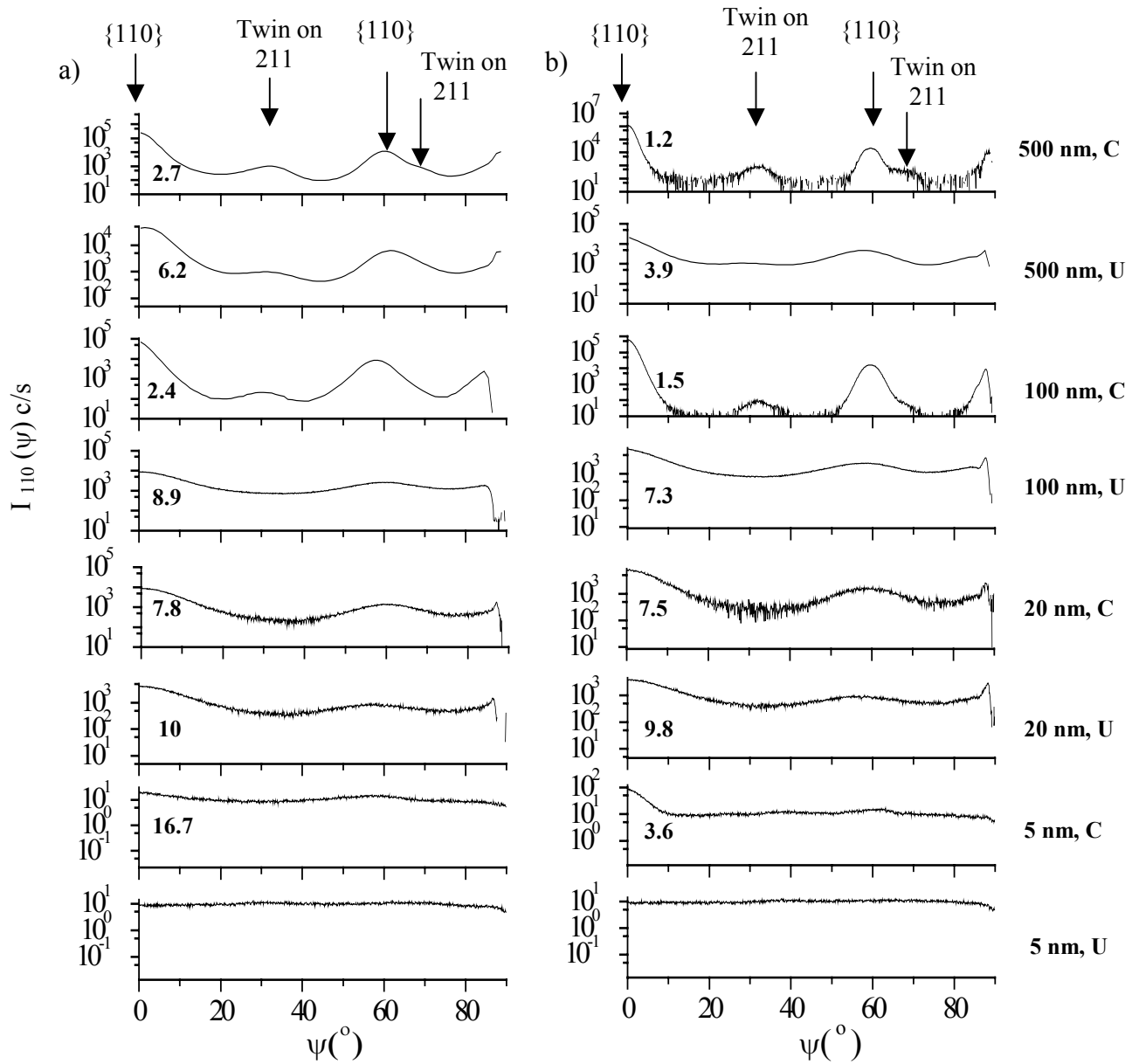


Figure 2.12. 110 fibre plots (see text) for Nb films of various thicknesses deposited onto uncleaned and sputter cleaned substrates for (a) SiO₂ substrates, (b) Si₃N₄ substrates. The HWHM (in $^\circ$) have been indicated for the 110 peak at $\psi = 0^\circ$. (U = uncleaned substrates, C = cleaned substrates)

The bcc Nb crystals with $\{110\}$ planes parallel to the surface give rise to peaks in the fibre plots at $\psi = 0^\circ$ and at $\psi = 60^\circ$. At about $\psi = 33.6^\circ$ and 70.5° two additional peaks are observed. These peaks can be ascribed to first generation twins formed on 211 planes of the Nb crystals with $\{110\}$ parallel to the surface. Twinning in bcc structures on the 211 planes is normal [27, 76, 77]. The peaks in the fibre plots due to this type of twinning were observed only for the 500 nm thick films

and the 100 nm thick films deposited on sputter cleaned substrates. On a $\theta/2\theta$ scan these twinned parts of the Nb films are not detectable because their diffracted intensities are below the detection limit.

The mechanisms responsible for the degree of perfection of the $\{110\}$ fibre texture of the Nb films are likely to be similar to those discussed for the $\{111\}$ texture of Cu films deposited on the same types of substrates [62]. The type of the texture, $\{110\}$ for Nb and $\{111\}$ for Cu, is dictated by surface energy minimization [11, 12, 40]. The 110 planes are the most densely packed planes in bcc materials and the free surface energy of this plane is the smallest as compared with that of other hkl planes. Thus, during thin film production of bcc materials, grains tend to grow with their 110 planes perpendicular to the growth direction (i.e. parallel to the film surface).

At the early stage of film growth, the crystalline (i.e. highly ordered) structure of the metal film has to develop on an amorphous (i.e. disordered) substrate surface. The atomic interactions between the metal atoms and the atoms of the amorphous substrate can locally obstruct the formation of perfect crystalline order, and thereby fluctuations of the orientation of the nucleating crystals is feasible as well. In particular the oxygen atoms at the SiO_2 substrate surface provoke such hindering effects due to their strong interaction with niobium. On uncleaned Si_3N_4 substrates oxygen (and carbon) is (are) present as an impurity contamination, whereas on SiO_2 oxygen is a constituting component. This explains why sputter cleaning is more effective for Si_3N_4 than for SiO_2 with respect to an increase of the texture perfection. However, also for the SiO_2 substrates cleaning causes enhancement of the Nb $\{110\}$ fibre texture. This may be explained by the stronger hindering effect for adsorbed O impurity atoms than for constituting O atoms (incorporated in SiO_2) and/or by the additional hindering effect of carbon impurity atoms, which both are removed by sputter cleaning. The increase of the perfection of the texture with increasing film thickness may be explained recognizing that continual material deposition occurs on highly ordered crystalline (i.e. no longer amorphous) material and/or the preferred growth of more ideally oriented crystals.

3.4 Residual stress

3.4.1 Conventional $\sin^2\psi$ method

The 110 reflection of the Nb films was used for the X-ray diffraction stress analysis. The lattice spacing d_{ψ}^{110} was determined by conducting $\theta/2\theta$ scans at various tilt angles ψ and calculating d_{ψ}^{110} from Bragg's law.

In the fibre textured Nb films a plane rotationally symmetric stress state is present (measurements at different ϕ yielded the same stress values) and the in-plane residual stress, $\sigma_{//,r}$, can be determined from [34]:

$$\varepsilon_{\psi}^{hkl} = \frac{d_{\psi}^{hkl} - d_0^{hkl}}{d_0^{hkl}} = \left[2S_1^{hkl} + 1/2S_2^{hkl} \sin^2\psi \right] \sigma_{//,r}. \quad (2.2)$$

where d_0 , is the stress free lattice spacing and S_1^{hkl} and $1/2S_2^{hkl}$ are the so-called X-ray elastic constants for the film. The Neerfeld-Hill value for $1/2S_2^{hkl}$ taken for 110 Nb, 14.01 TPa^{-1} , calculated from the single crystal elastic constants from [78] was used for this study (see e.g. [34]). The stress, $\sigma_{//,r}$, can be calculated from the slope of a straight line fitted to the data in the d_{ψ}^{hkl} versus $\sin^2\psi$ plot.

An example of a $\sin^2\psi$ plot of the Nb films is shown in Fig. 2.13 for a 20 nm thick Nb film on sputter cleaned Si_3N_4 substrate. The negative slope indicates a compressive residual stress. This was likewise observed for the other films. Although the intensity of the 110 reflection, $I^{110}(\psi)$ (dotted line in Fig. 13) is concentrated around the poles at $\sin^2\psi = 0$ and 0.75, it was possible to measure d^{110} also in between (c.f. Fig. 2.12), thus obtaining a continuous $\sin^2\psi$ plot even for the very thin 20 nm Nb layer. It was not possible to evaluate the stress state for the 5 nm thick Nb films on uncleaned substrates due to insufficient diffracted intensity.

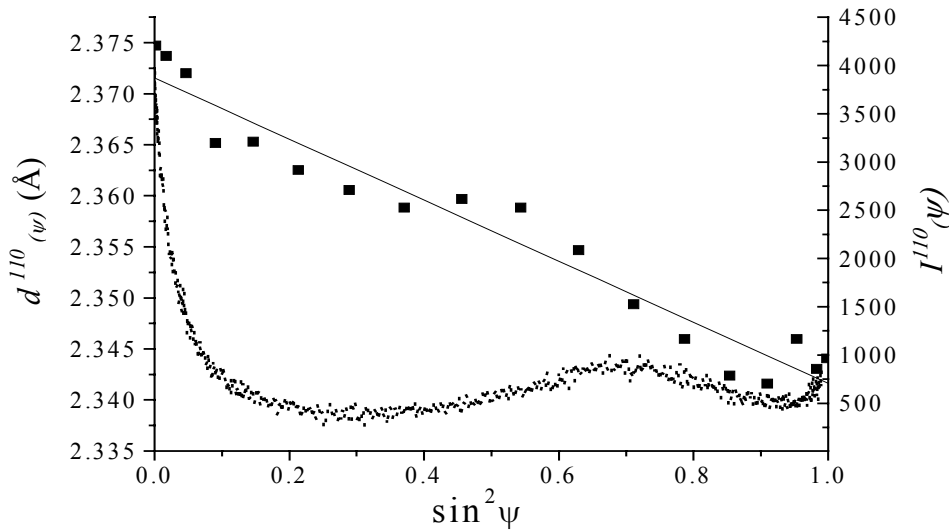


Figure 2.13. Plot of d_{ψ}^{110} versus $\sin^2 \psi$ for a 20 nm thick Nb film deposited on uncleaned Si_3N_4 substrate (■ , left hand scale), linear fit (—) and intensity I_{ψ}^{110} for the 110 reflection (..... , right hand scale).

The residual stress $\sigma_{//,r}$, is the sum of the intrinsic stress $\sigma_{//,i}$ and the extrinsic stress (for this study only the thermal stress $\sigma_{//,th}$, generated upon cooling from the layer production temperature, due to the difference in the film and substrate thermal expansion coefficients):

$$\sigma_{//,r} = \sigma_{//,i} + \sigma_{//,th} . \quad (2.3)$$

In the absence of stress relaxation by plastic deformation, the thermally induced stress can be calculated from:

$$\sigma_{//,th} = \frac{E}{1-\nu} (\alpha_f - \alpha_s) (T_d - T_a) , \quad (2.4)$$

$E/(1-\nu)$, is the texture state dependent biaxial modulus. The Neerfeld-Hill average [34] calculated for the biaxial modulus of a perfect Nb {110} fibre texture is 139 GPa. α_f and α_s are the coefficients of thermal expansion for the film ($7.3 \times 10^{-6}/\text{K}$ for Nb [36]) and the substrate ($1.72 \times 10^{-6}/\text{K}$ for Si, extrapolated for $T_d = 373 \text{ K}$ [37]), respectively. T_d (100 °C) and T_a (25 °C) are the substrate temperature during deposition and the ambient temperature during the stress measurement, respectively. The tensile thermal stress was thus calculated to be $\sigma_{//,th} = 60 \text{ MPa}$.

The compressive intrinsic stress $\sigma_{//,i}$ for the Nb layers determined from $\sigma_{//,r}$ and $\sigma_{//,th}$ using Eq. 2.3 has been plotted versus the film thickness in Fig. 2.14 for the two substrate types. In both film systems the intrinsic stress $\sigma_{//,i}$ is generally higher for the films deposited onto cleaned substrates.

A comparison of $\sigma_{//,i}$ for the layers on the different substrates shows that in the case of the uncleaned substrates the intrinsic stress in the films on SiO_2 and on Si_3N_4 is the same whereas for the films deposited on sputter cleaned substrates the growth stress is generally higher for the films on Si_3N_4 substrates.

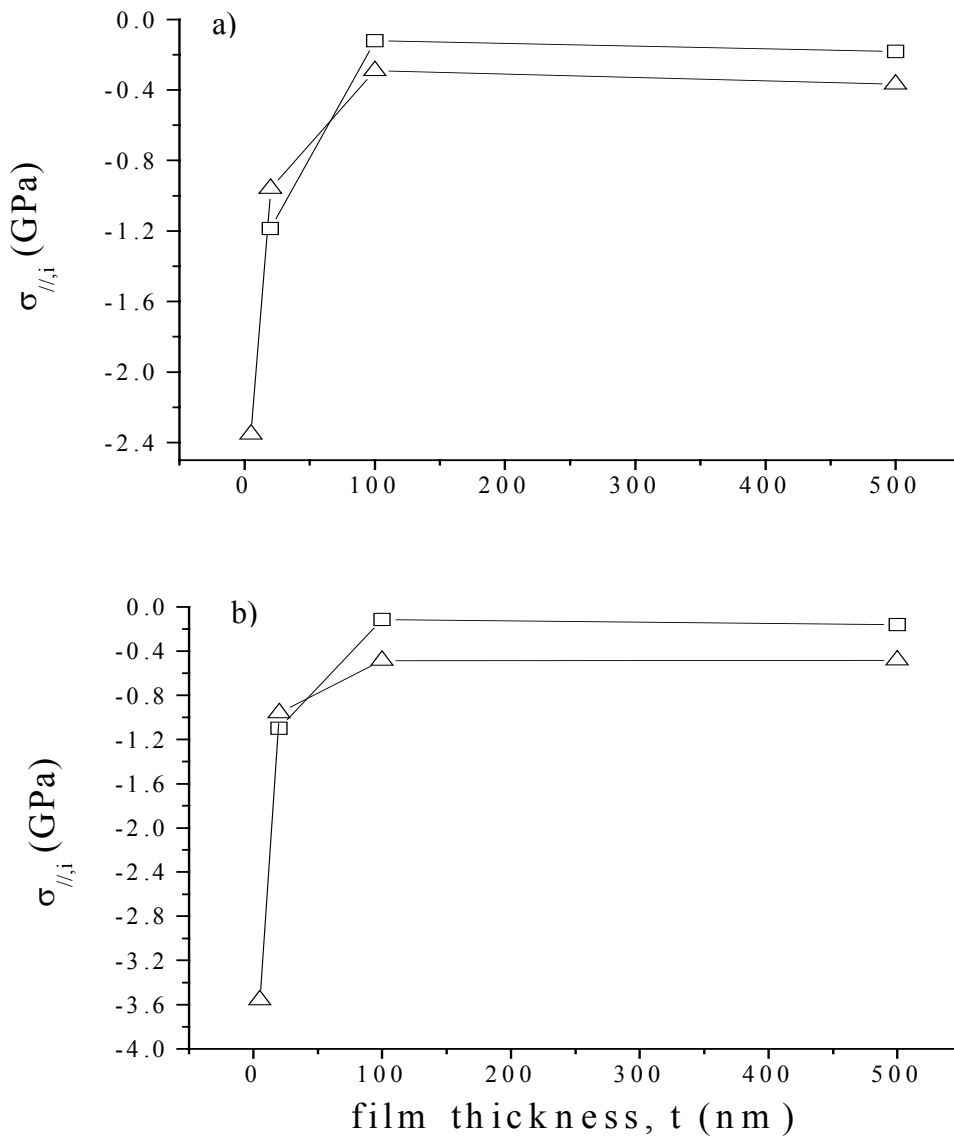


Figure 2.14. Intrinsic stress $\sigma_{//,i}$ for Nb films on uncleaned \square and sputter cleaned \triangle substrates for (a) SiO_2 substrate, (b) Si_3N_4 substrate, as a function of film thickness.

In the ultrathin (5 nm) films on the cleaned substrates a very high compressive stress occurs, of the order of a few GPa, and yet the film integrity is sustained (yield stress of bulk Nb is 207 MPa [79]). This signifies that ultra thin Nb films are mechanically much more stable than bulk Nb.

The thickness increase from 5 to 20 nm is accompanied by a drastic decrease in $|\sigma_{//i}|$ and a further increase in film thickness from 20 to 100 nm led to a further (less pronounced) decrease in $|\sigma_{//i}|$. The stress remained unchanged at film thicknesses of 100 and 500 nm.

A strain model proposed in Ref. [61] for compressive stresses in non-metallic thin films has been adopted in Ref. [50] to explain the origin of compressive stresses observed in evaporated Nb films. It is suggested that, upon exposure of Nb thin films to ambient, Nb_2O_5 oxide forms, but that also diffusion of oxygen into the metal layer through grain boundaries takes place leading to the development of niobium oxides at the grain boundaries, as illustrated in Fig. 2.15. The region of the film where these oxides are formed tends to expand, which is counteracted by the layer/substrate underneath, provided that coherency of the system is maintained. As a result compressive stress develops, in the region of the film containing these grain-boundary oxides.

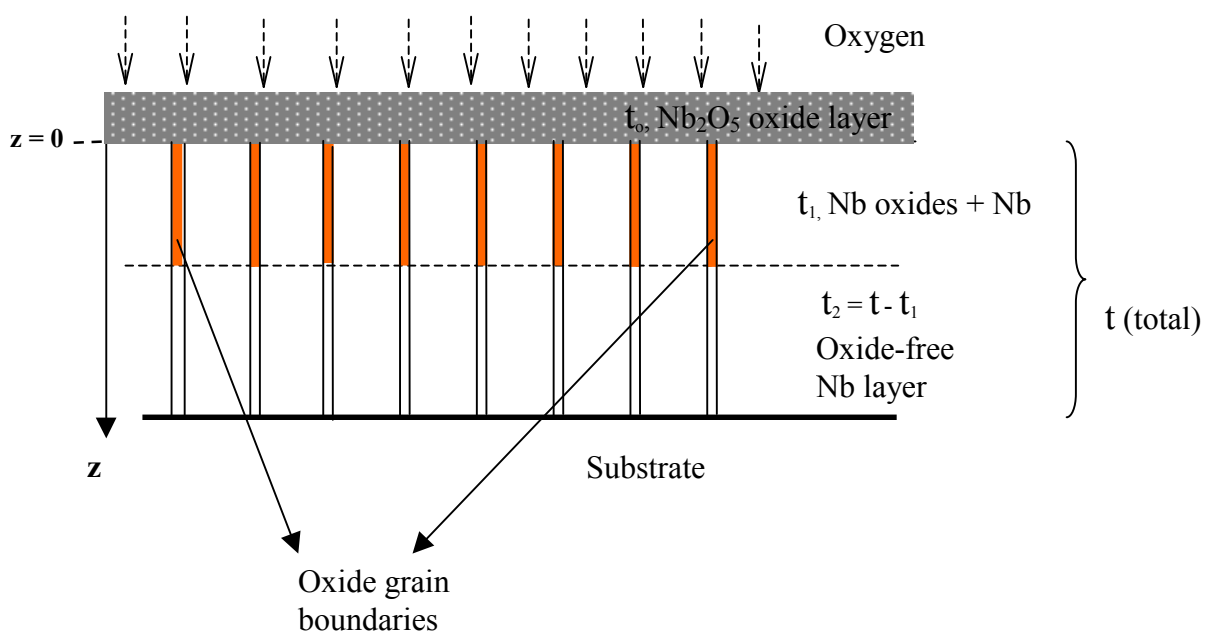


Figure 2.15. A schematic diagram for oxygen-niobium interaction based on the diffusion of oxygen through grain boundaries leading to the development of compressive stresses.

Note that the present XPS results (c.f. section 3.1) did reveal the existence of a region (beneath the Nb₂O₅ oxide top layer) where oxygen is incorporated in the Nb film.

A prerequisite for the generation of compressive stresses according to the model discussed is the presence of a columnar grain structure within the film: i.e. the grain boundaries in the surface adjacent region of the film should be largely perpendicular to the surface. This is the case here (see section 3.1.1).

The dependence of the measured intrinsic stress $\sigma_{//,i}$ on the film thickness t can be understood as follows. The Nb films are composed of two regions with different stress states: a thin oxygen containing layer t_1 of identical thickness for all the films with a high compressive stress σ_1 and an oxygen-free layer underneath of thickness $t_2 = t - t_1$, different for the various Nb films, with a small compressive stress σ_2 . The measured stress thus is an absorption-weighted average over the film thickness according to:

$$\sigma_{//,r} = \int_0^t \sigma_{//,r}(z) \exp\left[-\frac{2\mu}{\sin\theta} z\right] dz / \int_0^t \exp\left[-\frac{2\mu}{\sin\theta} z\right] dz \quad (2.5)$$

where z is the depth from the film surface and $\mu = 0.132/\mu\text{m}$ is the linear absorption coefficient of Nb for Cu K α . (In the present case $\sigma(z) = \sigma_1$ for $0 < z < t_1$ and $\sigma(z) = \sigma_2$ for $t_1 < z < t_1 + t_2$).

Adopting the measured values of $\sigma_{//,r}$ obtained for the Nb films deposited onto sputter cleaned Si₃N₄ substrates as representative of the system under investigation, the stress σ_1 in the region t_1 is taken to be equal to that obtained for the 5 nm thick film. The stress σ_2 is practically given by the measured values for the 500 nm thick film. For the other thicknesses, 20 nm and 100 nm σ then is calculated using Eq. 2.5. The result obtained using this recipe is shown in Fig. 16 for the intrinsic stress $\sigma_{//,i}$ (i.e. after subtraction of $\sigma_{//,th}$ according to Eq. 2.3). Obviously a good agreement exists between the measured intrinsic stresses and the calculated ones at the given film thicknesses, thereby validating the strain (profile) model proposed here.

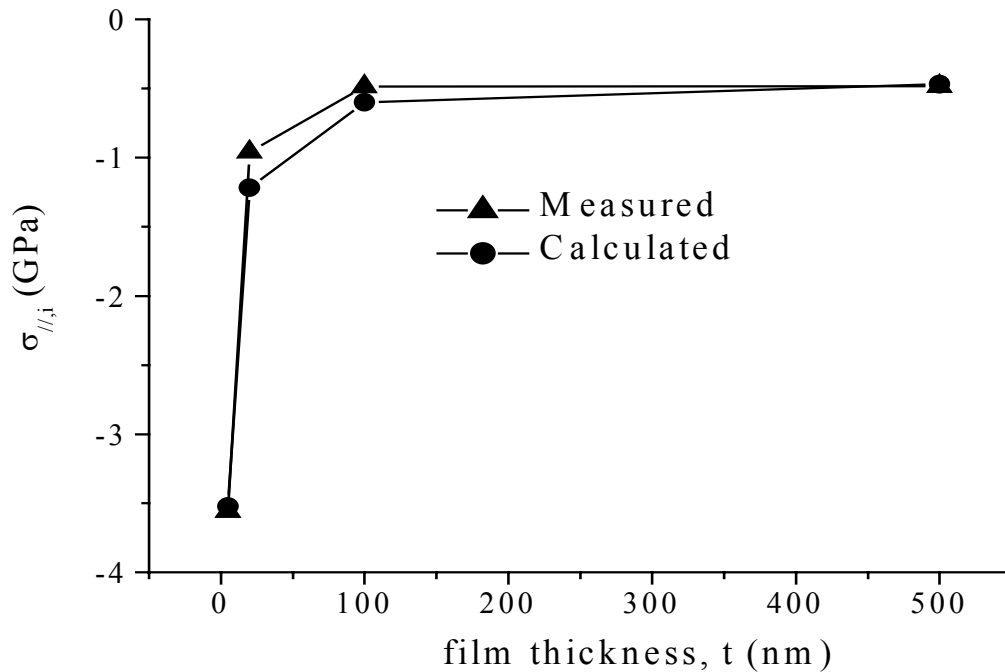


Figure 2.16. Intrinsic stress against thickness of Nb films on cleaned Si_3N_4 substrates for the as-measured stress \blacktriangle and calculated stress \bullet (see text).

The moderate compressive intrinsic stress $\sigma_{//i}$ in the oxygen free part of the Nb films (part of thickness t_2) is thought to be present in the films already before exposure to air. The possible source of such a compressive intrinsic stress is atomic peening during sputtering [9, 42]. Further it is noted that the increase of $\sigma_{//i}$ upon sputter cleaning of the substrate, being larger for the films on Si_3N_4 than for films on SiO_2 , correlates with the trends observed for the sharpness of the $\{110\}$ fibre texture (section 3.3). Grain boundaries in columnar films containing free volume would give rise to a tensile stress component acting across the grain boundaries [9]. This suggests that lower values for the compressive stress in the films with less perfect $\{110\}$ fibre texture, are due to grain boundaries of more open structure in the less textured films.

3.4.2 Grazing Incidence X-ray Diffraction (GIXRD)

In this subsection the focus is on a more detailed analysis of the stress-depth profile in the films using dedicated X-ray diffraction techniques.

For the detection of a depth profile of the stress it is necessary to measure the peak position at fixed inclination ψ of the lattice planes with respect to the specimen surface for different effective penetration depths of the X-ray beam. Small penetration depths are achieved by the so-called grazing incidence X-ray diffraction (GIXRD) technique where small angles of incidence of the X-ray beam, α (and/or small angles of exit, β : see Fig. 2.1), are used. In the case of conventional $\theta/2\theta$ diffraction, the effective penetration depth, τ , of Cu $K\alpha$ radiation is much larger than the thickness of the Nb films. With the Bragg-Brentano geometry the Bragg angle of the 110 reflection, $2\theta = 38.5^\circ$ corresponds to a penetration depth of $\tau = 1.2 \mu\text{m}$ (1/e definition). Hence GIXRD with the present Nb films is hardly possible applying this geometry. In order to confine the beam to a depth, τ , of for instance, 10 nm, an angle of incidence $\alpha = 0.15^\circ$ is required, which is smaller than the critical angle for total reflection: $\alpha_c = 0.4^\circ$ (in this case). Furthermore, the angle of divergence, α_D , of the beam on the MRD apparatus (c.f. section 2.5) is 0.3° .

Yet an attempt has been made to perform measurements at a small and fixed penetration depth τ . Then, get a sufficient number of points in a $\sin^2\psi$ plot, the so-called hkl- χ - Ω mode has been adopted here. This means that the lattice spacing of different hkl, each measured at different ψ , are incorporated in a single analysis. The constraint of fixed penetration depth and the need to hit the poles corresponding to the {110} fibre texture are fulfilled by selecting appropriate χ - Ω pairs.

Conventional $\sin^2\psi$ measurement

First, a conventional measurement ($\Omega = 0$) was carried out without using grazing incidence with the aim to ascertain that incorporating results from different hkl reflections in a single $\sin^2\psi$ plot does not affect the stress analysis, provided that all pairs of hkl and ψ belong to the same crystallite group. A crystallite group is defined as the family of crystals belonging to the same texture component [34] (in this case the group of crystals with the 110 plane parallel to the surface).

The hkl poles (i.e. corresponding ψ values) for the 110 crystal group were calculated and the corresponding lattice spacing measurements were performed for a 500 nm thick Nb film deposited onto a sputter cleaned SiO_2 substrate. The resulting $\sin^2\psi$ plot is shown in Fig. 2.17. The

strain, ε , was calculated from the measured d_ψ values using the strain free lattice spacing, d_0 (see data in Ref. [80]), following Eq. 2.2. The result indicates that the data for all hkl lie on a straight line. Hence the incorporation of the hkl's in a single analysis is feasible.

The residual stress was calculated according to Eq. 2.2, replacing the X-ray elastic constant $\frac{1}{2}S_2^{hkl}$ with the mechanical elastic constant $(1+\nu)/E$, where ν is the Poisson ratio given by 0.397 and E is the Young's Modulus given by 104.9 GPa [78]) assuming isotropic elastic behaviour of the film. The calculated stress from the plot was -370 MPa. The corresponding intrinsic stress $\sigma_{//,i} = -430$ MPa (c.f. Eq. 2.3) which can be compared with $\sigma_{//,i} = -370$ MPa obtained from measurements using only the 110 reflection in section 3.4.1. The difference can be ascribed to the assumption used in calculating the elastic constants.

In the conventional method (i.e. at $\Omega=0$, $\psi = \chi$) the penetration depth τ for the X-rays is much larger than the film thickness of 500 nm. Hence the stress value obtained here represents an average value over the film thickness.

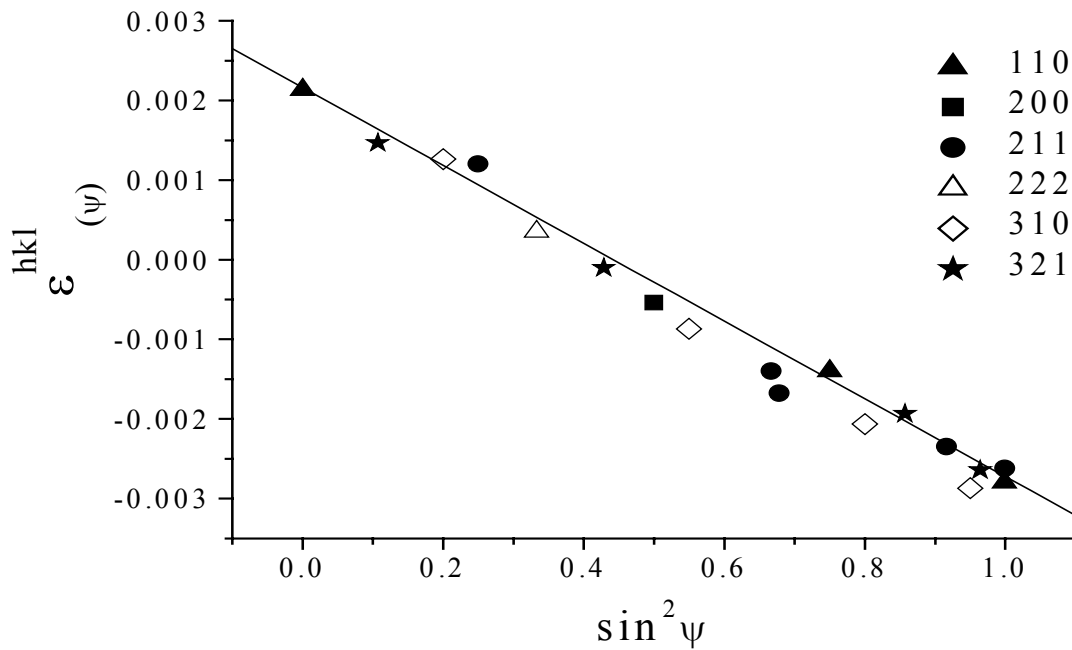


Figure 2.17. $\sin^2 \psi$ plot for a 500 nm thick Nb film for different hkl with ψ poles taken for the 110 crystal group. Conventional measurement: $\Omega=0$, $\psi = \chi$.

Grazing Incidence Method

For application of GIXRD according to the $hkl\text{-}\chi\text{-}\Omega$ -mode, $hkl\text{-}\chi\text{-}\Omega$ combinations were now chosen such that the penetration depth was kept fixed at $\tau = 40$ nm (corresponding to small angles of incidence, α , and/or of exit, β). In case of small angles (α and β) between the X-ray beam and the sample surface, the effect of refraction has to be considered which leads to an increase of the measured diffraction angle 2θ of a hkl reflection [81] and thus to an error of the resulting lattice spacing, d . To overcome this problem as an additional constraint, those $hkl\text{-}\chi\text{-}\Omega$ combinations were selected for which the theoretical shift of 2θ due to the refraction effect was $2\theta_r < 0.01^\circ$ (and about the same for all combinations). Finally the range $60^\circ \leq \psi < 90^\circ$ could be covered in the stress analysis.

The resulting $\sin^2\psi$ plot is shown in Fig. 2.18. From the slope of the straight line, the stress was calculated as -510 MPa. Clearly this value is greater than the value obtained by the conventional method above: -370 MPa. Note that the use of the same tilt angle range of $60^\circ \leq \psi < 90^\circ$ in the conventional method outlined above yielded a stress value of -380 MPa which is similar to that obtained for the full range $0^\circ \leq \psi < 90^\circ$ above -370 MPa. This shows that the difference in stress values between the conventional method (Fig. 2.17) and the GIXRD $hkl\text{-}\chi\text{-}\Omega$ -mode (Fig. 2.18) is not due to the different ψ ranges, but an indication of a variation of the stress with the depth, in agreement with the analysis in section 3.4.1.

It can be concluded that using the GIXRD results confirm that there exists a range with high compressive stress in the surface region of the films. Note that the information depth in the GIXRD measurement performed here, of about 40 nm, is still large as compared to the extent of the oxygen containing surface layer of some nm (c.f. section 3.4.1).

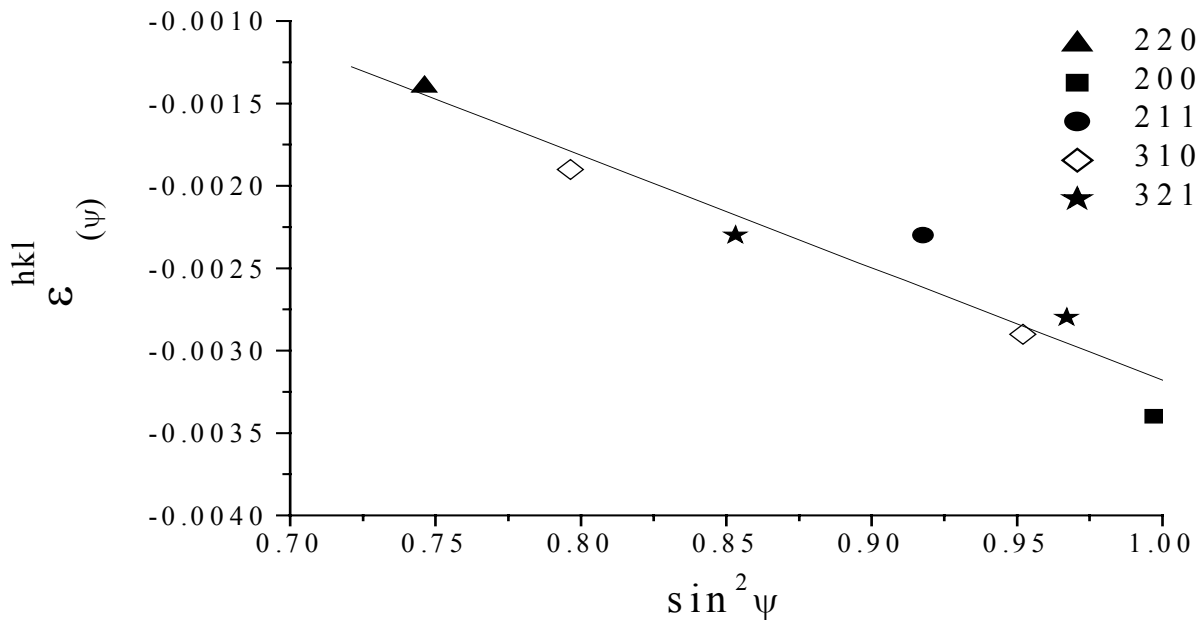


Figure 2.18. $\sin^2\psi$ plot for 500 nm thick Nb film deposited on sputter cleaned SiO_2 substrate obtained by GIXRD measurement according to the hkl - χ - Ω -mode.

3.4.3 Aging effect

The oxidation of the Nb layer may progress with time of aging. The intrinsic stress for the samples investigated have been plotted in Figs. 2.19 and 2.20 for the times 1 week and 4 months of storage at room temperature in air. Apparently, aging affects the stress (see in particular Fig. 2.19a and Fig. 2.20b), indicating that the mechanism responsible for the generation of stress by oxygen uptake at the boundaries was still going on after 1 week. The aging effect is not observed for larger film thicknesses because the measured stress value is an average over the sampled volume: the larger the value of t_2 , the lesser the stress contribution from t_1 (see section 3.4.1).

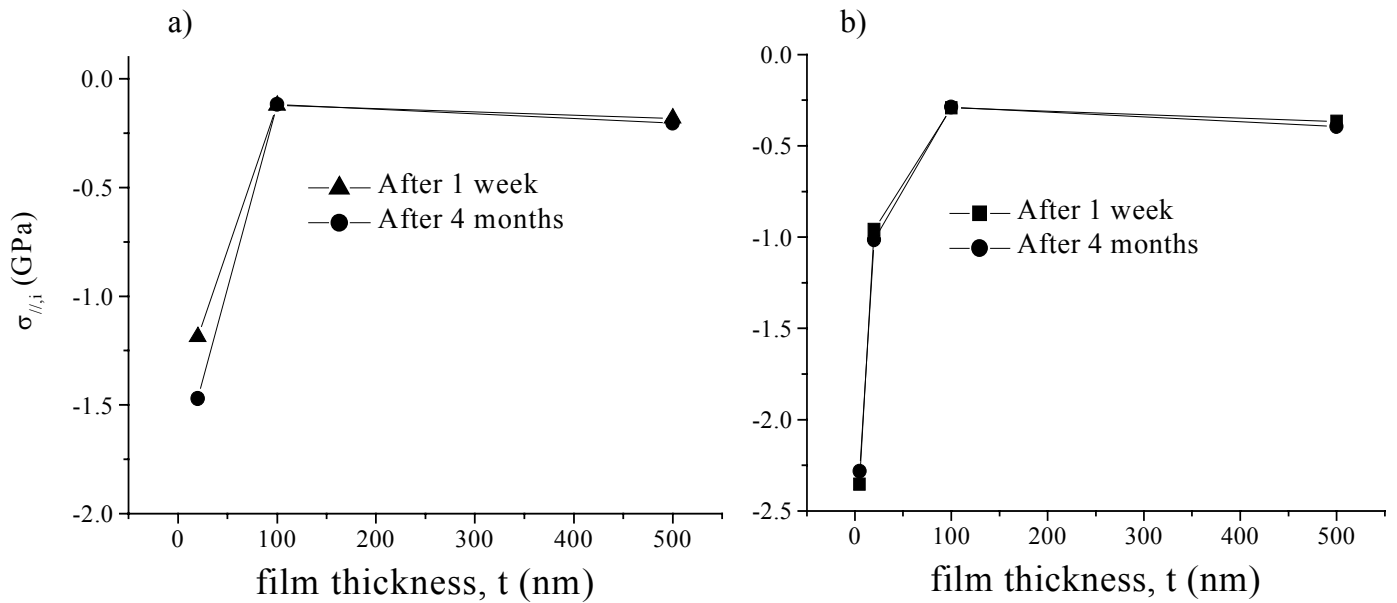


Figure 2.19. Graph of intrinsic stress versus film thickness for Nb films measured 1 week and 4 months after deposition for (a) uncleaned, (b) sputter cleaned SiO_2 substrates.

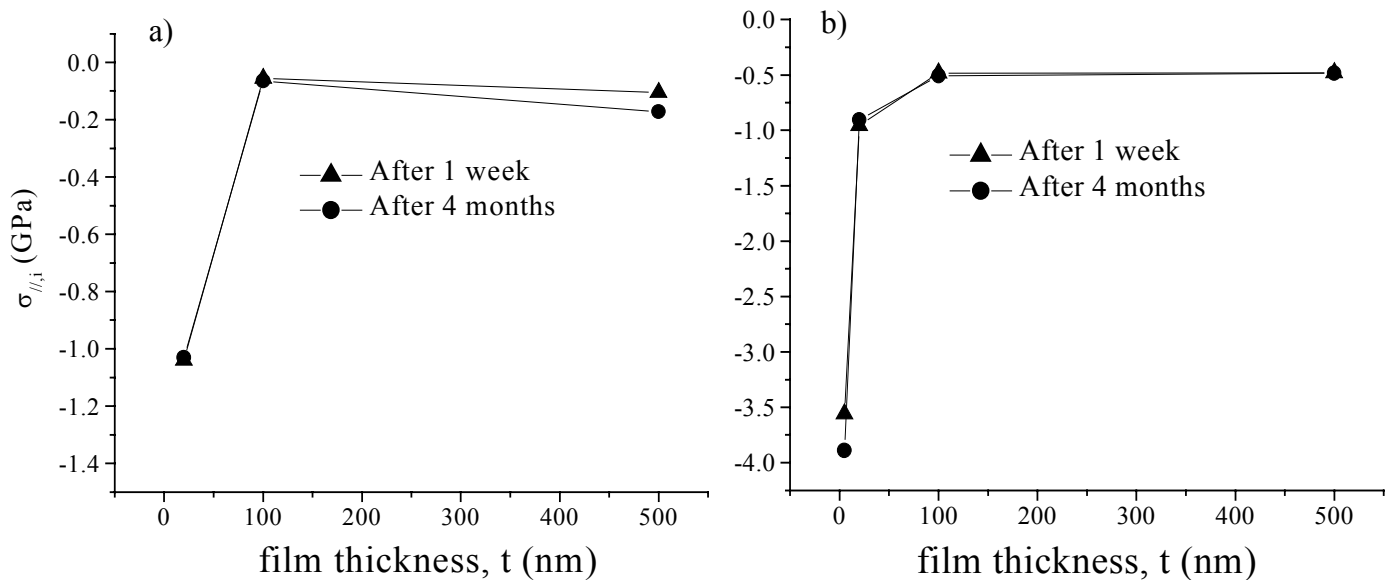


Figure 2.20. Graph of intrinsic stress versus film thickness for Nb films measured 1 week and 4 months after deposition for (a) uncleaned, (b) sputter cleaned Si_3N_4 substrates.

Similar stress measurements were performed for a number of the Nb specimens after 6 months of aging. Further stress changes were not observed, suggesting that a saturation level of oxygen uptake had been reached in the surface adjacent region of the Nb films.

3.5 Microstrain

From diffraction-line broadening analysis the crystal imperfection, i.e. the crystallite size and the microstrain, can be determined [82]. Using $\theta/2\theta$ scans in Bragg-Brentano geometry for the line-broadening analysis, the crystallite size and the microstrain values pertain to the direction perpendicular to the film surface.

Here the Williamson and Hall (integral breadth) method [45] was applied to the 110 and 220 reflections of the 100 nm and 500 nm thick films using the integral width (= peak area/peak height) as determined by fitting a pseudo-Voigt function to the measured line profiles. For the thinner 5 nm and 20 nm thick films the intensity of the 220 reflection was too low for a reliable analysis.

The integral width resulting from only the physical broadening, β_f , was obtained by correcting the measured integral width, β_h , for the instrumental integral width, β_g , according to (recognizing that the peaks are close to Gaussian):

$$\beta_f = \sqrt{\beta_h^2 - \beta_g^2}, \quad (2.6)$$

Values for β_g was determined from a measurement of a standard NIST Si specimen and interpolation at the 2θ values of the Nb 110 and 220 reflections.

In a (classical) W-H plot the integral breadth in reciprocal space, $\beta_f \cos\theta/\lambda$, is plotted against the reciprocal lattice spacing, $\beta_f 2\sin\theta/\lambda$. The crystallite size and the microstrain are obtained from the intercept and the slope respectively of a straight line fitted to the measured points [82]. In the present case the intercepts of the lines through the two points in the W-H plots were zero within the experimental accuracy, i.e. the corresponding crystallite size is larger than detectable by XRD line-profile analysis (i.e. larger than, say, 150 nm). This result is compatible with the columnar microstructure of the films (see section 3.2).

The values for the microstrain ε^{110} , obtained from the slope of the lines in the W-H plots, are represented in Fig. 2.21. In the Nb films microstrain occurs with average values of the order of one tenth of a percent. Systematic trends are observed: (i) the microstrain decreases with increasing

thickness of the films, (ii) the microstrain is smaller for the films on Si_3N_4 than on SiO_2 and (iii) the microstrain is smaller for the films on cleaned substrates than on uncleaned substrates. This microstrain behaviour correlates very well with the behaviour of the sharpness of the $\{110\}$ texture of the Nb films (see section 3.3): a sharper texture is associated with a lower microstrain. Apparently, the fluctuations of the lattice parameter d^{110} (perpendicular to the film surface) are larger when the orientation of the 110 lattice planes of the grains exhibits a larger deviation from perfect alignment parallel to the film surface.

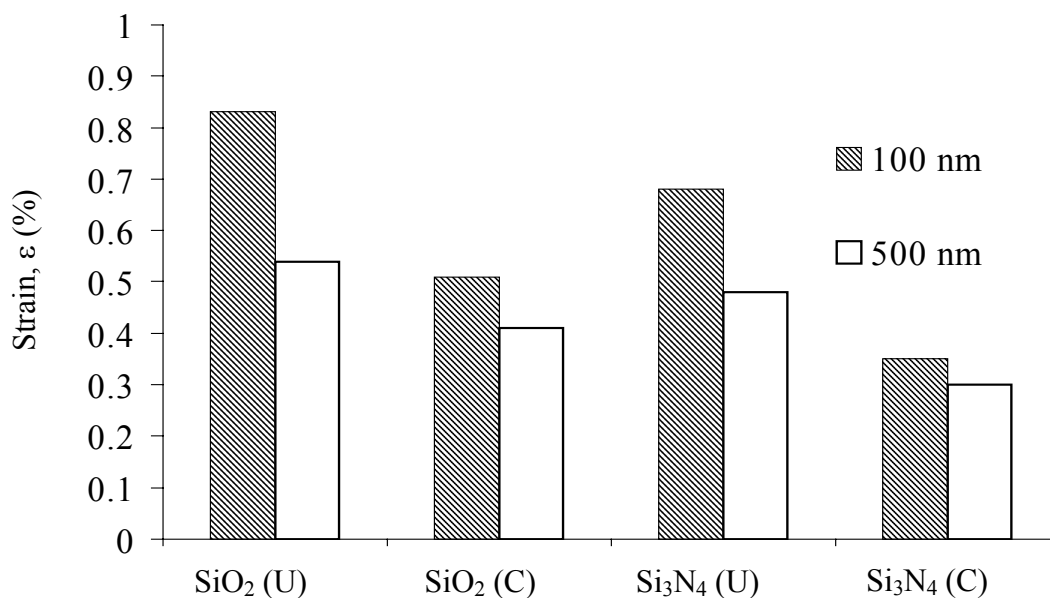


Figure 2.21. Microstrain ε as a function of substrate sputter cleaning condition (uncleaned (U) and sputter cleaned (C)), type of substrate; (SiO_2 and Si_3N_4) and film thickness.

3.6 X-ray reflectometry

The X-ray reflectivity curves for the Nb films on sputter cleaned SiO₂ substrates are shown in Fig. 2.22. For an angle of incidence smaller than the critical angle, α_c , total reflection occurs of X-rays incident on a surface.

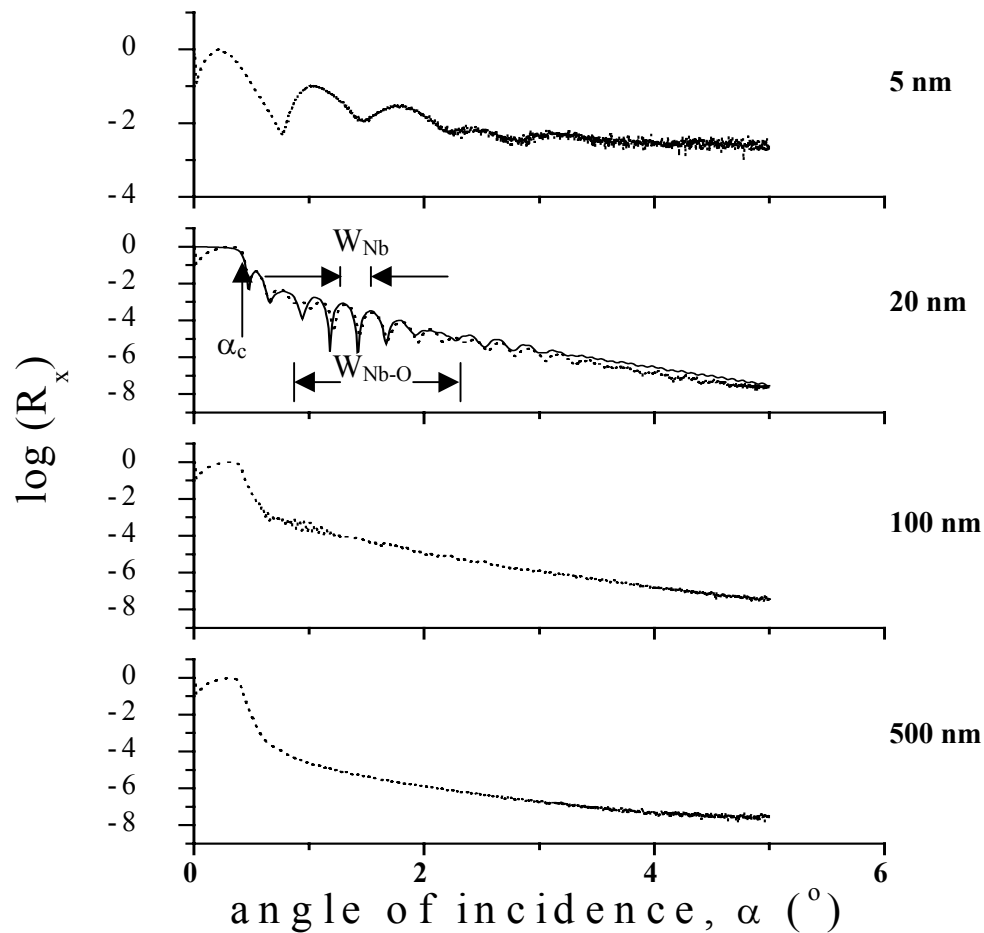


Figure 2.22. X-ray reflectivity R_x for Nb films on sputter cleaned SiO₂. (.....) measured, (—) fit. α_c is the critical angle for total reflection, W denotes the period of oscillation.

For the 20 nm thick film also a simulated curve obtained using commercial fitting software WIN-REFSIM (Bruker AXS/ Siemens) [83] has been presented in Fig. 2.22, which had been obtained using the criterion of best least squares fit to the experimental data. A good fit was only possible if an oxide layer on top of the Nb film was incorporated in the model of the layer substrate.

The parameters resulting from the fit have been listed in Table 2.2. Although the fit is not perfect, the main features are well described: the oscillations with period W_{Nb} associated with the Nb metal

layer thickness ($t = 16.1$ nm) are superimposed by a period from the Nb-O layer ($t = 3.2$ nm), as indicated by the width $W_{\text{Nb-O}}$ in Fig. 2.22 (the amplitude of the oscillations shows minima at $\alpha \sim 0.8^\circ$ and $\alpha \sim 2.2^\circ$). The critical angle of total reflection, $\alpha_c = 0.39^\circ$, as obtained from the drop of the reflectivity as indicated for the 20 nm thick Nb film in Fig. 2.22 is smaller than that for pure Nb ($\alpha_c = 0.44^\circ$). The thickness of the niobium-oxide layer, $t = 3.2$ nm, corresponds well with the results obtained from the XPS analysis (section 3.1).

Table 2.2. Parameters for simulation of 20 nm thick Nb film deposited on cleaned SiO_2 substrate. t: thickness, R: surface roughness, ρ : mass density.

	t (nm)	R (nm)	ρ (g/cm ³)
Niobiumoxide	3.2	0.53	3.43
Nb	16.1	0.55	8.55
SiO_2	50.5	0.27	2.20
Si	-	0.21	2.33

4 Conclusions

4.1 Chemical composition

- A layer of Nb₂O₅ with thickness of about 3 nm forms at ambient on the surface of Nb thin films after sputter deposition, irrespective of the film thickness.
- The presence of oxygen at depths beyond 3 nm is likely due to Nb-oxide at grain boundaries.

4.2 Morphology

- Nb films sputter deposited onto amorphous SiO₂ or amorphous Si₃N₄ exhibit columnar microstructure.
- The lateral grain size of thin films can be well quantified using a height auto-correlation function analysis.
- The lateral grain size in thickening Nb films below 100 nm thickness is the same as the island size in 5 nm thick Nb films at the coalescence stage, indicating that grain boundaries in growing Nb films remain immobile between 5 nm and 100 nm film thickness. Lateral grain growth in Nb films begins at 100 nm film thickness.
- The lateral grain sizes of Nb films are of nano-scale (≤ 100 nm).
- Columnar microstructures in Nb films deposited at 100 °C become clear at a thickness of 20 nm and are fully established at 100 nm.
- Stress related extrusions/protrusions are present in Nb films deposited onto Si₃N₄ even at 5 nm.
- The surface roughness of Nb films is larger at larger film thickness.

4.3 Texture

- Nb films sputter deposited at 100 °C have only one texture component (apart from a twinning induced component), a Nb {110} fibre texture (no random component occurs).
- Twinning on 211 planes of the {110} oriented grains in Nb films is detectable at larger film thicknesses.
- Texture development of Nb films starts at a thickness of about 5 nm. The texture generally becomes sharper with increasing film thickness.

- The texture of Nb films deposited onto amorphous Si_3N_4 substrates is sharper than for films deposited onto amorphous SiO_2 substrates. For both types of substrates the texture becomes sharper when the substrate is cleaned before film deposition. This is explained by the stronger chemical interaction between Nb and oxygen (in particular that oxygen which is adsorbed at the uncleaned substrate surface), as compared to that between Nb and nitrogen.

4.4 *Stress and microstrain*

- A rotational symmetric compressive state of plane (residual) stress occurs in Nb ultrathin and thin films grown by sputter deposition onto amorphous substrates.
- The contribution of the thermal stress (for Nb films produced at 100 °C) to the residual stress is relatively small.
- Nb-oxide formation at Nb film grain boundaries below a Nb_2O_5 surface layer is responsible for the occurrence of a strong compressive stress, of about 3 GPa, within a depth range of a few nanometers. Below this depth in the thicker films a compressive intrinsic stress of about 400 MPa occurs, which is ascribed to atomic peening. Thus a large stress gradient is present in the thicker films.
- For films with less sharp $\{110\}$ fibre texture the observed compressive intrinsic stress is smaller, which is ascribed to the occurrence of a tensile stress component acting across the grain boundaries in the films with less developed textures.
- Continual oxidation, upon aging at ambient, causes increase of stress up to 6 months of aging.
- For the films exhibiting a less sharp $\{110\}$ fibre texture a higher microstrain (as deduced from the diffraction line-broadening analysis) occurs, indicating that the fluctuations of the strain (microstrain) in the stressed crystallites are larger when the crystallites are less perfectly aligned according to the $\{110\}$ fibre texture.

Kapitel 3. Kurzfassung der Dissertation in deutscher Sprache

1. Einleitung

Dünne Filme werden in vielen technischen Bereichen angewendet. Aktuelle Entwicklungsarbeit ist z.B. auf ihren Einsatz in mikro-elektromechanischen (MEMS) und nano-electromechanischen (NEMS) Anwendungen gerichtet. Die zunehmenden Forschungsaktivitäten, die auf das Verständnis der Eigenschaften von dünnen Filmen gerichtet sind, haben zur Entwicklung von verbesserten und neuen analytischen Methoden geführt. Die Mikrostruktur, d.h. die Morphologie und die kristallografische Textur, und besonders die inneren Spannungen sind Eigenschaften, die für das Verhalten von dünnen Filmen in technischen Anwendungen wichtig sind. Die systematische Untersuchung der Zusammenhänge zwischen diesen Eigenschaften und deren Abhängigkeit von den Herstellungsbedingungen ist Gegenstand aktueller Forschung.

Für den Zusammenhang zwischen der Morphologie (Kornstruktur) und den Herstellungsbedingungen (Temperatur und Druck des Sputtergases) von gesputterten Metallschichten (im Dickenbereich von 20 μm bis 250 μm) liegt in der Literatur ein idealisiertes Struktur-Zonen-Modell vor. Jedoch ist über den Einfluß der Art und der Beschaffenheit des Substrates auf die Morphologie, besonders von sehr dünnen Metallfilmen, noch wenig bekannt.

Dünne PVD Schichten weisen oft eine ausgeprägte kristallografische Fasertextur auf. Aus der Betrachtung der Oberflächenenergien wurde in der Literatur gezeigt, warum bei Filmen aus fcc Metallen bevorzugt eine $\{111\}$ Textur vorliegt, während bcc Metalle meistens eine $\{110\}$ Textur ausbilden. Die Details solcher Texturen, d.h. deren Stärke (gemessen am Vorliegen von Komponenten mit anderer kristallografischer Orientierung) und deren Schärfe (gemessen am Bereich der Verkippung der Kristallite gegenüber der idealen Richtung), können von den Herstellungsparametern abhängen und somit gezielt beeinflusst werden. Auch hier ist über den Einfluß des Substrates noch wenig bekannt.

Innere Spannungen in dünnen Schichten entstehen während des Wachstums und unter Umständen während des Abkühlprozesses von der Herstellungstemperatur auf Raumtemperatur. Für die Entstehung von Wachstumsspannungen (im Zug- oder Druckbereich) werden in der Literatur verschiedene Mechanismen angeführt, wie der Einbau von Atomen des Sputtergases, der sogenannte "atomic peening" Effekt und interatomare Kräfte im Anfangsstadium des zwischen den Inseln und während des Wachstums über die Korngrenzen hinweg. In Metallschichten, die nach Herstellung der Umgebung ausgesetzt werden, können durch Reaktion mit dieser (z.B. durch

Einbau von Sauerstoff) innere Spannungen aufgebaut werden. Hier ist der Kenntnisstand noch nicht sehr tief.

Das Ziel der vorliegenden Arbeit war die systematische Untersuchung der Mikrostruktur, der Textur und der inneren (Makro- und Mikro)-Spannungen in dünnen Metallschichten, die durch Magnetronspütern hergestellt wurden. Insbesondere Zusammenhänge zwischen diesen Eigenschaften sollten studiert werden. Als repräsentative Systeme wurden ein fcc Metall (Kupfer) und ein bcc Metall (Niob) ausgewählt. Um möglichst umfangreiche Informationen zu erhalten, wurde eine breite Palette verschiedener Untersuchungsmethoden eingesetzt. Einflüsse der Art und der Vorbehandlung des Substrates auf die Eigenschaften der darauf abgeschiedenen Schichten mit sehr unterschiedlicher Dicke (angefangen von 5 nm dicken Schichten) waren ein Schwerpunkt der Arbeit. Dazu wurden zwei Substrattypen, amorphes SiO₂ und amorphes Si₃N₄, sowohl im unbehandelten Zustand, als auch nach Reinigung mit Ar Ionen, ausgewählt. Die erarbeiteten Ergebnisse sollen einen Beitrag liefern zur Vorhersage und der gezielten Einstellung der Eigenschaften von dünnen gesputterten Metallfilmen.

2. Experimentelle Grundlagen

2.1 Probenherstellung

Kupfer- und Niobfilme mit verschiedener Dicke von 5 nm bis 1000 nm wurden durch Magnetronspütern auf zwei kommerziell erhältlichen Si Wafern hergestellt, die mit einer amorphen Deckschicht versehen waren: 500 µm Si(510)/ SiO₂ (amorph) und 500 µm Si(100)/ SiO₂ (amorph)/ Si₃N₄ (amorph). Neben den unbehandelten Substraten wurden auch Substrate verwendet, die in-situ durch Spütern mit Argonionen gereinigt wurden.

2.2 Untersuchungsmethoden

Die Morphologie der Filme wurde untersucht mittels Transmissionselektronenmikroskopie (TEM), Focussed Ion Beam (FIB) imaging und Atomic Force Microscopy (AFM). Mit X-ray Photoelectron Spectroscopy (XPS) wurde die chemische Zusammensetzung and der Oberfläche der Substrate und der Cu Filme und im Fall der Nb Filme auch deren Tiefenprofile bestimmt. Mit den

Methoden der Röntgendiffraktometrie wurden die kristallografische Textur, die Eigenspannungen und die Mikrodehnungen in den Filmen ermittelt. Die Nb Filme wurden zusätzlich mittels Röntgenstrahlreflektometrie untersucht.

3. Ergebnisse für die Cu Filme

3.1 Morphologie

Die Morphologie der Cu Filme wird durch die Vorbehandlung der Substrate beeinflusst. Reinigung der Oberfläche mit Ar Ionen, bei der Sauerstoff- und Kohlenstoffkontaminationen entfernt werden, führt bei den 5 nm dicken Filmen, die sich im Zustand der Koaleszenz befinden, zu einer Verkleinerung der Größe der Inseln, entsprechend einer größeren Keimdichte. Beim Wachstum der Filme entsteht auf ungereinigten Substraten eine Mischung aus globularen und equiaxed Körnern, während sich auf gereinigten Substraten eine kolumnare Mikrostruktur mit kleineren Korngrößen bildet. Diese Einflüsse des Substratzustandes müssen in zukünftigen Struktur Zonen-Modellen berücksichtigt werden.

3.2 Textur

Es wurde gezeigt, dass für eine eingehende Aufklärung der kristallografischen Textur mit Diffraktometriemethoden die Kombination von $(\theta/2\theta)$ Scans in Bragg-Brentano Geometrie und von Polfiguren erforderlich ist: $(\theta/2\theta)$ Scans liefern Aussagen über die Stärke einer Texturkomponente (durch den Vergleich mit anderen Komponenten), während Polfiguren zusätzlich deren Schärfe ergeben. Die gesputterten Cu Schichten weisen durchwegs eine $\{111\}$ Fasertextur auf, mit geringen Anteilen von $\{200\}$ und $\{311\}$ und keine Komponente mit regelloser Orientierung. Zusätzlich tritt durch Zwillingsbildung an den $\{111\}$ Ebenen eine $\{511\}$ Texturkomponente auf, deren Volumenanteil in den Filmen auf SiO_2 größer ist als in den Filmen auf Si_3N_4 .

Die Einflüsse des Ar Gasdrucks beim Sputtern, des Substrates, der Filmdicke und nachfolgenden Temperung auf die Textur der Filme wurden eingehend untersucht. Die Schärfe der $\{111\}$ Textur von Filmen auf ungereinigten Substraten war gleich für SiO_2 und Si_3N_4 , während nach Reinigung der Oberfläche mit Ar Ionen im Fall der Si_3N_4 Substrate die Textur deutlich ausgeprägter wurde (Abb. 1).

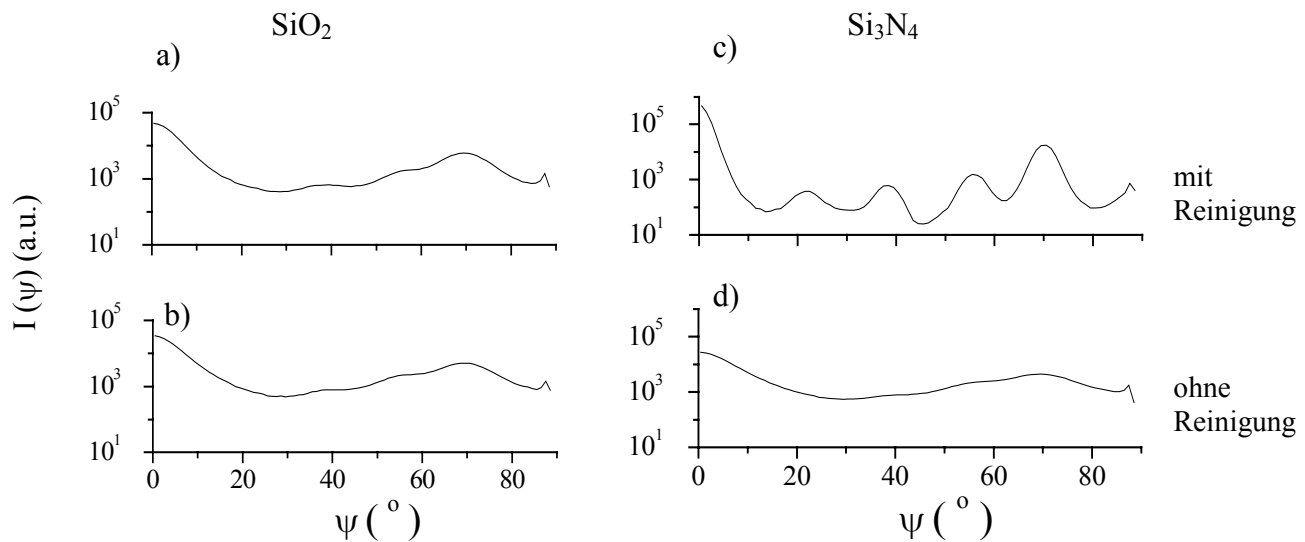


Abb. 1. Polfiguren (111 Reflex) für 500 nm dicke Cu Filme auf SiO₂ und Si₃N₄ ohne Reinigung und nach vorhergehender Reinigung des Substrates. Im Fall von Si₃N₄ führt die Reinigung (Entfernung von Sauerstoffatomen) zu einer schärferen Textur.

Dieses Verhalten wird damit erklärt, dass die Wechselwirkung der Cu Atome mit Sauerstoff auf der Substratoberfläche die Ausbildung einer perfekten Textur behindert. Der Unterschied in der Textur der Filme auf SiO₂, bzw Si₃N₄ (im gereinigten Zustand) ist größer bei den 5 nm dicken Filmen, als bei den 500 nm dicken Filmen. Dies weist darauf hin, dass der Einfluß des Substrates mit wachsender Schichtdicke abnimmt.

Nach Tempern von Filmen auf SiO₂ wurde eine Abnahme der Minoritätstexturkomponenten zugunsten der {111} Komponente beobachtet.

3.3 Eigenspannungen

Die Eigenspannungen wurden röntgenografisch mit der sogenannten $\sin^2\psi$ Methode ermittelt (s. Abb. 2 für 500 nm dicke Filme). Auf Grund der ausgeprägten {111} Fasertextur war es möglich, auch für die extrem dünnen (5 nm) Cu Schichten eine Eigenspannungsanalyse durchzuführen. In diesen Schichten treten als Wachstumsspannungen (nach Abzug der thermischen Spannungen, die während der Abkühlung von der Herstellungstemperatur von 100°C auf Raumtemperatur

entstehen) Zugspannungen in der Schichtebene auf, die von den attraktiven Kräften zwischen den Inseln im Stadium der Koaleszenz herrühren.

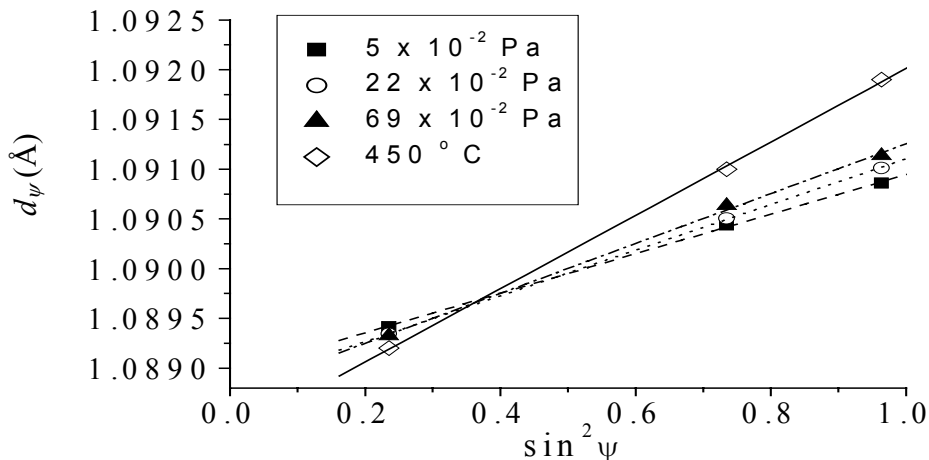


Abb. 2. $\sin^2\psi$ plots (311 Reflex) für 500 nm dicke Cu Filme auf SiO_2 (gereinigt), gesputtert bei verschiedenem Ar Gasdruck. Bei höherem Druck wird eine höhere Zugspannung gemessen, die nach Abzug der thermischen Spannung einer geringeren Druckspannung während des Wachstums entspricht. Nach Glühung liegt eine höhere Zugspannung vor.

In dickeren (500 nm) Cu Filmen wurden als Wachstumsspannungen Druckspannungen gemessen. Diese Umkehr der Spannung beim Wachstum der Filme wird erklärt durch (i) Spannungsabbau durch Diffusion von Cu Atomen (die eine relativ hohe Beweglichkeit besitzen) zu den Korngrenzen hin und (ii) Entstehung von Druckspannungen durch den „atomic peening“ Effekt. Bei 500 nm dicken Filmen auf Si_3N_4 wurde gefunden, dass die Druckspannungen im Film durch vorheriges Reinigen des Substrates verringert werden. Dies wird erklärt durch die Bildung einer kolumnaren Mikrostruktur auf gereinigten Substraten, die Anlass gibt für eine Zugspannungskomponente parallel zur Schicht auf Grund von attraktiven Kräften zwischen den Körnern.

3.4 Mikrodehnungen

Die Mikrodehnungen in den Körnern mit der $\langle 111 \rangle$ Richtung senkrecht zur Filmebene wurden aus der Linienbreite der 111 und 222 Reflexe mit der Methode nach Williamson und Hall ermittelt. Eine Linienverbreiterung durch den Kristallitgrößeneffekt wurde nicht beobachtet. Eine Tendenz wurde festgestellt, dass Schichten mit höheren Makrospannungen auch größere Mikrodehnungen aufweisen. Ein deutlicherer Zusammenhang wurde mit der Textur gefunden: Filme mit schärferer Textur wiesen größere Mikrodehnungen auf.

4. Ergebnisse für die Nb Filme

4.1 Morphologie

Die Topografie der Filmoberfläche wurde mit AFM untersucht. Die Rauigkeit der Nb Filme nimmt während des Dickenwachstums zu, wobei keine systematischen Unterschiede für die beiden Substrattypen, SiO_2 und Si_3N_4 , und kein Einfluss der Substratreinigung auftreten. Filme auf Si_3N_4 wiesen im Anfangsstadium des Dickenwachstums nach dem Stadium der Koaleszenz neben der Rauigkeit der Oberfläche zusätzliche nadelförmige Auswüchse auf, die zu einer bimodalen Höhenverteilungsfunktion führen. Für die Charakterisierung der Morphologie in lateraler Richtung wurde ein Computeralgorithmus entwickelt zur Berechnung der Höhen-Höhen Korrelationsfunktion aus den zweidimensionalen AFM Daten. Dieser Funktion konnte dann eine charakteristische Länge für die laterale Ausdehnung der Höhenfluktuationen entnommen werden, die ein Maß für die laterale Korngröße darstellt. Für beide Substrattypen nimmt diese während des Dickenwachstums der Nb Schichten zu von ca. 30 nm bis ca. 100 nm.

Die Untersuchung der Morphologie der 500 nm dicken Filme mit FIB zeigte das Vorliegen einer kolumnaren Struktur mit einer lateralen Korngröße um 130 nm, die mit den durch AFM ermittelten Werten recht gut übereinstimmt.

Insgesamt ergab sich, dass die Morphologie der Nb Schichten nicht vom Typ des Substrates und von dessen Vorbehandlung abhängt.

4.2 Tiefenprofile der chemischen Zusammensetzung

Die Tiefenprofile der Elemente Nb, Si, N, O und C wurden mit XPS während des Abtrags durch Sputtern gemessen (Abb. 3). Dabei ergab sich für alle Filme mit verschiedener Dicke dasselbe Bild. An der Oberfläche befindet sich nach der Herstellung des Films (nachdem er eine Woche der Luft ausgesetzt war) eine Nb₂O₅ Schicht mit einer Dicke von 2 bis 3 nm, die kein metallisches Nb enthält. Daran angrenzend existiert ein Bereich von wenigen nm, in welchem mit abnehmender Konzentration Sauerstoff in den Korngrenzen der Metallschicht vorliegt, als Nb₂O₅ und/oder als Nb-O Suboxid.

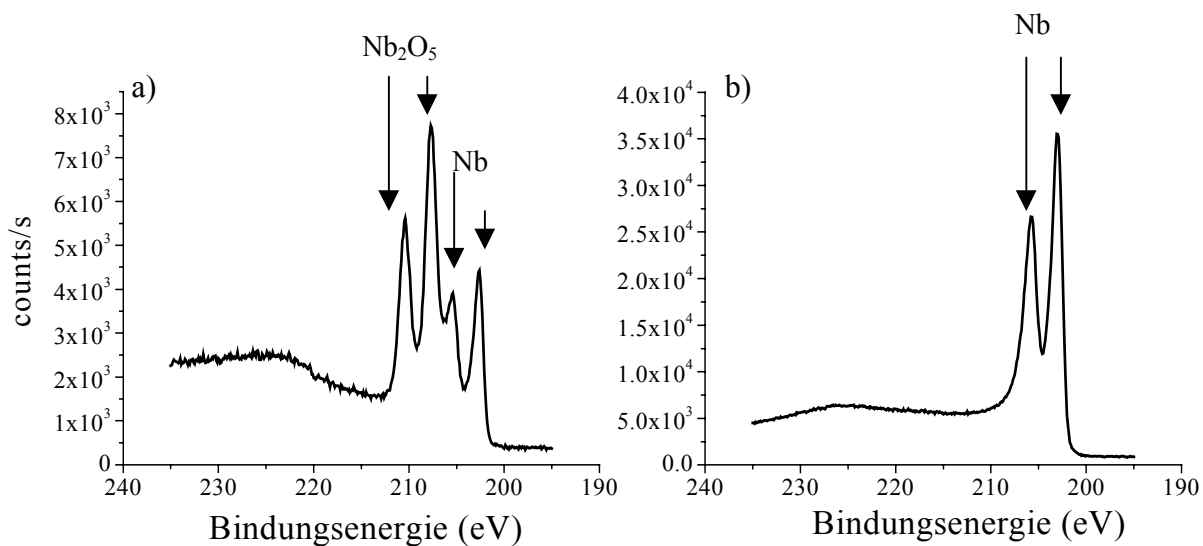


Abb. 3. XPS Spektren von einem 5 nm dicken Nb Film vor Sputterabtragung (a) und nach 30s Abtragung (b). An der Oberfläche (a) liegt das Oxid Nb₂O₅ vor, während in einem tieferen Bereich (b) nur noch metallisches Nb gefunden wird.

4.3 Textur

Die Textur der Nb Filme wurde mit Röntgendiffraktometrie durch Kombination von ($\theta/2\theta$) Scans in Bragg-Brentano Geometrie und von Polfiguren untersucht. Es ergab sich für alle Filme das Vorliegen einer {110} Fasertextur, wobei andere Texturkomponenten nicht nachgewiesen wurden. Allerdings wurde bei den dickeren Filmen mit 100 nm und 500 nm eine zusätzliche

Komponente in der Polfigur gefunden, die durch Zwillingsbildung an den 211 Ebenen der $\{110\}$ orientierten Komponente entsteht.

Die Schärfe der Textur, charakterisiert durch die Breite des Intensitätsmaximums in der Polfigur, war abhängig von der Schichtdicke, vom Substrattyp und von dessen Vorbehandlung. Für die Filme auf Si_3N_4 wurde generell eine schärfere Textur gefunden als für die Filme auf SiO_2 und für beide Typen führte eine vorherige Reinigung des Substrates mit Ar Ionen zu einer schärferen Textur. Wie im Fall der Cu Filme kann dieser Reinigungseffekt dadurch erklärt werden, dass durch die chemische Wechselwirkung zwischen Nb und O die Ausbildung einer perfekten $\{110\}$ Textur, die aus (oberflächen-) energetischen Gründen bevorzugt ist, lokal gestört wird. Da bei den Nb Filmen (im Gegensatz zu den Cu Filmen) ein Reinigungseffekt auch für die SiO_2 Substrate beobachtet wird, kann vermutet werden, dass für Nb Atome die störende Wirkung von adsorbierten O Atomen stärker ist, als von strukturellen O Atomen in amorphem SiO_2 .

Mit wachsender Schichtdicke nahm die Schärfe der $\{111\}$ Textur zu. Offenbar ist die Ausbildung einer perfekten Textur im Anfangsstadium auf einer amorphen Unterlage stärker behindert als im Stadium des Dickenwachstums, bei dem die Unterlage für hinzukommende Metallatome bereits geordnet ist.

4.4 Eigenspannungen

Die Eigenspannungen wurden am 110 Reflex mit der $\sin^2\psi$ Methode ermittelt. In allen Nb Schichten wurden als Wachstumsspannungen (nach Abzug der thermischen Spannungen, die während der Abkühlung von der Herstellungstemperatur von 100°C auf Raumtemperatur entstehen) Druckspannungen beobachtet. Diese zeigten eine sehr starke Abhängigkeit von der Schichtdicke, mit Werten um -3 GPa in 5 nm dicken Filmen und um -400 MPa in 500 nm dicken Filmen.

Es wurde gezeigt, dass ein in der Literatur berichtetes Modell für die inneren Spannungen auf die hier untersuchten Nb Sputterschichten angewendet werden kann. Demnach liegt in allen Nb Filmen ein oberflächennaher Bereich von einigen nm Dicke vor, in welchem sehr hohe Druckspannungen herrschen. Diese werden durch den Einbau von Sauerstoff, als Nb_2O_5 und/oder als Nb-O Suboxide, in den Korngrenzen nahe der Oberfläche hervorgerufen. In tieferen O-freien Bereichen liegen kleinere Druckspannungen vor, die während des Schichtwachstums (z.B. durch den „atomic peening“ Effekt) entstanden sind. Die Druckspannung weist also einen Gradienten

senkrecht zur Filmebene auf. Die gemessene Eigenspannung, als Mittelwert über die gesamte Schicht, nimmt mit wachsender Dicke ab (Abb. 4).

Die Reinigung der Substrate führte zu höheren Werten der (Wachstums) druckspannung in den dickeren Nb Filmen, besonders im Fall der Si_3N_4 Substrate. Dies weist auf eine überlagerte Zugspannungskomponente in den kolumnaren Schichten hin, die durch das freie Volumen in den Korngrenzen verursacht wird. Es wird vorgeschlagen, dass in Schichten mit breiterer $\{111\}$ Textur mehr freies Volumen zwischen benachbarten Körnern vorliegt und damit der Beitrag der Zugspannungskomponente größer ist und entsprechend die gemessene Druckspannung kleiner ist, verglichen mit Schichten mit schärferer Textur.

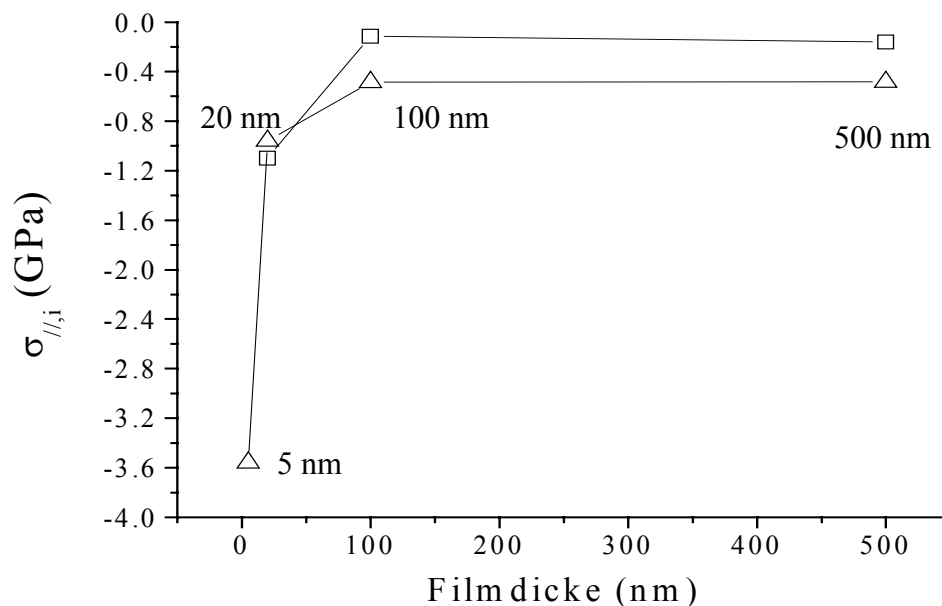


Abb. 4. Wachstumsspannung in Nb Filmen verschiedener Dicke auf Si_3N_4 vor Reinigung (□) und nach Reinigung (Δ). Bei den sehr dünnen (5 nm) Filmen wird die hohe Druckspannung im oberflächennahen Bereich gemessen, die durch Oxideinlagerung entsteht. Die dickeren (100 nm und 500 nm) Filme zeigen die Wachstumsdruckspannung, die nach Reinigung des Substrats höher ist.

Zur Untersuchung des Spannungsgradienten in den Nb Filmen wurde eine Methode der Tiefenanalyse mit Diffraktion unter streifendem Einfall angewendet. Dabei musste der Effekt der Brechung, der die Diffraktion störend überlagert, berücksichtigt werden. Obgleich die Verhältnisse auf Grund der geringen Schichtdicken bis zu 500 nm für diese Methode nicht günstig waren,

konnte nachgewiesen werden, dass zur Oberfläche der Filme hin ein Anstieg der Druckspannung vorliegt. Somit wurde das oben beschriebene Modell für die hohen Druckspannungen im Bereich der Oberfläche bestätigt.

Wiederholte Spannungsmessung (eine Woche, 4 Monate und 6 Monate nach Herstellung) ergaben, dass der Prozess der Entstehung von hohen Druckspannungen an der Oberfläche durch den Einbau von Sauerstoff nach 4 Monaten weiter fortgeschritten und nach 6 Monaten zum Stillstand gekommen war.

4.5 Mikrodehnungen

Die Mikrodehnungen in den Körnern mit der $\langle 110 \rangle$ Richtung senkrecht zur Filmebene wurden aus der Linienbreite der 110 und 220 Reflexe mit der Methode nach Williamson und Hall ermittelt. Eine Linienverbreiterung durch den Kristallitgrößeneffekt wurde nicht beobachtet. Ein systematischer Zusammenhang zwischen den Werten für die Mikrodehnung, bis zu 1%, und der Schärfe der $\{110\}$ Textur wurde gefunden, indem eine schärfere Textur mit geringeren Mikrodehnungen verknüpft ist.

4.6 Reflektometrie

Mit der Methode der Reflektometrie wurde der Schichtaufbau der Nb-Film/Substrat Systeme untersucht. Als wichtiges Resultat wurde gezeigt, dass für eine optimale Beschreibung der gemessenen Reflektivitäten mittels theoretisch simulierter Kurven eine zusätzliche Schicht an der Oberfläche der Filme eingeführt werden muß mit einer Dicke von ca. 3 nm und einer kleineren Dichte als der von metallischem Nb. Somit wurde ein weiterer, quantitativer, Nachweis für das Vorliegen einer Oxidschicht an der Oberfläche der gesputterten Nb Filme erbracht.

References

- [1] D.P. Tracy and D.B. Knorr; *J. Electron. Mater.*, **22**, 6, 1993, pp 611-616.
- [2] D.B. Knorr and D.P. Tracy; *Mater. Chem. Phys.*, **41**, 1995, pp 206-216.
- [3] R.-M. Keller, S. Bader, R. P. Vinci and E. Arzt; *Mat. Res. Soc. Symp. Proc.*, **356**, 1995, pp 453-458.
- [4] K.P. Rodbell, D.B. Knorr and J.D. Mis; *J. Electro. Mater.*, **22**, 6, 1993, pp 597-606.
- [5] Y. Tsuji, S.M. Gasser, E. Kolawa and M.-A Nicolet; *Thin Solid Films*, **350**, 1999, pp 1-4.
- [6] R. W. Hoffman; *Thin Solid Films*, **34**, 1976, pp 185-190.
- [7] J. A. Floro, S. J. Hearne, J. A. Hunter, P. Kotula, E. Chason, S. C. Seel and C. V. Thompson, *J. Appl. Phys.* **89**, 9, 2001, pp 4886-4897.
- [8] D. W. Hoffman; *J. Vac. Sci. Technol. A*, **12**, 4, 1994, pp 953-961.
- [9] H. Windischmann; *Critical Rev. in Solid State and Mat. Sci.*, **17**, 6, 1992, pp 547-596.
- [10] C.V. Thompson and R. Carel; *Mater. Sci. Engng B*, **32**, 1995, pp 211-219.
- [11] J.M.E. Harper and K.P. Rodbell; *J. Vac. Sci. Technol. B*, **15**, 4, 1997, pp 763-779.
- [12] C.V. Thompson; *Mat. Res. Soc. Symp. Proc.*, **343**, 1994, pp 3-12.
- [13] J. A. Thornton, *J. Vac. Sci. Technol.*, **12**, 4, 1975, pp 830-835.
- [14] R. Messier, A.P. Giri and R.A. Roy; *J. Vac. Sci. Technol. A*, **2**, 2, 1984, pp 500-503.
- [15] P. Bai, J. F. McDonald, T-M-Lu and M. J. Costa; *J. Vac. Sci. Techno. A*, **9**, **4**, 1991, pp 211-2117.
- [16] D. Brandon and W. Y. Kaplan; *Microstructural Characterisation of Materials*, John Wiley & Sons Inc., New York, 1999.
- [17] PHI MultiPak version 5.0, Physical Electronic, Inc. MN, USA, 1997.
- [18] PHILIPS ProFit version 1.0c, Philips Electronics N. V. The Netherlands, 1996.
- [19] U. F. Kocks, C. N. Tomé and H. –R. Wenk (Eds); *Textures and Anisotropy: Preferred Orientation in Polycrystals and their Effect on Materials Properties*, Cambridge University Press, 1998.
- [20] D.B. Knorr, H. Weiland and J.A. Szpunar; *JOM*, 1994, pp 32-36.
- [21] D.B. Knorr and J.A. Szpunar; *JOM*, 1994, pp 42-48.
- [22] T.C. Huang, G. Lim. F. Parmigiani and E. Kay; *J. Vac. Sci. Technol. A*, **3**, 6, 1985, pp 2161-2166.
- [23] N. Benouattas, A. Mosser and A. Bouabellou; *Mat. Sci. and Engng. A*, **288**, 2000, pp 253-256.
- [24] R-J. Xie, M. Mitomo, W. Kim and Y-W. Kim; *J. Am. Ceram. Soc.*, **84**,12, 2000, pp 3147-3152.

- [25] D. Yang, R. Jonnalagadda, B.R. Rogers, J. T. Hillman, R. F. Foster and T. S. Cale; *Thin Solid Films*, **332**, 1998, pp 312-318.
- [26] G. B. Harris; *Phil. Mag.* **43**, 1, 1953, pp 113-123.
- [27] B.D. Cullity; *Elements of X-Ray Diffraction*, Addison-Wesley Publishing Company Inc, Mass. USA. 1959.
- [28] U. Welzel and M. Leoni, *J. Appl. Cryst.*, **35**, 2002, pp 196-206.
- [29] H. -J. Bunge; *Texture Analysis in Materials Science, Mathematical Methods*, (English Edition) Butterworths, UK, 1982.
- [30] D.B. Knorr; *Mat. Res. Soc. Symp. Proc.* 1993, **309**, pp 75-86.
- [31] D.P. Tracy, D.B. Knorr and K.P. Rodbell; *J. Appl. Phys.*, **76**, 5, 1994, pp 2671-2680.
- [32] I. Tomov, M. Adamik and P.B. Barna; *Thin Solid Films*, **371**, 2000, pp 17-27.
- [33] M. Ohring; *The Materials Science of Thin Films* (UK Edn), Chap. 9, Academic Press, London, 1992.
- [34] V. Hauk; in *Structural and Residual Stress Analysis by Nondestructive Methods*, Elsevier Science BV, Amsterdam, The Netherlands, 1997, p 57.
- [35] C. J. Smithells and E. A. Brandes (Eds.); *Metals Reference Handbook*, 5th edition, Butterworths, London, 1976, pp 975-980.
- [36] <http://www.webelements.com>.
- [37] <http://bell.mma.edu/~jmcent/siliconprop>.
- [38] CRC Handbook of Chemistry and Physics, R. C. Weast (Ed.); 62 Edition, CRC Press, Boca Raton, FL, 1981.
- [39] E. Arzt; *Acta Mater.*, **46**, 16, 1998, pp 5611-5626.
- [40] C.V. Thompson and R. Carel; *J. Mech. Phys. Solids*, **44**, 5, 1996, pp 657-673.
- [41] W.D. Nix and B.M. Clemens; *J. Mater. Res.*, **14**, 8, 1999, pp 3467-3473.
- [42] J. A. Thornton and D.W. Hoffman; *J. Vac. Sci. Technol.*, **14**, 1, 1977, pp 164-168.
- [43] J. A. Floro, E. Chason, R. C. Cammarata and D. J. Srolovitz; *MRS Bulletin*, Jan. 2002, pp 19-25.
- [44] F. Spaepen; *Acta Mater.*, **48**, 2000, pp 31-42.
- [45] G. K. Williamson and W. H. Hall, *Acta Met.*, **1**, 1953, pp 22-31.
- [46] C. Suryanarayana and M. Grant Norton; *X-ray Diffraction A Practical Approach*, Plenum Press, New York, 1998.
- [47] J. Stringer; *Corrosion Science*, **10**, 1970, pp 513-543.
- [48] C. T. Wu; *Thin Solid Films*, **34**, 1976, pp 185-190.

- [49] J. J. Cuomo, J. M. E. Harper, C. R. Guarnieri, D. S. Yee, L. J. Attanasio, J. Angilello, C. T. Wu and R. H. Hammond; *J. Vac. Sci. Technol.*, **20**, 3, 1982, pp 349-354.
- [50] M. Murakami and T. Yogi; *J. Appl. Phys.* **57**, 2, 1985, pp 211-215.
- [51] F. M. D'Heurle and J. M. E. Harper; *Thin Solid Films*, **171**, 1989, pp 81-92.
- [52] D.B. Knorr and T.-M. Lu; *Textures and Microstructures*, **13**, 1991, pp 155-164.
- [53] W.-M. Kuschke, A. Kretschmann, R.-M Keller, R.P. Vinci, C. Kaufmann and E. Arzt. *J. Mater. Res.*, **13**, 10, 1998, pp 2962-2968.
- [54] Y. Perlovich, H. J. Bunge and M. Isaenkova; *Z. Metallkd.*, **91**, 2000, pp 149-159.
- [55] H. Huang and G. H. Gilmer; *J. Computer Aided Mater. Des.*, **7**, 2001, pp 203-216.
- [56] R. Günzel, S. Mandl, E. Richter, A. Liu, B. Y. Tang and P. K. Chu; *Surf. Coat. Technol.*, **116 – 119**, 1999, pp 1107-1110.
- [57] Y. Yamada, Y. Seno, Y. Masuoka, T. Nakamura and K. Yamashita; *Sens. Actuators, B*, **66**, 2000, pp 164-166
- [58] R. F. Broom, ThO. Mohr, W. Walter and R. B. Laibowitz; *IBM J. Res. Develop.*, **24**, 2, 1980, pp 121-222
- [59] L. J. Weirick and W. L. Larsen; *J. Electrochem. Soc.*, **119**, 4, 1972, pp 465-471.
- [60] D. W. Hoffman and J. A. Thornton; *Thin Solid Films*, **45**, 1977, pp 387-396.
- [61] R. W. Hoffman, *Physics of Nonmetallic Thin Films*, NATO Advanced Study Institutes Series, Plenum, New York, 1976, pp 273-353.
- [62] B. Okolo, U. Welzel, P. Lamparter, T. Wagner and E. J. Mittemeijer; *Mat. Res. Soc. Symp. Proc.*, **695**, 2002.
- [63] B. Okolo, P. Lamparter, U. Welzel, T. Wagner and E. J. Mittemeijer; *Mat. Sci. Forum*, 2002, pp 691-696.
- [64] B. Okolo, P. Lamparter, U. Welzel, T. Wagner and E. J. Mittemeijer; to be published (see Chapter 1 of this thesis)
- [65] U. Welzel, J. Ligot, P. Lamparter, A. C. Vermeulen and E. J. Mittemeijer; to be published.
- [66] J. H. Scofield, "Hartree-Slater subshell photoionisation cross-sections at 1254 and 1487 eV", *J. Elect. Spect. and Related Phenomena*, **8**, 1976, pp 129-137.
- [67] Thermo VG Scientific, "Avantage data spectrum processing", document number HA600045, issue 1, 2001.
- [68] J. Halbritter; *Appl. Phys. A*, **43**, 1987, pp 1-28.
- [69] L. J. Weirick and W. L. Larsen; *J. Electrochem. Soc.*, **119**, 4, 1972, pp 472-476.
- [70] O. Hellwig and H. Zabel; *Physica B*, **283**, 2000, pp 228-231.

- [71] C. Bouillet, D. Ciosmak, M. Lallemand, C. Laruelle and J. J. Heizmann; *Solid State Ionics*, **101 – 103**, 1997, pp 819-824.
- [72] B. Li and I. Kojima; *Appl. Surf. Sci.*, **169-170**, 2001, pp 371-374.
- [73] Peter Graat; Private Communication.
- [74] A. G. Dirks, R. A. M. Wolters and A. E. M. De Veirman; *Thin Solid Films*, **208**, 1992, pp 181-188.
- [75] H. Huang, G. H. Gilmer and T. Diaz de la Rubia; *J. Appl. Phys.*, **84**, 7, 1998, pp 3636-3649.
- [76] I. A Gindin, Ya. D. Starodubov and V. K. Aksenov; *Sov. Phys. Solid State*, **17**, 4, 1975, pp 648-649.
- [77] D. A. Mirzayev, M. M. Shteynberg and Yu. N. Goykhenberg; *Fiz. Metal. Metalloved.*, **28**, 4, 1969, pp 593-602.
- [78] E. A. Brandes and G. B. Brook (Eds), *Smithells Metals Reference Book*, 7th edition, Butterworth-Heinemann, Oxford, 1992, pp 15-3, 5.
- [79] <http://www.matweb.com>
- [80] PCPDFWIN version 2.02; JCPDS-International Centre for Diffraction Data, 1999.
- [81] M. F. Toney and S. Brennan; *Phys. Rev. B*, **39**, 1989, pp 7963-7966.
- [82] R. Delhez, Th. H. de Keijser and E. J. Mittemeijer; *Fres. Zeitschr. Anal. Chem.*, **312**, 1982, p 1.
- [83] WIN-REFSIM, version 1.2K, Bruker AXS GmbH, 1995-1999.

Danksagung

I am immensely grateful to Prof. Dr. Eric Mittemeijer and Dr. Peter Dearnley for facilitating and making my Ph.D. program possible. I specially thank my kind, patient and witty advisor Dr. Peter Lamparter and my colleagues at Max Planck Institute for Metals Research in Stuttgart; especially Dr. Udo Welzel and Dr. Thomas Wagner for persevering with me.

I thank the following for their warm company in Stuttgart:

Emeka, Steve, Fred, Obum, Flora, Birgit&Tilman, Ralph&Annegret, Patrick, Hervais, Siglinde, Natascha, Jiang&Yuya, Maik, Mattheo, Udo, Andreas, Matthias&Yvonne, Klaus&Pia, Sycha family, Ute, Gerd, Josef, Maritta, Marion, Jay, Matthais, Sonja, Rabe, Lydia, Peter&Marianne and everyone whom had made my stay in Germany blissful.

May God bless my family and best friends: Harry, Grace, Samira, Gozi, Mike, Junior&family, Ral, Peter, Traudl, Alexander, Fide, Uncle Mike and Auntie Cordelia, Eddy&family, Eun-Jae and Mark.

Curriculum Vitae

Name Brando Chidi Okolo

Date of Birth October 22, 1970

Place of Birth Enugu (Nigeria)

School 1976 – 1982
Ekulu Primary School – Enugu – Nigeria

1982 – 1988
Federal Government College Kaduna – Nigeria

Higher Education 1989 – 1995
Enugu State University of Science and Technology
Enugu – Nigeria. (Bachelor of Engineering, Chemical Eng.)

National Service 1995 – 1996
Physics Teacher (Dawakin – Tofa High School – Nigeria)

Employment 1996 -1998
Operations Engineer (Chyn Laboratories – Abuja – Nigeria)

Higher Education 1998 – 1999
University of Leeds – England (UK)
Master of Science (Chemical Engineering)

1999 – 2003
Ph.D. Student at Max Plank Institute for Metals Research,
Institute for Materials Science, Stuttgart